Thesis for the Degree of Ph. D.

Synthesis and Characterization of Boron-Based Scintillators for Thermal Neutron Detection and Imaging

Department of Physics, Major in Nuclear Physics
The Graduate School

Sudipta Saha

June 2022

The Graduate School
Kyungpook National University

Synthesis and Characterization of Boron-Based Scintillators for Thermal Neutron Detection and Imaging

Sudipta Saha

Department of Physics, Major in Nuclear Physics
The Graduate School

Supervised by Professor HongJoo Kim

Approved as a qualified thesis of Sudipta Saha
for the degree of Ph. D.
by the Evaluation Committee

June 2022

Chairman Hwanbae Park ㊞

Guinyun Kim ㊞

Sunghwan Kim ㊞

MooHyun Lee ㊞

HongJoo Kim ㊞

The Graduate School council
Kyungpook National University

List of Contents

List of Figures

List of Tables

Synthesis and Characterization of Boron-Based Scintillators for Thermal Neutron Detection and Imaging*

Sudipta Saha

Department of Physics, Major in Nuclear Physics
Graduate School, Kyungpook National University,
Daegu, South Korea
(Supervised by Professor HongJoo Kim)

Abstract

The thermal neutron imaging technique has been advanced to fulfill the requirements of a variety of applications. To fulfill the requirements, research was intended to find a suitable transparent crystalline compound that could serve the purpose of a scintillation screen for thermal neutron imaging. Depending on the thermal neutron absorption cross-section of a variety of elements, the compounds containing Li, B, and Gd were attracted the most due to their high microscopic absorption cross-section. Considering the γ-rays of different energies from neutron sources and the environment, it is very crucial to discriminate between thermal neutrons and γ-rays by the scintillator.

---

* A thesis submitted to the Council of the Graduate School of Kyungpook National University in partial fulfillment of the requirements for the degree of Ph.D. in June 2022

Three new glass compositions were tested for their ability to distinguish thermal neutrons from γ-rays. Prior to the proceedings, the thermal neutron facility was characterized to determine the thermal neutron and γ-ray contents in the beam as well as the luminescence properties of the glass samples. The samples were doped with Eu^{3+} -ions and showed their characteristic 4f-4f transition emission. BLiY:1.5Eu sample was identified through digital and film-based neutron radiography techniques to distinguish thermal neutrons, successfully rejecting the accompanied γ-rays. As a result, $Li_6Y(BO_3)_3$ was identified as a candidate for crystal growth that matches the elements exist in the glass sample.

The Czochralski method was used to successfully grow a single crystal of pure $Li_6Y(BO_3)_3$, which was then doped with 4 mol% Dy^{3+} and 1 mol% Pr^{3+}-ions. The doped crystals were characterized by luminescence studies under X-ray and photo-excitation. The scintillation performance of these single-crystal samples was evaluated using β^- and α-particles, γ-rays, along with moderated thermal neutrons from ^{90}Sr, ^{241}Am, ^{60}Co, and ^{252}Cf radioactive sources, respectively. 4 mol% Dy^{3+} doped $Li_6Y(BO_3)_3$ was found to have 4500 ± 550 Photons/MeV, or 92.8 % photon counts in comparison to CMO crystal under β^- irradiation. The grown samples were found efficient enough to distinguish thermal neutrons from γ-rays generated by nuclear research reactors as well as radioactive source, ^{252}Cf. $Li_6Y(BO_3)_3$ was discovered to be promising for future use as a thermal neutron scintillator for imaging.

Chapter 1. Introduction

1.1 Thermal Neutron Scintillators

Borate-based scintillators that are position-sensitive neutron detectors have been attracted in thermal neutron experimental procedures. Typically, these detectors are utilized, being composed of single-crystals and semiconductor materials [1]. They are, however, seldom used in equipment requiring high signal-to-noise ratios (SNRs), such as thermal neutron scintillation for imaging. The fundamental reason for this is the scarcity of non-hygroscopic thermal neutron scintillators with high light output and a high neutron-gamma discrimination ratio.

Thermal neutron imaging technology has several applications in a variety of disciplines [2–5]. The number of fields continues to grow daily as more exact needs for instrument customization emerge. Numerous researchers have conducted different forms of methodological development research to meet the needs of these growing demands [3,6–8]. By replacing the radiographic film with a neutron-to-photon converting scintillation screen and high-resolution CCD or CMOS sensor cameras, the method of neutron radiography (NR) has been progressed into neutron imaging (NI) [9,10]. The sensors are expected to be effective in detecting the low scintillation light output by the scintillators and converting it to an electrical signal that can be displayed in a two-dimensional user interface through software data processing.

Among the various phases of matter, single crystals and glasses are transparent, which minimizes scintillation light self-absorption and multiple

scattering. It is why transparent crystals and glasses containing thermal neutron-sensitive materials are gaining increased interest in the investigation of high light yield with efficient thermal neutron scintillation rejecting environmental γ-rays [11].

1.2 Borate Crystals and Glasses

Boron is used in a variety of industrial applications, the majority of which involve boron-oxygen complexes. This class has diverse structural chemistry, including crystalline and amorphous transparent solids of reasonable performance and profitability. Boron's electron configuration is $[He]2s^2 2p^1$, implying that it might construct intramolecular compounds. With oxygen, the element creates extremely strong covalent bonds. Boron-oxygen combinations, on the other hand, do not generally form multicenter bonds [12]. The boron atom's unique properties are primarily responsible for the rich structural diversity of borate chemistry; its valence shell orbitals, vacant p-orbitals, and planar ionic groups such as the boron atom's $(BO_3)^{3-}$, $(B_3O_6)^{3-}$, and $(B_3O_7)^{5-}$ exhibit interesting conjugation; and it's three or four-fold coordinative modes are responsible for the rich structural diversity of borate chemistry [13–15].

In recent years, researchers have been more interested in borate crystals, which have a large band gap, are non-hygroscopic, and have a high luminescence efficiency. Because of the high concentration of Li in alkali orthoborates such as $Li_6X(BO_3)_3$ (X= Y, Gd, Lu), they have piqued the interest of researchers for their potential uses in thermal neutron studies, above all other borate compounds. A wide range of applications, including thermal neutron detection, light-emitting diode (LED) technology, medical imaging,

and other fields, have been investigated using the compounds in this category [16–19].

The amorphous structure can be formed by boron oxide (B_2O_3) glass former as [BO_3^{3-}] with the benefits of thermal stability, good transparency, as well as high solubility of rare earth (RE) ions. In the glass network, boron can be structured in both three coordination (B_3) and four coordination (B_4) states depending on the molar concentration of network modifiers. However, a glass containing boron tri-oxide (B_2O_3) usually has high phonon energies (about 1300 cm^{-1}), which allows the non-radiative transitions, and as a result, RE ion emission intensity can be significantly decreased. The addition of heavy metal oxides to the network can make it more stable, resistant to moisture, and reduce the phonon energies as well [20,21].

1.3 Motivation

Although there are a lot of commercial scintillators available for thermal neutron imaging, the technology is still very expensive and sophisticated. The most common scintillators in operation are (1) Li-based, (^{6}LiF/ZnS doped with Ag or co-doped with Cd and Ag), and (2) Gd-based, (Gd_2O_2S doped with Tb^{3+}, which is available with enriched ^{157}Gd also). Ce^{3+} doped $Gd_3Al_2Ga_3O_{12}$ is another available scintillator, which is recommended for this purpose [22]. However, all these scintillators have emissions in different distinctive visible photon energy regions. The emitted photons that are identified by the CCD or CMOS camera sensors have a typical quantum efficiency (QE) that increases with the wavelength from 450 to 650 nm [11]. The most important fact in neutron imaging is to eliminate the impact of γ-rays, emitted from both the source and the detector (e.g., Gd) [23]. The sensors

are silicon chips, which are very sensitive to the γ-rays, resulting in a white spot on the screen for each incident. The consequences are explained in the literature elsewhere [23]. To find a proper single crystal scintillator, it is required to study a variety of compounds that contain Li, B, and Gd separately and together in a facility where the incident thermal neutron contents and γ-ray contents are known. At the same time, the proposed samples are also required to be compared with the existing scintillator to find the appropriate effectivity.

Glasses are substances that can be manufactured quickly, in large numbers, in a variety of forms, and at a lower cost than a single crystal. The glass samples containing such thermal-neutron-sensitive elements can be characterized through X-ray-induced and photon-induced luminescence followed by exposure to a thermal neutron beam with sufficient intensity. It is quite adequate to apply the samples of appropriate thicknesses as scintillators both with digital camera sensors and non-destructive testing (NDT) industrial films as a direct film neutron radiography method, replacing the existing scintillators. It is the first time transparent glass samples were attempted for thermal neutron imaging as a scintillator [24].

The appropriate combination of compounds from the studied glass samples was found that contains Li, Y, and B [24]. $Li_6Y(BO_3)_3$ (LYBO) is the compound containing these elements and can be grown as single crystals by the Czochralski technique for further characterizations [25]. As the light yield is more important for thermal neutron imaging, dopant luminescence with long lifetime can be allowed considering the image acquisition segment from milliseconds (ms) to seconds (s). Therefore, attention was given to enhancing the luminescence efficiency of the crystal activating with Dy^{3+} -ions. Prior to

the thermal neutron exposure, the grown crystals are required to be characterized with X-rays, photoluminescence excitation, and emission as well as scintillation efficiency with α and β^- -particles from ^{241}Am and ^{90}Sr radionuclides, respectively. The emission peaks originating from Dy^{3+} ions are due to the forbidden $4f^9$-$4f^9$ transitions with the characteristics of a longer lifetime. Such long decay components of a crystal do not permit the spectroscopic scintillation measurements under excitation of γ-rays and α-particles. Therefore, instead of spectroscopic measurements, a continuous scintillation photon-counting technique was applied for the estimation of the comparative light yield [11].

Ce^{3+} and Pr^{3+} are well-known elements for fast decay components that can facilitate the real-time detection ability through doping in the same crystalline material. As previously reported [26–28], triply ionized praseodymium (Pr^{3+}) can display both interconfigurational ($4f^15d^1$-$4f^2$) and intraconfigurational ($4f^2$-$4f^2$) emission transitions with a quantum yield greater than unity depending on the host material. Followed by a thorough luminescence investigation, the grown crystal sample can be tested to find a response of moderated thermal neutron from a ^{252}Cf source by applying the pulse shape discrimination (PSD) method [29].

1.4 Thesis Proceedings

The thesis contains a theory section in Chapter 2 that discusses the theoretical aspects, applied during the experimental works. The next chapter will explain the experimental equipment and technical details used in this research. Chapter 4 has three sub-sections explaining the results and

discussions of the three steps of our experimental approaches. The last chapter, 5, summarizes and concludes the thesis with remarks.

Chapter 2. Theory

2.1 Thermal Neutron Interaction

In scintillation crystals, neutrons do not directly cause ionization, but their interaction with the nuclei of the element is possible to be detected. The basic mechanism on which most radiation detectors depend for functioning is the formation of free charge carriers. Nuclear reactions are the principal approach for detecting thermal neutrons since they lack the energy necessary for displacements following the encounter. The common nuclear reactions that contribute to the scintillations purposes are mentioned as follows:

a) The reaction cross-sections that decrease in terms of the square root of the neutron energy [30]

I. $^{3}He + {}^{1}n \rightarrow {}^{3}H + {}^{1}H + 0.764\ MeV$

II. $^{6}Li + {}^{1}n \rightarrow {}^{4}He\ (2.05\ MeV) + {}^{3}H\ (2.73\ MeV)$; (Q-value: 4.8 MeV)

III. $^{10}B + {}^{1}n \rightarrow {}^{7}Li\ (0.84\ MeV) + {}^{4}He\ (1.47\ MeV)$; (Q-value: 2.79 MeV) (Ground State)

$\rightarrow {}^{7}Li^{*}\ (0.84\ MeV) + {}^{4}He\ (1.47\ MeV)$; (Q-value: 2.31 MeV) (Excited State)

b) Resonance (n,γ) reactions inhibit γ-ray emission while transferring energy to orbital electrons. The process produces complex γ-rays and conversion electrons [31,32].

I. $^{155}Gd + {}^{1}n \rightarrow {}^{156}Gd^{*} \rightarrow {}^{156}Gd + (\gamma + \text{conversion electrons } (7.9\ MeV))$

(Main electron energies are 39 and 81 keV)

II. $^{157}Gd + {}^{1}n \rightarrow {}^{158}Gd^{*} \rightarrow {}^{158}Gd + (\gamma$ + conversion electrons (8.5 MeV))

(Main electron energies are 29, 71, 78 and 131 keV)

At the moment, the scintillators that have been studied are mostly composed of Li, B, and Gd, activated with rare-earth elements such as Ce, Dy, Tb, and Eu. They are also gaining interest as potential substitutes for existing commercial scintillation screens [33–36].

2.2 Cross-section

Neutron interactions with materials might take part in the form of scattering or absorption. Scattering may cause a change in the energy and direction of travel for neutrons, but it is unable to cause the absorption of a free neutron. However, the consequences of nuclear absorption involve fission or the synthesis of a new nucleus with another particle or particles such as protons (β^{+}), alpha particles (α), and gamma-ray (γ) photons cause the removal of free neutrons. The **cross-section** term expresses the probability of such interactions between an incident particle (neutron) and a target nucleus. The probability of occurrence of nuclear reactions is primarily dependent on the energy of the neutrons and on the properties of the nucleus with which it is interacting. Neutron cross sections are expressed in units of barns, where: 1 [barn] = 10^{-24} [cm^{2}]. When a neutron is absorbed, nuclear transformation occurs inside the target nucleus. It may take the form of nuclear reactions, nuclear fission, or capture, among others.

Let us denote the reaction rate as R, which should be constructed as proportional to the area of the target A, thickness x, the flux density of the

incident neutron beam ϕ, average velocity of those neutrons ῡ, and the number of the target nuclei in the target N, as shown in Figure 2.2.1. Mathematically, it can be written as equations (2.1) and (2.2)

$$R \propto A \cdot x \cdot \phi \cdot \bar{\upsilon} \cdot N, \quad (2.1)$$

$$\text{or, } R = \sigma \cdot A \cdot x \cdot \phi \cdot \bar{\upsilon} \cdot N \text{ [Reactions/Sec]}, \quad (2.2)$$

Here, the proportionality constant σ is the **microscopic cross-section** [37].

The total capture cross-section includes all possible interactions like scattering, absorption, radiative capture, etc., except fission reaction.

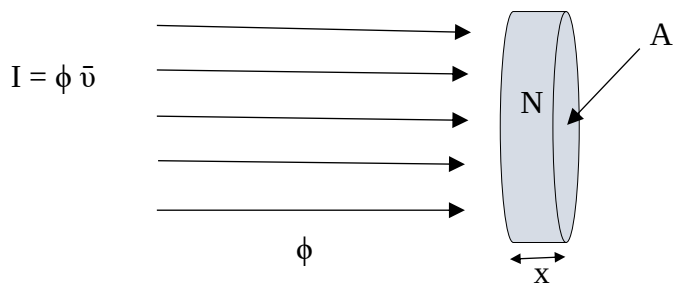

Figure 2.2.1. A schematic view that shows the incident thermal neutron beam passing through the sample defines the thermal neutron cross-section.

A complete set of data that includes coherent and incoherent scattering lengths, scattering, and absorption cross-section data can be found in the literature, summarized by Varley F. Sears [38]. Using the volumetric and molar concentration [37] as well as the isotopic abundance of the elements in the compounds, thermal neutron absorption cross-section values of $Li_6X(BO_3)_3$ (X= Y, Gd) compounds are evaluated as reported in Table 2.1.

Table 2.1. The list of thermal neutron cross-sections for $Li_6X(BO_3)_3$ (X= Y, Gd) compounds

Crystal	Doping	Cross-section [b]	Remarks*
$Li_6Y(BO_3)_3$	0.2 mol% Ce	143.4358	Natural Conc.
$Li_6Y(BO_3)_3$	4.0 mol% Dy	145.5258	Natural Conc.
$Li_6Y(BO_3)_3$	6.0 mol% Eu	157.7371	Natural Conc.
$Li_6Y_{0.5}Gd_{0.5}(BO_3)_3$	-	1451.297	Natural Conc.
$Li_6Gd(BO_3)_3$	-	2759.158	Natural Conc.
$Li_6Gd(BO_3)_3$	0.2 mol% Ce	2753.926	Natural Conc.
$Li_6Y(BO_3)_3$	-	418.0148	Enriched ^6Li
$Li_6Y(BO_3)_3$	-	627.8569	Enriched ^{10}B

* Natural conc. refers to the natural isotopic abundance

2.3 Thermal Neutron Energy and Velocity

The most probable kinetic energy of thermal neutron can be evaluated using the following equation (2.3) that considers the Maxwellian distribution

$$E_{mp} = \frac{1}{2}mv_{mp}^2 = \frac{1}{2}m\frac{2kT}{m} = kT, \qquad (2.3)$$

where m is the neutron mass, k is the Boltzmann constant, and T is the temperature in K. Thus, thermal neutrons can be referred to as kT neutrons as well as independent of their mass. Taking the Boltzmann constant in the [erg/K] unit and converting the environment temperature into $[K \cdot eV/erg]$,

the evaluated thermal neutron energy is $0.025\ eV$. The most probable velocity of thermal neutrons can also be determined using equation (2.4).

$$v_{mp} = \sqrt{\frac{2kT}{m}} \approx 2{,}200\ [m \cdot s^{-1}] \tag{2.4}$$

2.4 Charged Particle Interaction

Although neutron is an uncharged particle, it creates charged particles interacting with elements in glass and crystalline compounds. In addition, the radionuclides and the neutron sources also initiate charged particles that will interact with the scintillating compounds. Coulomb interaction takes place due to interactions of the incident charged particles with the host atoms. The traversing charged particle collides concurrently with the host material electron cloud. Excitation or ionization occurs when charged particles transmit energy to electrons. Rutherford scattering and alpha-induced reactions are also conceivable there but with a negligible effect. Calculation of stopping power through such a phenomenon is the prime concern that can be determined by the Bethe-Bloch formula as given in the equation (2.5) below [39]:

$$-\frac{dE}{dx} = \frac{4\pi k_0^2 Z^2 e^2 n}{mc^2\beta^2}\left[\ln\frac{2mc^2\beta^2}{I(1-\beta^2)} - \beta^2\right], \tag{2.5}$$

where k_0 is the Coulomb constant ($8.99 \times 10^9\ N \cdot m^2 \cdot C^{-2}$), Z is the atomic number of the incident charged particle, e is the magnitude of the electron charge, n is the number of electrons per unit volume in the host medium, m is electron rest mass, c is the velocity of light in vacuum, $\beta = \frac{v}{c}$ = speed of the particle relative to c, and I is the mean excitation energy of the medium.

2.5 Interaction of X-rays and Gamma (γ) Rays

The scintillation process can be classified into three stages: a) the initial interaction of radiation with matter, followed by relaxation and thermalization resulting in electron-hole pairs having energies approximately equal to band-gap (E_g), b) additional relaxation, forming excitonic states, and transportation of this energy to luminescence center, and c) luminescence [40]. Ionizing radiation can be electromagnetic rays. Excited atoms release "X-rays" with quantum energies ranging from 1 to 100 keV, while excited nuclei release γ-rays, which have typical energy of several MeV. In both circumstances, the radiation is in the form of photons. Because the photon is uncharged, it does not interact with matter through the Coulomb force, allowing it to travel longer distances without interaction. Thus, the mean free path is defined by the distance between two subsequent collisions, which can vary from a few millimeters for low-energy X-rays to tens of centimeters for high-energy γ-rays. However, when contact occurs, it might change the photon's energy and direction, or even the photon can disappear entirely. The photon energy is transmitted to one or more electrons in the absorber material. The energy of these electrons may be used to infer information about the energy carried by the incoming photons. The three main types of such interactions are explained below in detail.

2.5.1 Photoelectric Effect

In this process, a sufficiently energized γ-ray photon interacts with a rest atom and vanishes entirely, releasing an electron (photoelectron) that was tightly bound or in the K-shell of the atom. The process is shown

schematically in Figure 2.5.1. The ejected photoelectron has the kinetic energy (E_e) (equation (2.6)):

$$E_e = h\nu - E_b, \tag{2.6}$$

where $h\nu$ is the incident photon energy and E_b is the binding energy of the electron inside the atom.

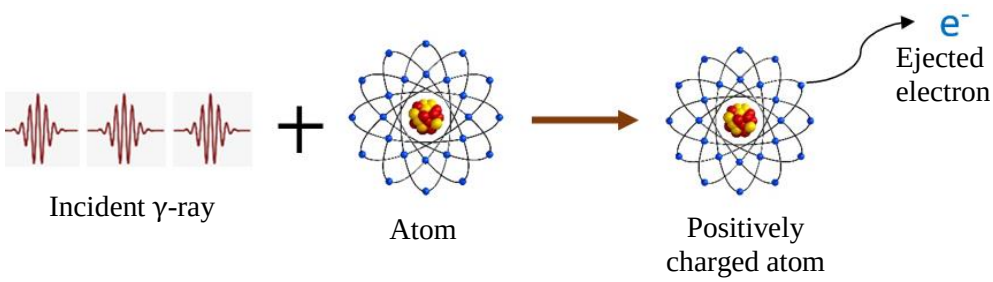

Figure 2.5.1. A schematic view of the photoelectron ejection process.

The outer shell electrons fill the void left by the expelled electron, causing the emission of a characteristic X-ray. The likelihood of a photoelectric effect, i.e., the photoelectric cross-section per atom (σ_γ), is proportional to (equation (2.7),

$$\sigma_\gamma \propto \frac{Z^n}{E_\gamma^{3.5}}, \tag{2.7}$$

where Z is the atomic number and n is a parameter that varies from 4 to 5 [41].

2.5.2 Compton Scattering

When the incident γ-ray is energetic enough to eject the electron (recoil electron) upon colliding and deflected with an angle, θ from its original direction, the phenomenon is known as Compton scattering. The loosely

bound electron has a binding energy of a few eV, while the γ-ray photon contains energy in keV or higher. The photon transmits some of its energy to the electron during this encounter, resulting in the formation of a Compton electron and a Compton scattered photon. So, we can write equation (2.8)

$$E_{Ce} = E_{\gamma} - E_{\gamma'}, \tag{2.8}$$

where E_{Ce} is the energy of the Compton electron, E_{γ} and $E_{\gamma'}$ are photon energies before and after the collision.

2.5.3 Pair Production

When the incident γ-ray photon has an energy that exceeds twice the rest mass of electron energy, which is $2m_e c^2 = 1.02$ MeV, can initiate the pair production. This interaction occurs inside the Coulomb field of a nucleus. The input photon energy E_{γ} is absorbed during a pair production interaction, resulting in the formation of an electron-positron pair with the total energy E_{pp}, which can be written as equation (2.9).

$$E_{pp} = E_{\gamma} - 2m_e c^2 \tag{2.9}$$

The positron annihilates with an electron, creating two γ-ray photons with 511 keV energies propagating in the opposite direction. Another photoelectric or Compton interaction may occur inside the scintillator by these photons.

2.6 Generation of Electron-Hole pairs

When ionizing photons are absorbed, secondary electron and hole pairs are generated inside the material. The production of secondary electron-

hole (e-h) pairs persists indefinitely until the pairs lose their ability to ionize further. The surplus energy of these electrons and holes is dissipated during thermalization. These processes are expected to occur on a time scale of around 1 ps. Several hypotheses and experiments have been performed to compute the number of such thermalized e-h pairs per unit of absorbed energy. Rodnyi et al. examined these hypotheses in-depth [40]. The number of generated e-h pairs (N_{eh}) is proportional to the absorbed photon energy (E_γ), which can be written as equation (2.10),

$$N_{eh} \sim \frac{E_\gamma}{E_{eh}}, \tag{2.10}$$

where E_{eh} is denoted for the average energy required to cause a single pair of thermalized e-h.

2.7 Energy Transportation to Luminescence Center

Electrons and holes that have been thermalized transmit their energy through direct electron-hole capture and the formation of excitons. In direct capture, the luminescence center is activated sequentially by a hole and an electron, or by an electron and a hole, referred to as electron and hole recombination luminescence. Additionally, electrons and holes may be quenched during the migration phase of non-radiative transition. The density of the ionization track dictates the competence of these non-radiative relaxation processes. The luminescence efficiency drops as the ionization track becomes denser, whereas the non-radiative quenching rate rises. Non-radiative energy transmission processes between luminescence centers can be found in the literature [42]. Charge carriers may be trapped in the forbidden gap of the scintillator by impurity atoms or lattice defects lying

between energy levels. It often results in a substantial delay in the scintillation process and the appearance of afterglow [43].

2.8 Luminescence

Luminescence is a complex system of electronic radiative transitions after absorbing external radiation, photon, or energy. Luminescent emission occurs by overcoming the non-radiative transitions of energetic electrons decaying through thermal energy or phonons to the environment, as shown in Figure 2.8.1. Luminescence can be categorized by the relaxation processes of the energy that affects the decay periods of the emitted photons significantly. The emission spectra and the photon lifetime are regulated by the spectroscopic selection rule that defines whether the electronic transitions are allowed or forbidden. The spectroscopic selection rules have two parts

(a) *Spin Selection rule:* The relative alignments of the spins of electrons in a system cannot be altered by the electromagnetic energy of incident radiation. A singlet (S=0) cannot transition to a triplet (S=1) because an originally antiparallel electron pair cannot be changed to a parallel pair. The rule can be outlined as $\Delta S = 0$ for all spin-allowed transitions.

(b) *The Laporte Selection Rule:* According to the Laporte selection rule, the transitions are permitted only in a centrosymmetric molecule or ion, which is accompanied by a change in parity. It is often sufficient to recall if the quantum number *l* does not change in a centrosymmetric complex, there can be no change in parity. As a result, the s-s, p-p, d-d, and f-f transitions become forbidden. Since s and d orbitals are g, while p and f orbitals are u, s-p, p-d, and d-f transitions have been allowed; however, s-d and p-f transitions are restricted. Due to the fact that d-d ligand-field transitions are g-g in a centrosymmetric compound, they are forbidden. Their forbidden nature

explains why these transitions are weaker in octahedral complexes (which are centrosymmetric) than in tetrahedral complexes, where the Laporte rule becomes silent (they are non-centrosymmetric and have no g or u as a subscript) [44].

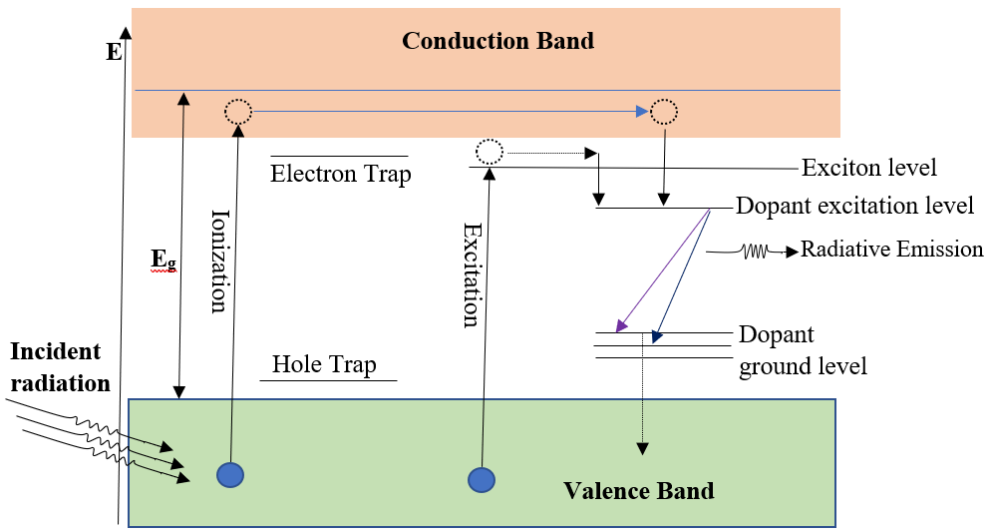

Figure 2.8.1. The schematic view of a random band structure of a crystalline compound that contains dopants that produce luminescence after absorbing external radiation energy.

2.8.1 Interconfgiurational (f-d) and Intraconfigurationsal (f-f) Transitions

The majority of rare-earth-doped crystalline materials exhibit both 4f-4f and 4f-5d transitions. The surrounding environment effectively shields the 4f-electrons, preserving their chemical nature. However, the 5d band is known to be quite environment-dependent. The 5d→4f transitions are also recognized for their broad emission and absorption bands. The association of the 5d electron around with its lattice phonons causes a broadening of the band. It

indicates that the transitions from 4f to 5d are substantially more environment-dependent. It is shown by phenomena such as nephelauxetic effects and crystal field splitting in the literature [45]. Transitions from 4f to 5d are recognized as interconfigurational transitions, which are parity allowed. In the lanthanides, the energy E required to excite an electron from the $4f^n$ ground state multiplet to the lowest $4f^{n-1}5d$ level changes irregularly with the value, n. The amount of variance that was observed experimentally appeared relatively comparable for neutral and ionized lanthanides, regardless of the fact that such electron configurations for Ln, Ln^+, and Ln^{2+} are distinct [46,47]. Numerous rare-earth-doped compounds, containing Eu^{2+}, Ce^{3+}, and Pr^{3+}, emit in the wide band owing to 5d–4f transitions. Due to the fact that parity and spin are allowed, the 5d–4f transition has an extremely short decay period, which is from a few nanoseconds to a few microseconds [48].

The intraconfigurational transitions through the $4f^n$-$4f^n$ energy states, which are parity forbidden, are also observed in the trivalent lanthanides (Ln). Dieke's group pioneered the absorption and emission energy levels of lanthanides, which became known as Dieke's diagram, which presents the energy level of rare-earth ions in their 3+ charged states with respective Russel-Saunders terms [49,50]. In such a case, the energy states are narrow enough and located near the neighboring energy states, allowing the electron to exhibit a non-radiative transition for relaxation. During the radiative transition between the 4f-4f states, strong emission lines, such as those of Tb^{3+}, Eu^{3+}, Dy^{3+}, Gd^{3+}, and so on, are seen. Additionally, 4f-4f transitions have a slow decay period of approximately micro to milliseconds due to their parity and spin forbidden transitions [51]. Sometimes the transitions can be spin allowed (e.g., Pr^{3+}), which results in a faster radiative decay time (a few µs).

2.9 Thermal Neutron Beam Collimation and **QE**

Thermal neutrons emitted by a source must be collimated in order to create a useable beam. The optimum solution is to keep the neutron source and moderator behind a neutron-absorbing armor and enable a few of the neutrons to pass through a hole in the shield, a process called beam collimation. The emerging beam's angular spread will be controlled by the collimator hole's length to diameter ratio; hence, to guarantee a small beam spread, a collimator will typically have a high L/D ratio. This ratio may be increased significantly but at the expense of significant beam intensity loss and the appearance of rings or streaks on the radiography picture. The entrance aperture of a divergent collimator is rather small, and the collimator hole diverges consistently throughout its length. The angular dispersal of the neutron beam reaching the target is determined only by the source size and distance. The following equation (2.11) provides an estimation of the flux originating from a collimator tube [52]:

$$\Phi = \frac{A}{16}\left(\frac{D}{L}\right)^2\left(\phi_i + \frac{1}{\Sigma}\frac{\partial\phi}{\partial z}\right), \tag{2.11}$$

where ϕ_i is the neutron intensity at the entrance to the collimator in $n \cdot cm^{-2} \cdot s^{-1}$, Φ is the neutron emission at the exit of the collimator in $n \cdot s^{-1}$, A is the collimator area in cm^2, D is the diameter of the inlet aperture of the collimator in cm, L is the length of the collimator in cm, Σ is the total macroscopic cross-section of moderator in cm^{-1}, and $\frac{\partial\phi}{\partial z}$ is the flux gradient at the inner face of the collimator [53]. Since the flux gradient is very small, the fraction of neutrons lost due to collimation can be approximated by the ratio, equation (2.12):

$$\frac{flux\ at\ the\ entrance}{flux\ at\ the\ exit} = \frac{\phi_i}{\phi_0} = 16\left(\frac{L}{D}\right)^2, \tag{2.12}$$

where ϕ_0 is the neutron flux at the outlet of the collimator in $n \cdot cm^{-2} \cdot s^{-1}$. The collimator length to inlet diameter ratio (L/D) is called the collimator ratio. Since the length to diameter (L/D) ratio of a collimator affects both resolution and efficiency, it is often employed as a basic way of characterization. The resolution of the radiography system may be explained by evaluating the influence of the collimator's radiographic dimensions on the unsharpness of the output image. This radiographic unsharpness is demonstrated by equation (2.13)

$$U_g = \frac{D}{L_s} \times L_f \approx \frac{1}{L/D}, \tag{2.13}$$

where U_g is the geometric (radiographic) unsharpness in cm, L_s is the length from inlet to sample position in cm, and L_f is the object to scintillator distance in cm, as shown in Figure 2.9.1. Typically, $L_f \ll L_s$, and hence the geometric unsharpness is directly related to the inverse of the collimator ratio.

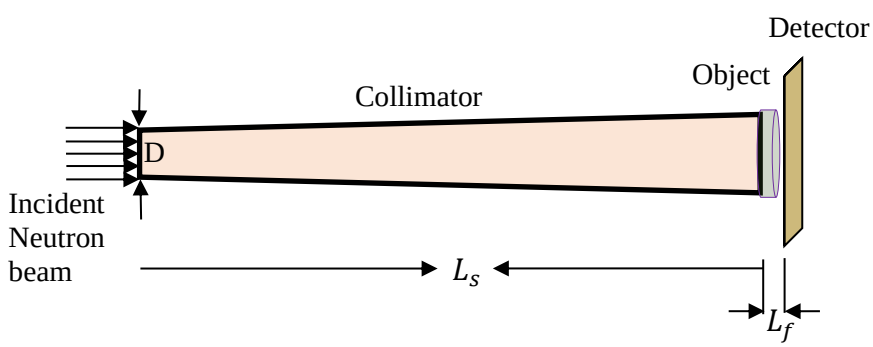

Figure 2.9.1. A schematic view of a collimator for a typical neutron radiography setup.

Thermal neutron imaging can be performed in a variety of ways; direct and indirect film radiography techniques, imaging plate, real-time neutron radiography, or digital neutron radiography, which can be advanced to neutron tomography. For a typical neutron radiography arrangement, the collimator ratio ranges from 20 to 250 [54]. However, for a digital neutron radiography setup, higher values (>100) have been recommended to avoid the beam impurities resulting in less image unsharpness.

2.10 Signal to Noise Ratio (SNR)

The signal from a scintillation screen, either a scintillating crystal or a high purity thin Gadolinium metal foil, results in a digital image on a computer screen or a radiographic film, representing the internal structure of the object. This signal can be expressed as a point spread function (PSF). The point spread function (PSF) measures the response of an imaging system to a point source or object. The PSF is a more general term for impulse response functions, with the PSF referring to the initial signal as seen via a focused optical viewfinder. It is the spatial domain equivalent of the optical transfer function of the imaging system. PSF can be expressed by the following equation (2.14).

$$PSF\ (r,\ r_0) = S \cdot\ \delta(r - r_0)\ , \qquad (2.14)$$

where S is the transfer coefficient and $\delta(r - r_0)$ is the Dirac delta function. To illustrate the image properties, the edge response function (ERF) and line spread function (LSF) are applied to define the resolution of the acquired image. These two functions are generated as a line curve with the gray values at the object edge region of the radiographic image as a function of distance or pixel [55].

The gray variations can be utilized to find the signal-to-noise ratio (SNR), which is defined as equation (2.15) [56].

$$SNR = \frac{Expected\ power\ in\ the\ signal}{Expected\ power\ in\ the\ noise} \tag{2.15}$$

Generally, SNR can also be defined in terms of the ratio between the average signal value μ_{sig} and the standard deviation σ_{bg} in the following equation (2.16), derived for the images shown in Figure 2.10.1.

$$SNR = \frac{\mu_{sig}}{\sigma_{bg}} \tag{2.16}$$

However, the SNR and Contrast to Noise Ratio (CNR) present a similar demonstration on a 2D gray value image [57]. CNR can be defined using the amplitude of gray values A_{sig} and the standard deviation σ_{bg}, as expressed in equation (2.17) [58].

$$CNR = \frac{A_{sig}}{\sigma_{bg}} \tag{2.17}$$

In terms of decibel (dB) unit, the SNR of a radiographic image can be evaluated as equation (2.18).

$$SNR = 20 \times log_{10}\left(\frac{\mu_{sig}}{\sigma_{bg}}\right) \tag{2.18}$$

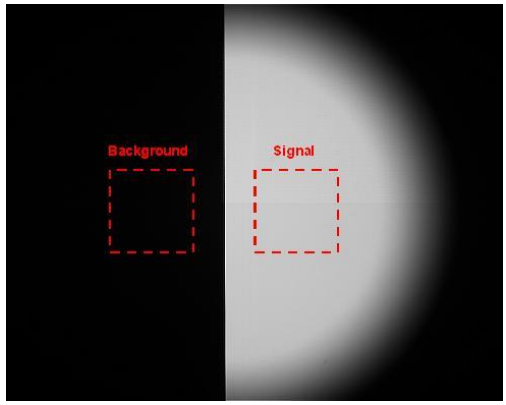

Figure 2.10.1. A half-moon or knife-edge test target image is typically used in image analysis (Electro Optical Industries, Inc. dated 08.09.18).

2.11 Scintillation Light Yield

The scintillation light yield of a scintillator is the number of photons created per unit of absorbed energy, often denoted as Photons/MeV. The size of the bandgap, E_g (between valence and conduction band) of a scintillator constrains the maximum light production Y_{ph} as defined by the following equation (2.19):

$$Y_{ph} = \frac{SQ}{\beta\, E_g} \times 10^6, \qquad (2.19)$$

where S and Q denote the transfer and quantum efficiency of luminescence, respectively, and β is a parameter whose value is ranging between 2 and 3 for broad bandgap substances. The highest E_g values are found in fluoride compounds, whereas the lowest values are found in sulfides, and oxides (borates) are in between.

2.12 Crystalline Structure of $Li_6Y(BO_3)_3$

$Li_6Y(BO_3)_3$ crystallizes in the monoclinic $P2_1/c$ space group. The structure is three-dimensional. There are six inequivalent Li^+ sites, while each one is bonded with O^{2-} atoms. There is a spread of Li–O bonds that distance from 1.87 to 2.57 Å depending on the positions. There are three inequivalent B^{3+} sites. In all B^{3+} sites, B^{3+} atoms are bonded in a trigonal planar geometry to three O^{2-} atoms. There are one shorter (1.37 Å) and two longer (1.40 Å) B–O bond lengths. Each Y^{3+} is bonded to eight O^{2-} atoms to form distorted YO_8 hexagonal bipyramids that share corners with two LiO_4 tetrahedra, corners with two LiO_5 trigonal bipyramids, edges with two equivalent YO_8 hexagonal bipyramids, an edge-edge with one LiO_4 tetrahedra, and edges with four LiO_5 trigonal bipyramids. There is a spread of Y–O bond distances ranging from 2.32 to 2.55 Å. A schematic view of a unit $Li_6Y(BO_3)_3$ crystal is shown in Figure 2.12.1 [59].

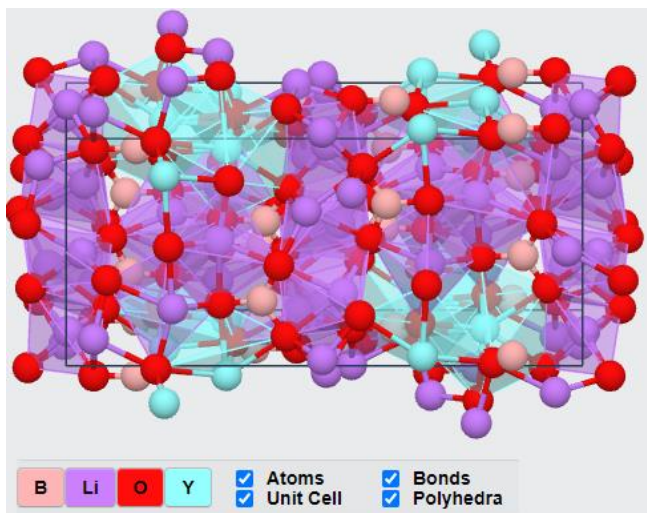

Figure 2.12.1. A schematic view of the crystalline structure in a unit cell of $Li_6Y(BO_3)_3$. (Materials Data on $Li_6Y(BO_3)_3$ (SG:14) by Materials Project)

2.13 Single Photon Counting Technique

Due to the limits of our measurement setup, we are unable to determine the scintillation light production of a crystal with a long decay period ($> 25\ \mu s$). Generally, the decay periods of the molybdate and tungstate groups are long (several microseconds). The technique can be applied to the 4f-4f transition luminescence, where the decay time can vary from a few microseconds to a few milliseconds. At room and low (300 to 10 K) temperatures, the scintillation light yields of these crystals are determined using a single-photon counting technique based on the recording of individual photons from a scintillation event. This approach is particularly advantageous for slow scintillation material because it avoids signal accumulation. Individual photons are recorded after noise and background (without a source) are measured at ambient temperature and subtracted from the original data point (data with a source). The total time required to collect data for each data point is 300 seconds, and the overall count is divided by this time to obtain the count per second.

The irradiation source is a ^{90}Sr (β^-) source, and the photon detector is a multi-alkali Hamamatsu PMT (R7400U-20 Series) with a 16 mm diameter and 12 mm length. According to the company specification, the PMT responds between 232 and 900 nm, with the highest quantum efficiency (QE) of ~18% at 495 nm, as illustrated in Figure 2.13.1. To compare the absolute light yields of two distinct crystals, the quantum efficiency of the PMT must be corrected. A few data points are retrieved from the QE spectrum and then interpolated to generate additional data points for QE rectification using excel software.

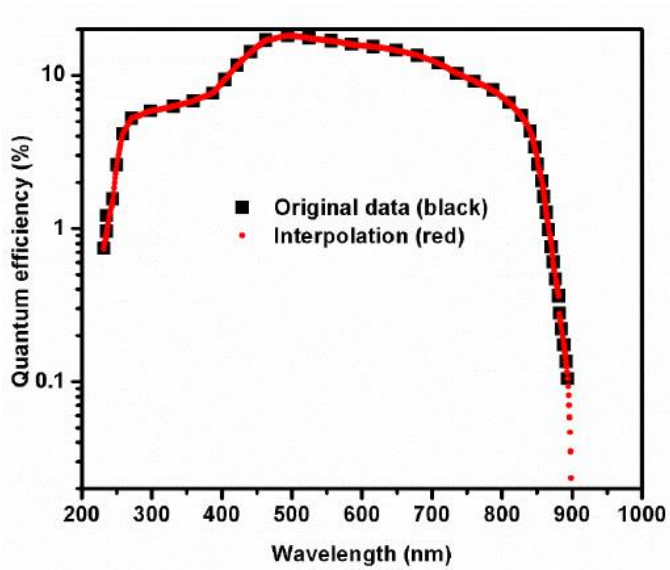

Figure 2.13.1. The interpolated QE data from the original QE spectrum of multi-alkali PMT [60].

Emission weighted quantum efficiency can be formulated as equation (2.20) [61,62].

$$\overline{\mathrm{EMQE}} = \frac{\int QE(\lambda) E_m(\lambda)\, d\lambda}{\int E_m(\lambda)\, d\lambda}, \tag{2.20}$$

where $QE(\lambda)$ denotes the quantum efficiency of the PMT as a function of wavelength (λ), and $E_m(\lambda)$ is for the probability of emission from at the same position of the wavelength (λ). The mean photon energy of the crystal can be evaluated as equation (2.21).

$$\overline{\upsilon} = \frac{\int \upsilon\, E_m(\upsilon) d\upsilon}{\int E_m(\upsilon) d\upsilon}, \tag{2.21}$$

where $\overline{\upsilon}$ is the energy in eV varying inversely proportional to the wavelength (λ) as (1240/λ) and $E_m(\upsilon)$ is the probability of emission at the frequency (υ). Likewise, $d\upsilon$ can be calculated as $\frac{1240\times d\lambda}{\lambda^2}$.

In this method, the number of photoelectrons (N_{pe}) generated by the PMT at a certain temperature for the sample crystal is calculated. The number of photons (N_{ph}), generated in the crystal under the excitation of a radioactive source, produces the photoelectrons (N_{pe}) in the PMT. So, the emission weighted quantum efficiency ($\overline{\mathrm{EMQE}}$) can also be formulated as equation (2.22).

$$\overline{\mathrm{EMQE}} = \frac{N_{pe}}{N_{ph}} \tag{2.22}$$

That gives the scintillation light yield as equation (2.23)

$$N_{ph} = \frac{N_{pe}}{\overline{\mathrm{EMQE}}} \tag{2.23}$$

The single-photon counting technique was effective for crystalline samples to determine the light yield avoiding the electronic noise and pile-up events in a long decay process [61,62].

2.14 Pulse Shape Discrimination

Different kinds of incident radiation can be discriminated against using the pulse shape discrimination (PSD) ability of the scintillator. Different types of radiation have significant influences on the scintillation decay time constants. The PSD approach discriminates between neutron and γ-ray pulses based on variation in the generated pulse forms. In the present experiment, the

approach was applied to distinguish the moderated thermal neutron pulse from the photomultiplier (PMT) noise and the γ-ray responses on the scintillator. The ratio between the accumulated charges in the tail of the pulse and the overall charge in the entire pulse, Q_{ratio} was computed to determine the type of radiation. For the same total charge deposited, the Q_{ratio} for neutron pulses should be greater than the Q_{ratio} for γ-ray pulses.

The PSD ratio indicates the percentage of relative charges acquired throughout the prompt and delayed windows as a percentage of the overall charge contribution [63]. It can be defined as in equation (2.24).

$$\text{PSD ratio} = W_1/ (W_1 + W_2), \tag{2.24}$$

where W_1 and W_2 denote the accumulated charges obtained in the prompt and delayed periods, respectively. W_1 is the accumulation from the apex of the pulse immediately followed by W_2 without any time delay.

2.15 PMT Noise

Thermionic electrons, ejected from the photocathode of the PMT are the major cause of such PMT noise. Usually, these photocathodes are alkali metals and can eject electrons after heating by a marginal amount, resulting from high voltage injection. It is why, with the increase of high voltage, the PMT noise is also increased. The pulses produced by this mechanism correspond to a single photoelectron; their amplitude is restricted to the lowest end of the energy scale. The rate at which these pulses are observed is proportional to the area of the photocathode. Such electron flow is also named dark current. Typically, at room temperature, this spontaneous emission rate is in the range of $10^2 \sim 10^4\ electrons \cdot cm^{-2} \cdot s^{-1}$.

Chapter 3. Experimental Section

3.1 Glass Fabrication

Three different series of glass samples were fabricated using the conventional melt-quenching technique. The constituent materials contained thermal neutron-sensitive elements like Li, B, and Gd, while Eu^{3+} ions were doped to make the glass compounds luminescent. The fabricated glass compositions are (30-x)B_2O_3:60Li_2O:10Gd_2O_3:xEu_2O_3 (BLiGd:xEu, x = 0.05 ~ 1.5 mol%), (55-x)B_2O_3:10SiO_2:25Gd_2O_3:10CaO:xEu_2O_3 (BSiGdCaO:xEu, x = 0.1 ~ 0.45 mol%), and (30-x)B_2O_3:60Li_2O:10Y_2O_3:xEu_2O_3 (BLiY:xEu, x = 0.05 ~ 0.5 mol%), which are tabulated elaborately in Table 3.1 [64–66]. About 20 grams of every batch composition were ball milled and fully ground in an agate mortar after the constituent compounds were mixed in their appropriate molar ratios. These homogeneous mixtures were poured into an alumina crucible and heated inside an electric furnace (Hantech, S 1700) for up to two hours at temperatures of 1200° C for BLiGd:xEu and BLiY:xEu, 1400° C for BSiGdCaO:xEu. The hot melt was quenched on a preheated stainless-steel mold and annealed for around five hours at 500 °C to diminish thermal stresses. Optimal optical clarity was achieved once the glasses cooled down and were polished. The thicknesses of the glass samples for the thermal neutron imaging experiment were adjusted based on the penetration depth of thermal neutrons via the contents within, and the varied thicknesses are 0.7, 0.6, and 2.3 mm for BLiGd:xEu, BSiGdCaO:xEu, and BLiY:xEu, respectively [67].

Table 3.1. The molar ratio of constituents in three different glass compositions.

Sl. no.	B_2O_3	Li_2O	SiO_2	Gd_2O_3	CaO	Y_2O_3	Eu_2O_3	Acronym
	Concentrations in mol%							
01	30-x	60	-	10	-	-	x = 0.05, 0.10, 0.15	BLiGd:xEu
02	55-x	-	10	25	10	-	x = 0.05, 0.15, 0.25, 0.35, 0.45	BSiGdCaO:xEu
03	30-x	60	-	-	-	10	x = 0.01, 0.05, 0.50, 1.00, 1.50	BLiY:xEu

3.2 Crystal growth by the Czochralski method

3.2.1 The Czochralski method

The Polish scientist Jan Czochralski developed the idea of pulling a piece of crystal out of its melt against gravitational force in 1917 [68]. Later, the technique was modified to make it better and more useful to many researchers. Schmid, Polanyi, Von Gomperz, and Mark modified this procedure further by cooling the grown crystal. Teal and Little extracted the crystal from the melt using a clock mechanism. They used this technology to grow the first germanium crystal in 1948. They adjusted this process in order to regulate crystal formation by varying the crystal shape, pulling force, and rotation speed. The significant technological advancement in this technology was the automated development of crystals through the crystal's weight control. The automated control of the growing procedure enabled precise control of the diameter. The weight of the crystal may be determined by weighing it from above using the drawing rod or by balancing the crucible [69]. The pulling rod approach seems to be the most effective and is frequently used for directly weighing crystals. Zinnes created the computer methods to enhance the control system [43]. For the growth of different halides, oxides, metals, and compound semiconductors, the Czochralski method is utilized. The crystal growth technique is dominant over others because it allows precise control of the crystal diameter by adjusting the molten temperature as well as the growth rate by controlling the rotation speed and pulling rate. This approach enables the production of dislocation-free crystals at a reasonably rapid rate.

Figures 3.2.1 and 3.2.2 depict the schematic design and photographic image of the Czochralski growth setup. It is primarily composed of an alternating high-radio-frequency (RF) coil that is used to melt the material by heating the metallic crucible. The RF coil is positioned at the center of the chamber. The platinum or iridium crucible is filled with powders of the substance to be grown. The crucible is placed in the middle of the coil to be heated and melt the charged material. Thermal shielding surrounds the crucible to minimize heat loss. The constant flow of water cools the outer part of the furnace. The importance and process of hydrodynamics can be found in the literature [70]. Largely, the crystal is grown in an air or inert gaseous atmosphere (e.g., Ar, N_2, CO_2, etc.). A window is positioned at the top portion of the chamber to monitor the growth process. For proper growth management, the seed should be properly secured in the seed-containing rod, which should be attached to the pulling rod. Centering the coil, crucible, and seed is also crucial for the proper management of the growth process.

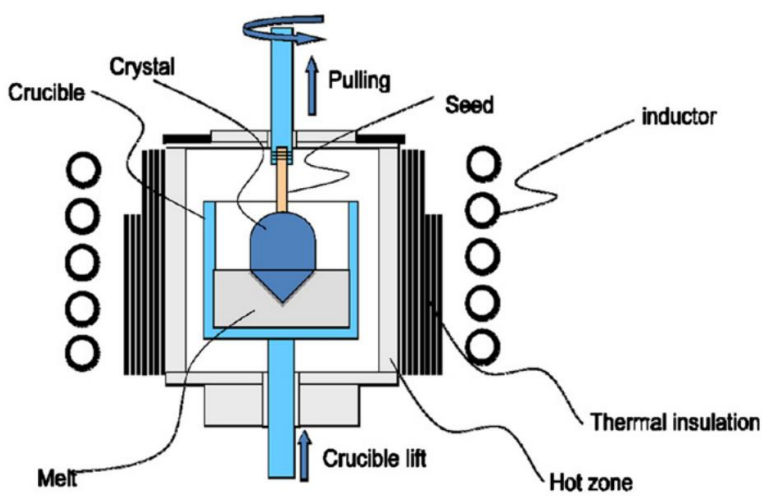

Figure 3.2.1. A schematic view of the Czochralski crystal growth technique where the inductor is indicated for a high radio-frequency coil [71].

Figure 3.2.2. A photographic image of the Czochralski crystal growth apparatus.

3.2.2 Sample Preparation

In order to prepare the intended crystalline form of the LYBO compound, a proper stoichiometric ratio of high purity compounds was required for weighing and mixing thoroughly. It is why, Li_2CO_3 (99.998%, Alpha Aesar), Y_2O_3 (99.99%, Alpha Aesar), and H_3BO_3 (99.99%, Alpha Aesar) were weighed according to the molar concentrations as mentioned in the following equation (3.1) [72].

$$6Li_2CO_3 + Y_2O_3 + 6H_3BO_3 \rightarrow 2Li_6Y(BO_3)_3 + 6CO_2 \uparrow + 9H_2O \qquad (3.1)$$

Dy_2O_3 (99.99 %, Alpha Aesar) and Pr_2O_3 (99.99 %, Metal Rare Earth Ltd.) were added at the stoichiometric ratio of Y_2O_3 to activate the compound

with dopants like dysprosium (Dy) and praseodymium (Pr) ions. The optimum concentration of Dy_2O_3 doping, according to a previous report, was 4 mol%, which was used in this experiment [73]. However, the content of Pr_2O_3 varied from 0.5 to 3 mol% (0.5, 1.0, 2.0, and 3.0 mol%) to determine the optimum doping concentration. The powders were weighed and then ball milled for 12 hours in sterilized plastic containers with ceramic balls (Wisemix ball mill, Daihan, Korea).

3.2.3 Sintering to form Polycrystalline sample

The well-mixed powders were transported to an alumina crucible, and sintering was performed in the DK746 furnace (STI, Korea). To avoid the abrupt evaporation of boric acid, the temperature was gradually increased to 200° C at a rate of 30° C/h and then maintained for 4 hours. The temperature was then raised to 650° C at a steady rate of 50° C/h for 12 hours, after which it was cooled to room temperature at the same speed. The sintered powders were finely pulverized with an agate mortar and pestle before being sintered for another 24 hours at 750° C at a rate of 50° C/h. For powder X-ray diffraction (PXRD) analysis and X-ray induced luminescence measurements, the produced phosphors were thoroughly grounded. After being assured of proper crystalline phases by PXRD analysis, the well-sintered samples were then carried to be poured into the platinum crucible for crystal growth using the Czochralski method.

3.2.4 Crystal growth process

The Czochralski process was utilized to grow single-crystal samples of a pure and doped LYBO. The doped LYBO crystals contained 4 mol% of Dy_2O_3 and 1 mol% of Pr_2O_3 impurity concentrations as the optimum

activation ratios. After being deposited in a platinum crucible with a diameter and height of 3 cm, the polycrystalline powders were carried to a Czochralski puller for further processing. To find the seed crystal of pure LYBO, the sintered powder of pure LYBO compound was used with a platinum rod as a seed to pull out a small size single crystal of pure compound. Later, this grown crystal sample was cut and used to grow further pure and doped LYBO crystals of larger sizes. The seed crystal, on the other hand, was cut in line with the growth direction from the ingot of pure LYBO. The seed crystal was 15 mm long while the width and thickness were 2 mm × 2 mm. It was attached to the pulling axis with the use of a platinum rod as well as platinum thread. A proper positioning keeps the crucible with the sample at the center of the RF coil under the same alignment of the seed crystal during rotation without angular displacement. The Czochralski chamber was sealed and vacuumed slowly before argon gas was filled to make the atmosphere inert. Then the power was raised slowly to start heating the platinum crucible. The power and temperature were monitored properly to find the exact melting condition. The material was observed to be melted congruently and consistently at 850° C, which corresponds to the DTA plot from the previous work [17]. To eliminate the surface bubbles, the temperature had to be raised to 880° C and held there for two hours. The seed is then slowly put into the melt while the rotation speed is maintained at 9 rpm. It was a success when the crystal pulling started at a rate of 0.5 mm/h after 30 minutes of monitoring for stable conditions. By keeping these conditions constant and modifying the heating and cooling rates very slowly, a crystal ingot with a diameter of 13 mm and a length of 22 mm was grown. After that, the crystal was allowed to cool to room temperature over the course of 48 hours at variable rates to avoid any thermal shock.

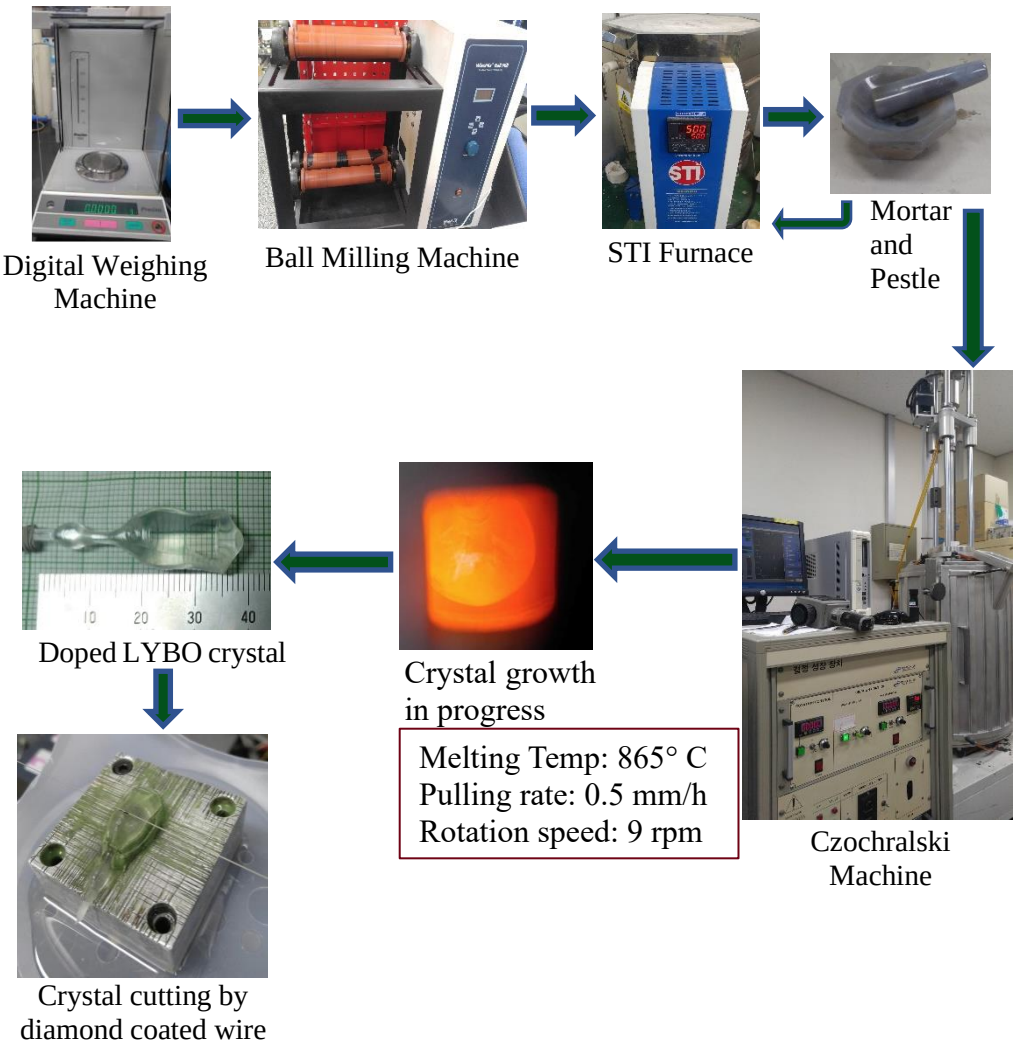

Figure 3.2.3. The flow chart shows the entire crystal growth process from sample weighing to crystal ingot cutting with a diamond-coated wire saw.

However, because of the window on the shielding arrangement (which was used to monitor and control the growth process), it was not possible to avoid the thermal shock that happened during the cooling phase, resulting in a surface fracture of Pr^{3+} doped LYBO crystal. All grown crystal

ingots were cut with a diamond-coated stainless-steel wire saw and optically polished for luminescence and scintillation tests, yielding exceptional pieces of transparent crystals. The entire crystal growth process is shown schematically in Figure 3.2.3. The grown crystal ingot and the transparent crystal pieces of pure LYBO after cutting and polishing are shown in Figure 3.2.4, 4 mol% Dy^{3+} doped LYBO crystal in Figure 3.2.5, and 1 mol% Pr^{3+} doped LYBO crystal in Figure 3.2.6.

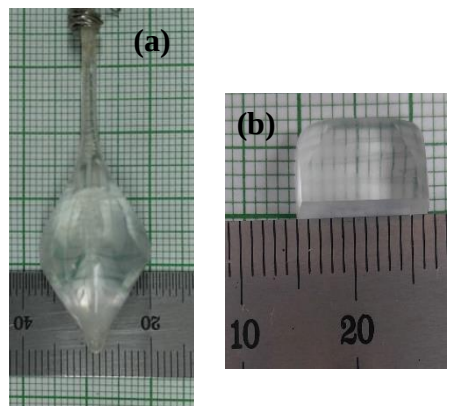

Figure 3.2.4. (a) The grown ingot of the pure LYBO crystal and (b) the piece of pure LYBO crystal after cutting and polishing with dimensions of 11.5 mm × 6 mm × 6 mm.

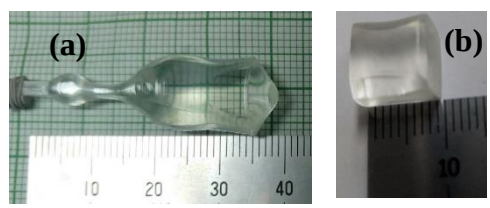

Figure 3.2.5. (a) The grown ingot of the 4 mol% Dy^{3+} doped LYBO crystal and (b) the piece of 4 mol% Dy^{3+} doped LYBO crystal after cutting and polishing with dimensions of 9 mm × 8.5 mm × 7 mm.

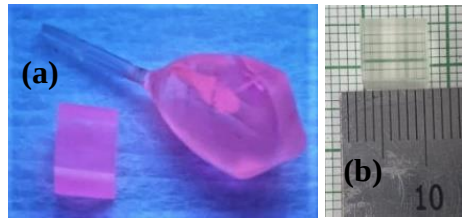

Figure 3.2.6. (a) The as-grown 1 mol% Pr^{3+} doped LYBO crystal ingot with a separated piece under UV (254 nm) excitation and (b) optically polished piece with dimensions of 7 mm × 7 mm × 7 mm.

3.3 Experimental techniques and Instruments

3.3.1 X-Ray induced emission spectroscopy

The emission spectra of the produced crystals were examined under X-ray exposure at room temperature to investigate their X-ray detection and luminescence capabilities. The X-rays were produced via a tungsten anode X-ray tube manufactured by DRGEM. The samples were optically polished, connected to optical fiber on one side, and wrapped with 250 µm thick Teflon tape on the other. The sample was bombarded with X-rays produced by the tube at an operative voltage of 100 kV and a current of 2 mA. Figure 3.3.1 depicts a schematic design and a photographic representation of the X-ray triggered measurement setup. The light emission from the samples was recorded using a QE65000 ocean optics spectrometer coupled with a calibrated optical fiber of 400 µm diameter. Light yield nonlinearity, absolute irradiance, and spectral sensitivity correction were calibrated for the spectrometer arrangement. The collected data was analyzed using a window-based program (origin 8).

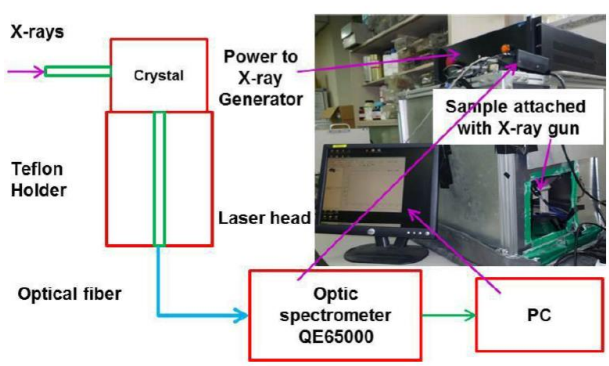

Figure 3.3.1. A schematic diagram with the photographic view that explains the arrangement of X-ray induced luminescence spectroscopy system [43].

3.3.2 Direct Film Neutron Imaging

Additionally, the direct film neutron radiography method was used to irradiate each of these glass samples without using any material other than an empty ball pen refill. Glass samples were employed as neutron converters instead of 25 μm thick 4N pure Gadolinium (^{157}Gd) converter foil. An AGFA Structurix DSFW industrial X-ray film was used to capture the pictures within the NR cassette [74,75]. To begin, the glass samples were individually irradiated for 5 minutes to determine their neutron-induced luminescence. The empty ball pen nib was then used as a sample for examination after a ten-minute irradiation period during which the glass specimen worked as a neutron-to-photon converter. Metal and plastic can be found in the empty ball pen refill and can be considered a good sample for the test. The X-ray films employed in this experiment are very sensitive to visible light, allowing for the performance of this experiment. The irradiated films were developed, fixed, and dried following recommended procedures, which can be found elsewhere [2,75].

3.3.3 Beam Purity Assessment

The beam purity indicator (BPI) was used to determine the fractional content of thermal and scattered neutrons, as well as γ-rays, in the available neutron beam. Our experiment followed the procedures outlined in the American Society for Testing and Materials (ASTM) standard E 2003-10 (2014) [9]. The technique is still in use to classify radiography facilities, allowing for a comparison of the quality of various neutron radiography facilities worldwide. The BPI is comprised of a TFE-fluorocarbon block that accommodates two boron nitride disks, two lead disks, and two cadmium

wires inside, as shown in Figure 3.3.2 (a) [76,77]. The shim design and structure of the sensitivity indicator (SI) that is made of acrylic, aluminum, and lead components, are shown in Figure 3.3.2 (b) [76,77]. The optical density, D at these positions in the neutron radiographic film was measured with the digital densitometer. The gray value density at the respective positions from the radiographic film, the D parameters are listed below [9,77] :

a) $D_1 = D_B\ (Lower) = Density\ under\ the\ lower\ boron\ nitride\ disc$
b) $D_2 = D_B\ (Higher) = Density\ under\ the\ upper\ boron\ nitride\ disc$
c) $D_3 = D_L\ (Lower) = Density\ under\ the\ lower\ lead\ disc$
d) $D_4 = D_L\ (Higher) = Density\ under\ the\ upper\ lead\ disc$
e) $D_5 = D_H = Background\ film\ density\ in\ the\ center\ of\ the\ hole$
f) $D_6 = D_T = Film\ density\ under\ the\ teflon\ body$

(a)

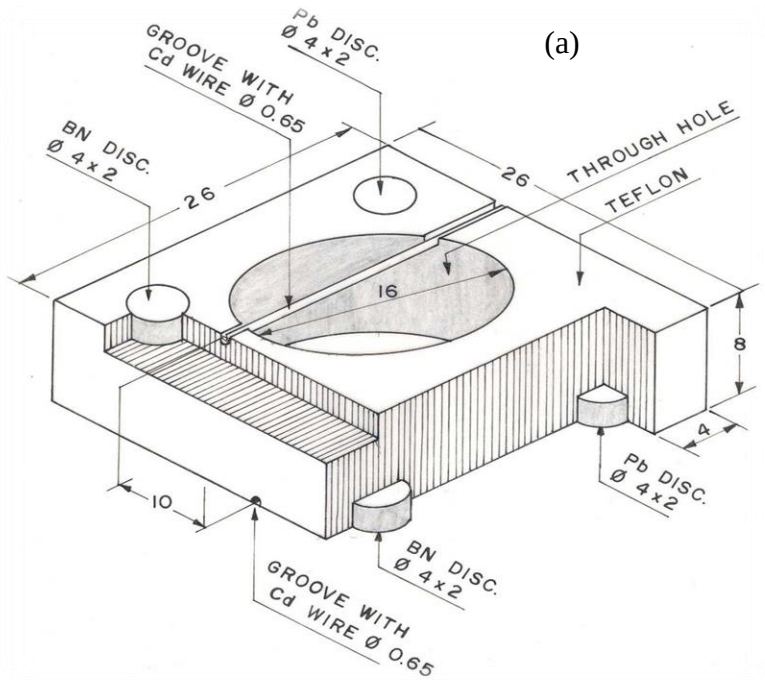

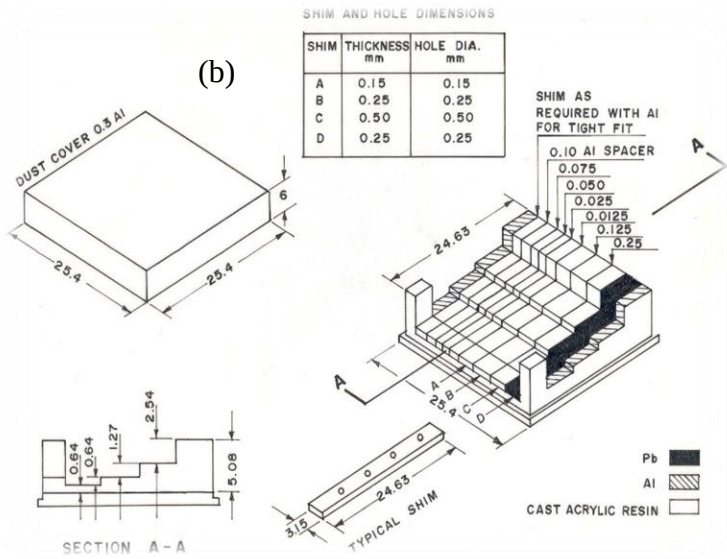

Figure 3.3.2. The schematic diagram of the inside structure of (a) a beam purity indicator (BPI) and (b) a sensitivity indicator (SI).

The desired fractional contributions of different types of radiation in the beam can be calculated using the following relationships:

I. Thermal neutron content, $C = \frac{D_5 - (higher\ value\ of\ D_1 and\ D_2)}{D_5} \times 100$

II. Scattered neutron Content, $S = \frac{D_1 - D_2}{D_5} \times 100$

III. Gamma Content, $\gamma = \frac{D_6 - (lower\ value\ of\ D_3 and\ D_4)}{D_5} \times 100$

IV. Pair production contribution, $P = \frac{D_3 - D_4}{D_5} \times 100$

BPI was irradiated to the thermal neutron beam with two different 4N pure Gadolinium (^{157}Gd) converter foils (25 and 50 μm thick) and AGFA Structurix DSFW industrial X-ray film to obtain the most reliable data at this

step. The process of developing and fixing the irradiated X-ray films can be found in the literature, which was followed accordingly [75].

3.3.4 Optical Density Measurement

The change in image density, ΔD at each point of the sample image with the film background, can be calculated using the following formula:

$$\Delta D = D_{bk} - D_{image}\ , \qquad (3.2)$$

where

D_{bk} = optical density of the film background,

D_{image} = optical density at the point of the sample image.

Hence using equation (3.2), the average optical density difference between film background radiographic image of the sample, $(\Delta D)_{av}$ can be written as,

$$(\Delta D)_{av} = D_{bk} - D_{image(av)}, \qquad (3.3)$$

where

$D_{image(av)}$ = average optical density of each level of image points on the horizontal line of the sample image.

We have measured the optical density of the neutron radiographic images of the samples by a digital densitometer (Model – 07-424, S-23285 Victorian Inc., USA).

3.3.5 Phase Analysis

In this work, the produced crystals are alkali orthoborates, which have three or four constituent compounds. As a result of inhomogeneous mixing or stoichiometry fluctuation, the formation of several phases is reasonable. X-ray

diffraction (XRD) inspection was used to confirm the construction of a single crystalline phase in the synthesized crystalline powder samples. An X-ray diffractometer XPERT-MED with Cu $K\alpha_1$ radiation of wavelength 0.154 nm was used to study the powders. The XRD data of the samples were collected on the scale of Bragg angle (2θ) in the range from 10°~70° at a scan rate of 0.01°/s and step size of 0.03° in the gonio scan mood (Panalytical X'Pert Pro, UK) to authenticate the crystalline phase. During measurements, an X'Celerator solid-state detector was used, allowing a faster scanning rate with better resolution. The generator was set at a tube current of 35 mA and a voltage of 40 kV for X-ray production. To validate the data from Pr^{3+} doped LYBO crystal, it was refined using Rietveld refinement analysis with Material Analysis utilizing Diffraction (MAUD) software [78].

3.3.6 Photoluminescence

The photoluminescence excitation and emission spectra were examined using an Agilent Cary Eclipse Fluorescence Spectrophotometer to understand the luminescence mechanism in synthesized glass and grown crystal samples. Figure 3.3.3 shows an image of the instrument as well as a schematic representation of it. A pulsed xenon source is paired with a 0.125 m Cerny-Turner monochromator in this spectrometer. A monochromator was used to disperse the light emitted by the sample crystal, and PMT was used to gather it. The emission and excitation spectra of the samples were corrected for the transmission of the monochromator and the quantum efficiency of the PMT. Window-based software Origin 8 was used to evaluate the acquired data.

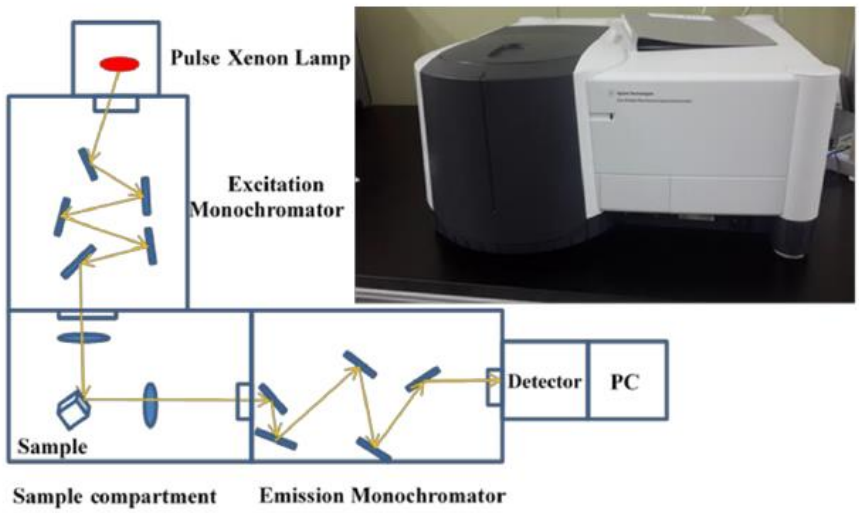

Figure 3.3.3. A schematic diagram with a photographic view explains the arrangement of the photoluminescence system [43].

3.3.7 Laser-Induced Luminescence

Figure 3.3.4 depicts a laser-induced luminescence measurement setup. An MPL-F-266nm-20mW-10ns laser source was used to irradiate the 1 mol% Pr^{3+} LYBO crystal sample for the study. The UV solid-state laser was used to stimulate the sample crystal at a 266 nm wavelength with 10 ns pulses. The pulse energy was constant at 4.13 µJ. The Ocean Optics QE65000 spectrometer was used to measure the emission spectrum accompanied by optical fiber. The laser-induced emission spectra were plotted and studied with Origin 8, a Windows-based software. The whole process of measurement is quite analogous to the X-ray-induced emission measurement technique, except for the excitation source, which is a laser here.

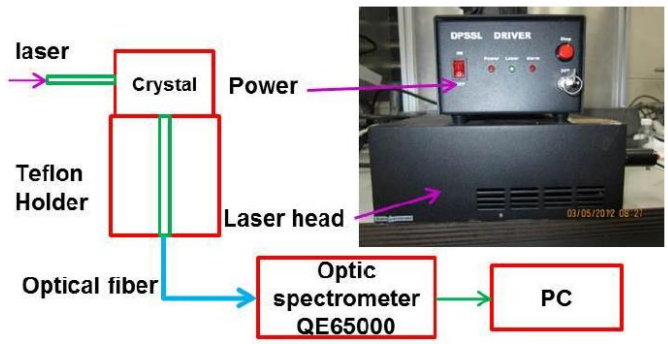

Figure 3.3.4. A schematic diagram with the photographic view that explains the arrangement of the laser-induced emission measurement system [79].

3.3.8 Digital Neutron Radiography

Three glass samples with the optimal activator concentration for luminescence were assessed utilizing the thermal neutron beam at the tangential beam port of the 3 MW BAEC TRIGA Research Reactor, operated at 2.2 MW. The facility has an L/D ratio of 60 and an estimated neutron flux of $1.038 \times 10^{7}\ n \cdot cm^{-2} \cdot s^{-1}$. The present scintillation detector screen is a 0.22 mm thick Ag-doped compound layer composed of ^{6}LiF and ZnS mixed at a 4:1 ratio. Due to the enrichment with ^{6}Li, it is anticipated to have a low X-ray and γ-ray absorption cross-section but a high thermal neutron absorption cross-section. The facility is equipped with a cooled digital CCD camera from the Chroma CX3 series, model CX-1600E, equipped with a C-mount motorized zoom lens with a 20× magnification and an aperture of f =1.8.

3.3.9 Thermal Neutron Induced Luminescence Measurement

The luminescence output was determined by passing the neutron beam through scintillating glasses as well as throughout the shape of a printed

pattern, as seen in Figure 3.3.5 (a). The design was drawn on a 200 $g \cdot m^{-2}$ (ISO:536-2012) tracing paper with a 53.5% translucency (ISO:2469-2014). The paper was positioned just below the commercial screen to allow the emitted light to pass through and reach the camera lens reflected by the mirror within the digital neutron radiography (DNR) box. These photos were used to determine the signal-to-noise ratio (SNR) [80,81]. To test the thermal neutron-induced luminescence of the manufactured glass samples, the scintillation screen was substituted with individual glass samples to conduct identical imaging with a different pattern, as shown in Figure 3.3.5 (b). Seven horizontal lines and eight curved lines of varying thickness are included in the 6 mm length. The design has been reduced in size to correspond to the scintillating area of all glass samples. To replace the present commercial scintillation screen, a ~3 cm thick poly-boron shield with a window for one glass has been designed. The window on the shield enables the thermal neutron beam to pass only through the glass samples. Figure 3.3.5 (c) shows the optical capture of the ballpen refill that used as a sample for direct film neutron radiography with glass samples as converter instead of Gd foil.

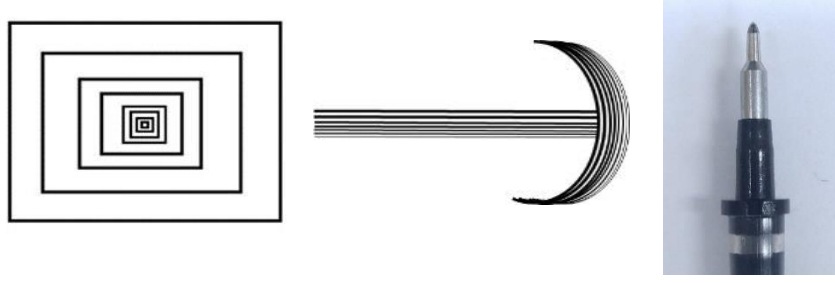

(a) (b) (c)

Figure 3.3.5. Patterns were printed and used as a phantom in a digital neutron imaging system to examine (a) the existing scintillation screen, (b) test glass samples, and (c) ballpen refill as a sample for direct film neutron radiography.

3.3.10 Scintillation measurements using Single Photon Counting Technique

A ^{90}Sr radiation source as a β^- emitter of 100 µCi activity was utilized in this experiment [82]. For a collimated β^- particle beam from the source, a ~1 mm thick lead sheet with a ~2 mm diameter hole was structured. A few layers of 250 µm thick Teflon sheet were wrapped around the crystal as a light reflector (except the top and bottom). The ^{90}Sr source was completely bound to one side of the crystal using a Teflon sheet. For adjusting the crystal height with the source and mounting it next to the light guide, a ~3 mm thick copper plate is employed. Thermal grease is used to connect a copper plate to the cold plate at the bottom. Thermal grease is used on top and bottom of the aluminum foil for thermal coupling with the copper plate and crystal, and a thin layer of aluminum foil is used on top of the copper plate to prevent light loss from the bottom side of the crystal. The crystal is set so that the top side of the crystal has the most surface area exposed to a quartz light guide.

As a photon detector, a Hamamatsu R7400U-20 Series Photomultiplier Tube (PMT) was employed. Using silicone optical grease (EJ550, Eljen Technology), the PMT is optically connected to the quartz light guide. The quartz light guide and the PMT are held together by the black tape and a Teflon holder to reduce the light loss. The signal from the PMT is transmitted to a pre-amplifier (with a gain of 50) and then to a 10-channel PMT counter from Notice Korea. Figure 3.3.6 depicts a schematic diagram of the experimental setup. To reduce noise, the top section of the cryogenic system is covered with 2-3 layers of aluminum foil and black cloth during both room and low-temperature data acquisition. The measured counts at room

temperature from LYBO:Dy^{3+} crystal were compared to CMO crystal to match the slow decay process since the compound was previously reported to have a decay period in microseconds [83].

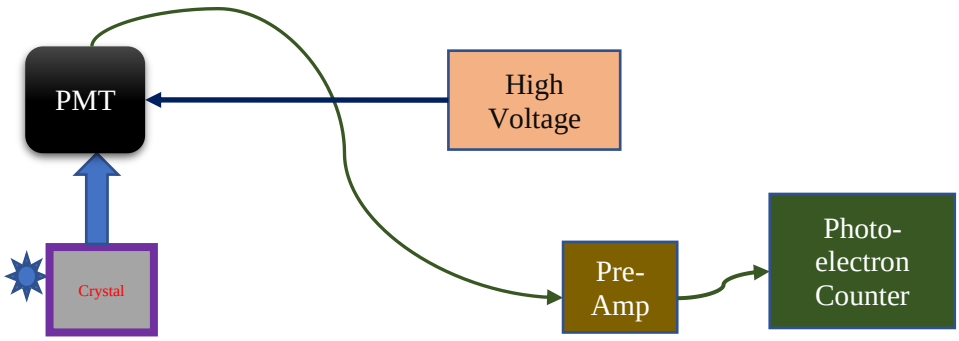

Figure 3.3.6. A schematic experimental arrangement of the single-photon counting technique.

3.3.11 α-particle and γ-ray spectroscopy

The LYBO:Pr^{3+} crystal sample (7 mm × 7 mm × 7 mm) was bombarded with α-particles and γ-ray from ^{241}Am and ^{60}Co sources, respectively, for scintillation measurements. A weak ^{252}Cf source was employed independently using the same configuration for the neutron detection experiment. Between the sample crystal and the source, a ~3 cm thick paraffin wax layer was applied that thermalized the spontaneous fission neutrons. On the photocathode of the Hamamatsu R6233-100 photomultiplier tube, the crystal was optically linked using silicone optical grease. The output signals were digitized using a 500 MHz flash analog to digital converter (FADC) (Notice Korea) [84]. The PMT was biased at -1300 V. To completely reconstruct each photoelectron pulse, the flash analog to digital converter module possesses a resolution of 12 bits and transforms at a processing rate of

500 MS/s over a duration of up to 10 μs. The recorded pulses were processed offline using a customized C++ code compiled and executed in the ROOT package to determine the pulse shape discrimination (PSD) ratio for the observed radiation, pulse height spectrum, and scintillation decay time estimate [85,86].

3.3.12 ICP-OES and Optical Properties

To conduct an inductively coupled plasma – optical emission spectroscopy (ICP-OES) investigation, a Perkin Elmer Inc. Optima 7300 V spectrometer with a 40 MHz radiofrequency was utilized to generate argon plasma. A Spectrophotometer (Shimadzu UV-3600 model) was used to acquire absorption spectra in the UV–Vis-NIR range at room temperature. A JASCO V-650 spectrophotometer was used to test the crystal sample's transmittance, with a systematic error of 0.3 percent in photometric accuracy.

3.3.13 Decay Time Measurements

The multiparameter character of radiative emission of light following excitation is usual. As a result, the goal of a measurement is to collect data on as many factors as feasible. The fluorescence (or phosphorescence) lifespan provides an absolute (concentration-independent) metric and enables the creation of a dynamic image of the fluorescence (or phosphorescence), both of which contribute to its acceptance. These time-resolved radiative emission measurements can be quantified using the following equation (3.4) (origin 8), where a three components exponential decay function is estimated.

$$I = A_1 \exp(-\frac{t_1}{\tau_1}) + A_2 \exp(-\frac{t_2}{\tau_2}) + A_3 \exp(-\frac{t_3}{\tau_3}) + I_0, \qquad (3.4)$$

where I and I_0 denote the intensities at times, t and 0. A_1, A_2, and A_3 are the integrated areas, calculated for the fluorescent lifetime components τ_1, τ_2, and τ_3, respectively. The contribution from each decay component was quantified using the respective integrated area (A_1, A_2, and A_3) of each emission phase. Due to the discontinuity in the change of a single component with respect to temperature, the trend of change in decay behavior can be observed using the average decay time. The average decay time can be obtained using equation (3.5).

$$\tau_{\mathrm{av}} = \frac{A_1 \times \tau_1^2 + A_2 \times \tau_2^2 + A_3 \times \tau_3^2}{A_1\tau_1 + A_2\tau_2 + A_3\tau_3} \qquad (3.5)$$

Chapter 4. Results and Discussions

4.1 Synthesis and Characterization of Borate Glasses for Thermal Neutron Scintillation and Imaging

4.1.1 X-ray Induced Luminescence

The radioluminescence characteristics of BLiGd:xEu, BSiGdCaO:xEu, and BLiY:xEu with different doping concentrations of Eu^{3+} were observed under X-ray excitation, as shown in Figure 4.1.1 (a), (b), and (c), respectively. Eu^{3+}-ions characteristic emission is evident in the X-ray induced emission spectra from BLiGd:xEu, BSiGdCaO:xEu, and BLiY:xEu samples with peaks at 578, 591, 611, 652, and 701 nm due to the forbidden 4f-4f transition from $^5D_0$ to $^7F_0$, $^7F_1$, $^7F_2$, $^7F_3$, and $^7F_4$ energy states. In Figure 4.1.1 (b), the energy level splitting was observed at 591 nm due to the $^5D_0 \rightarrow {}^7F_1$ transition which can be explained by the stark effect phenomenon. However, the highest intensity peak is observed at 611 nm due to the transition of $^5D_0 \rightarrow {}^7F_2$ levels for all samples. One sample was identified from each variety, considering the highest emission intensity under X-ray excitation for the purpose of neutron imaging. The selected samples were BLiGd:0.5Eu, BSiGdCaO:0.45Eu, and BLiY:1.5Eu, as evident in Figures 4.1.1 (a), (b), and (c), respectively. The emission intensities of these samples were compared in Figure 4.1.2 for more contrast on the effect of photon emission efficiencies under X-ray absorption. The BSiGdCaO:0.45Eu glass was found to emit the highest X-ray induced light in comparison to the other two samples.

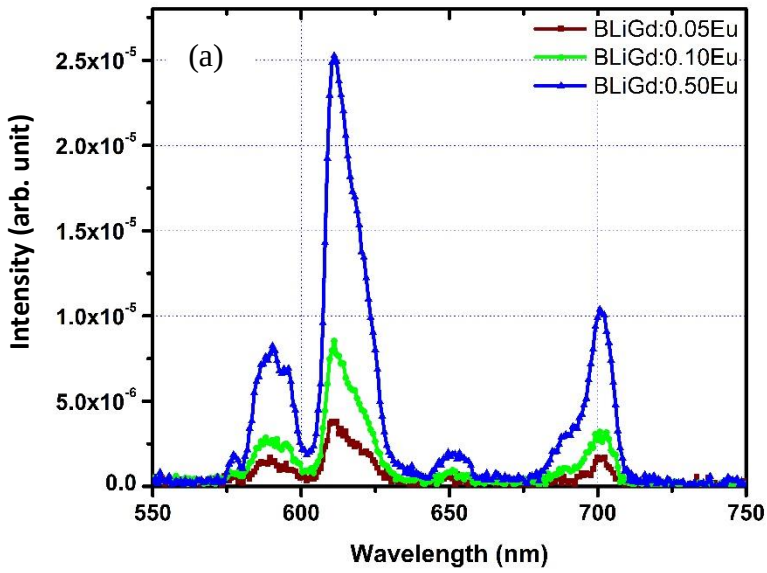
(a)
BLiGd:0.05Eu
BLiGd:0.10Eu
BLiGd:0.50Eu
Intensity (arb. unit)
2.5x10-5
2.0x10-5
1.5x10-5
1.0x10-5
5.0x10-6
0.0
550
600
650
700
750
Wavelength (nm)

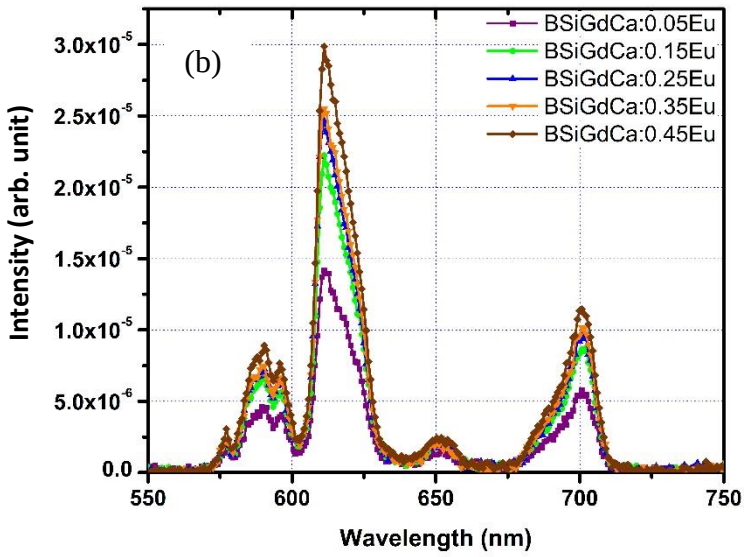
(b)
BSiGdCa:0.05Eu
BSiGdCa:0.15Eu
BSiGdCa:0.25Eu
BSiGdCa:0.35Eu
BSiGdCa:0.45Eu
Intensity (arb. unit)
3.0x10-5
2.5x10-5
2.0x10-5
1.5x10-5
1.0x10-5
5.0x10-6
0.0
550
600
650
700
750
Wavelength (nm)

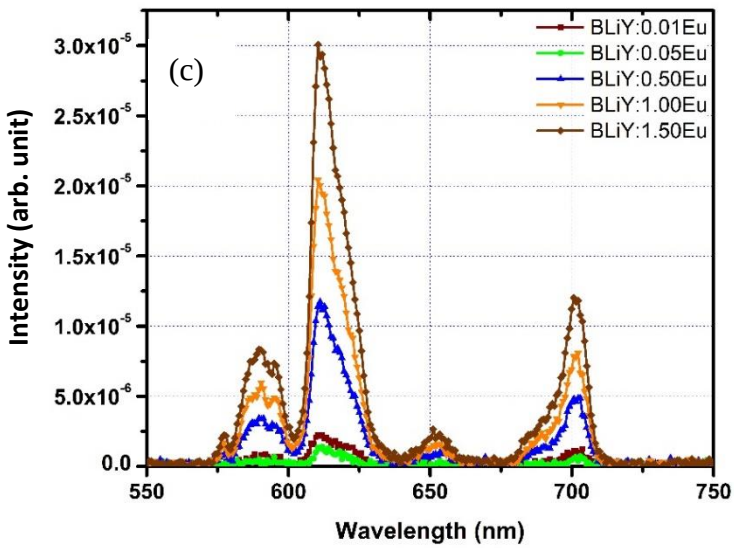

Figure 4.1.1. X-ray Luminescence comparison spectrum varying with different doping concentrations of Eu^{3+} in (a) BLiGd and (b) BSiGdCaO (c) BLiY compositions.

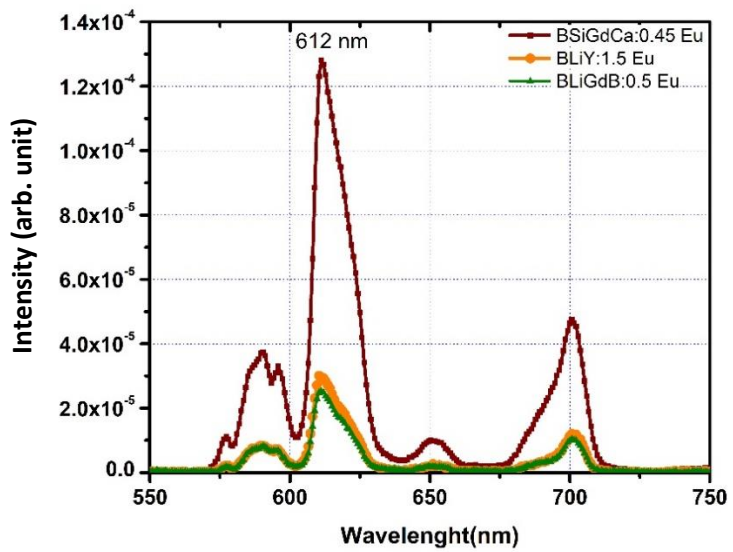

Figure 4.1.2. X-ray luminescence spectra of BSiGdCaO:0.45Eu, BLiGd:0.5Eu, and BLiY:1.5Eu glasses.

4.1.2 UV-Vis Excitation Spectra

The photoluminescence (PL) excitation spectra were measured in the UV-Vis spectral range from 200 to 550 nm for the Eu^{3+} ion emission at 611 nm from BSiGdCaO:0.45Eu, BLiGd:0.5Eu, and BLiY:1.5Eu glasses. A comparative presentation of these spectra is depicted in Figure 4.1.3. The characteristic eight UV-Vis excitation peaks of Eu^{3+} ions are observed in all these spectra due to the transitions from $^7F_0$ to $^5H_4$ at 320 nm, $^7F_0$ to $^5D_4$ at 364 nm, $^7F_0$ to $^5G_4$ at 384 nm, $^7F_0$ to $^5L_6$ at 393 nm, $^7F_0$ to $^5D_3$ at 413 nm, $^7F_0$ to $^5D_2$ at 462 nm, $^7F_0$ to $^5D_1$ at 527 nm, and $^7F_1$ to $^5D_1$ at 534 nm [87]. The charge transfer band (CTB) is also observed at 226, 228, and 245 nm for BLiY:1.5Eu, BLiGd:0.5Eu, and BSiGdCaO:0.45Eu glass samples respectively [88,89]. Another two peaks are also visible in the excitation spectra of BSiGdCaO:0.45Eu and BLiGd:0.5Eu samples, which are centered at 274 and 311 nm due to the Gd^{3+} -ions transitions from $^8S_{7/2}$ to $^6I_{9/2}$ and from $^8S_{7/2}$ to $^6P_{7/2}$ [88]. The Gd^{3+} -ion excitation bands for Eu^{3+} -ion emission bands are evidence of an effective energy transfer from the host matrix to activator ions in these glass networks that subsequently lead to a higher light yield.

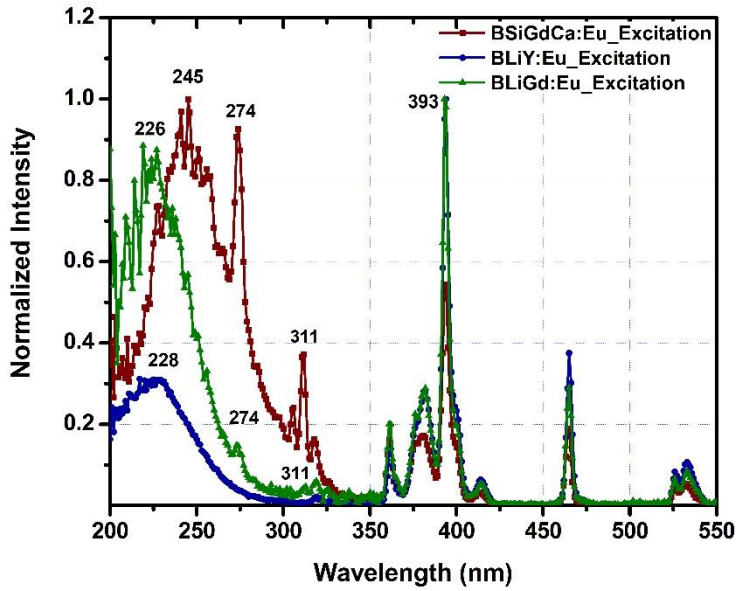

Figure 4.1.3. Photoluminescence excitation spectra of BSiGdCaO:0.45Eu, BLiGd:0.5Eu, and BLiY:1.5Eu glasses.

4.1.3 Beam Quality Evaluation

An optical photographic image and a respective schematic diagram of BPI are shown in Figures 4.1.4 (a) and (b) respectively. The neutron radiographic images of BPI and SI under the irradiation with thermal neutron beam using a 25 μm thick Gd foil as a converter are shown in Figures 4.1.4 (c) and (d).

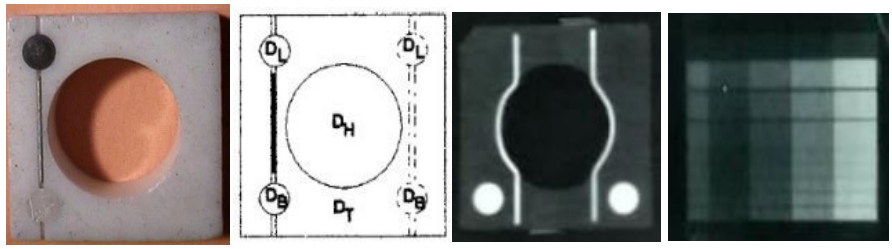

(a) (b) (c) (d)

Figure 4.1.4. (a) The photographic image and (b) the schematic view of BPI. The neutron radiographic images of (c) BPI and (d) SI were taken at 2.2 MW power of a reactor using 25 μm thick Gd foil as a converter.

In the direct film radiography technique, converter foil was used to transform the transmitted (through the sample) neutron beam into conversion electron, which interacts with the emulsion layer on the industrial radiographic film, breaking the chemical bonding and recording the incident response. The NR images of BPI and SI are obtained using two Gd converter foils of thickness 25 and 50 μm under thermal neutron irradiation for 4 and 6 minutes, respectively. The measured optical densitometric parameter values, "D" at respective positions of NR images, were acquired. The NR images of BPI and SI in 250 kW with 25 μm thick Gd foil were taken in 2007 under irradiation of 25 minutes and compared the values of those standards with the images of the present experiment. The evaluated values of thermal neutrons, γ-rays, scattered neutrons, and pair production contents define the quality of the incident beam. The identified number of gaps and holes define the image clarity within the system. The L/D ratio can be responsible for the image blur effect. The calculated values of these parameters using equations as reported in **section 3.3** are presented in Table 4.1.1.

Table 4.1.1. The measured gray values of optical densitometric parameters of BPI.

Reactor Power	**250 kW**	**2.2 MW**	**2.2 MW**
Thickness of Gd foil	**25 µm**	**25 µm**	**50 µm**
D_B (lower)	0.715	0.91	0.69
D_B (higher)	0.845	0.93	0.71
D_L(lower)	1.92	2.17	1.64
D_L(higher)	1.94	2.29	1.65
D_H	2.15	2.52	1.88
D_T	1.98	2.24	1.71

According to Table 4.1.2, the thermal neutron content measured at 250 kW reactor power with 25 μm thick Gd foil was higher than the present measurement. The content is higher with 50 μm thick Gd foil irradiating for extra time to achieve a similar gray value level at the background. There can be a few reasons for this incident, such as burnt fuel positions, neutron moderator temperature, etc. during the experiment. The γ-rays contents in the thermal neutron beam can depend on the operating power of the reactor. The collimator under operation is also responsible for generating γ-rays due to irradiation for an extended period. The consumed time for sample irradiation

may vary with the level of γ -rays doses. The detected γ -ray content within the neutron beam thus can change as evident in Table 4.1.2. The scattered neutron contents increased with the irradiation time and were invariant to the operating power of the reactor. The pair production content is dependent on the amount of high-energy γ -rays incident with the beam that is invariant on the reactor operation power and exposure time. However, the identified numbers of gaps and holes are indicating the L/D ratio of the facility is appropriate for film neutron imaging.

Table 4.1.2. The calculated value of thermal neutrons, γ -rays, scattered neutrons, pair production contents from BPI, and identified number of gaps and holes from SI.

	Thermal Neutron, NC	**Gamma, γ**	**Scattered Neutron, S**	**Pair Production, P**	**Gap, G**	**Hole, H**
250 kW, 25 μm	65.81 %	2.79 %	6.04 %	0.93 %	7	6
2.2 MW, 25 μm	58.33 %	1.98 %	0.79 %	4.70 %	7	6
2.2 MW, 50 μm	61.70 %	3.70 %	1.06 %	0.53 %	7	6

4.1.4 Scintillation Screen Luminescence

To check the photon emission efficiency of the existing commercial Ag-doped ^{6}LiF and ZnS neutron scintillation screen and the compatibility with the camera, the thermal neutron beam was opened for 2.5 minutes to find a sufficient number of photons from the scintillation screen that could transmit

through the printed paper and reach the camera. Figure 4.1.5 (a) shows the raw image without correction, which contains a lot of white spots (also known as γ -ray spots). The beam source and environmental γ -rays are responsible for these spots. After required software (ImageJ) corrections, the concentric pattern could be identified on the image, as shown in Figure 4.1.5 (b). However, the obtained pattern was magnified from the original one, and a ghost line can also be observed. For graphical presentation, the obtained gray values from the marked section of Figure 4.1.5 (b) were plotted as distance in the number of pixels versus gray value intensity in Figure 4.1.6. A high amount of distortion in signal was observed at the position of the printed line. The distortion value at the signal region varies from 26 to 65%. The signal-to-noise ratio (SNR) was measured as reported in Table 4.1.3 comparing the inverse gray value variation following equation 4.1 [90].

$$\text{SNR (db)} = 20 \times \log_{10} \{\text{Signal Intensity (Inverse Gray Value)} \div \text{Average Std. Dev. everywhere (Inverse Gray Value)}\} \quad (4.1)$$

The gray value is inversely proportional to the signal intensity or the optical density of the NR image. To normalize such an effect, the inverse value was considered to calculate the SNR value.

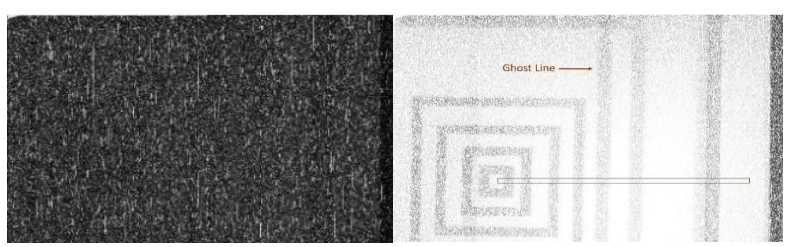

(a) (b)

Figure 4.1.5. The neutron radiographic image of the concentric pattern (a) without correction and (b) after software correction.

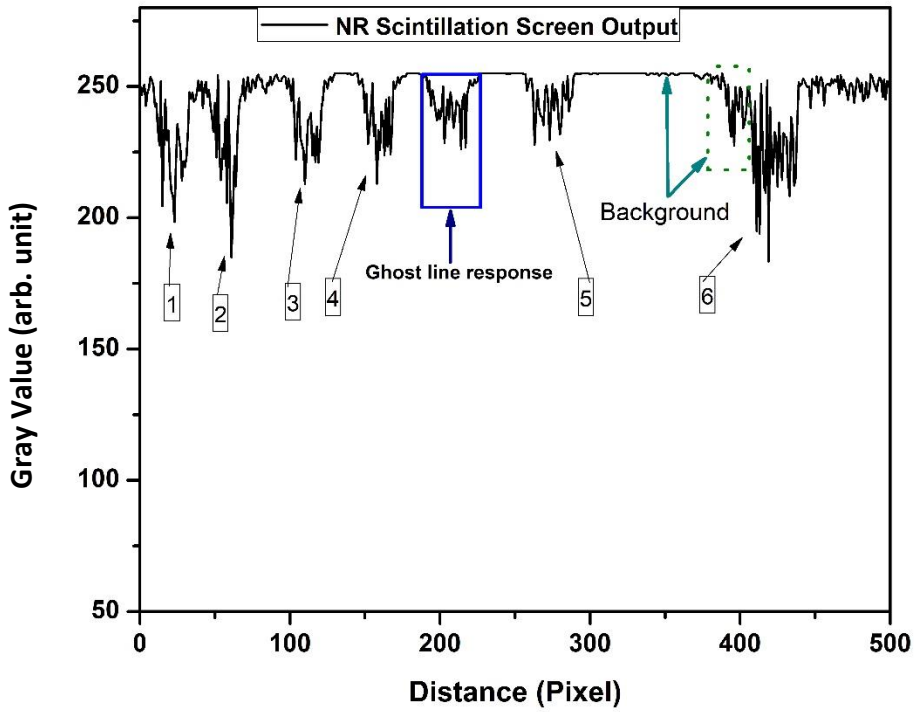

Figure 4.1.6. The graph shows the gray value intensity as the curve of the original pattern, which is expected to be imitated in the image developed from scintillation screen photons.

Table 4.1.3. The gray value variation over different positions and calculated SNR from the scintillation screen

Parameters	Line 1	Line 2	Line 3	Line 4	Line 5	Line 6	Background
Average Gray Value	223.6 ± 13.9	221.7 ± 17.1	229.4 ± 7.8	234 ± 8.3	242.2 ± 6.9	219.2 ± 15.5	249.9 ± 5.4
Inverse Value ($\times 10^{-3}$)	4.5 ± 0. 3	4.5 ± 0.3	4.4 ± 0.2	4.3 ± 0.2	4.1 ± 0.2	4.6 ± 0.3	4.0 ± 0.1
Individual SNR (dB)	25.83	25.83	25.63	25.43	25.02	26.02	
Average SNR (dB)	25.63						

The glass samples were irradiated for 5 minutes to construct a digital neutron radiographic image similar to the scintillation screen. However, the printed pattern was not identified as observed for the scintillation screen. Lower light output from these glass samples can be determined from the measurement. A few white spots were found on the image which is the result of the γ -ray contents from the beam coming from the tangential beam port of the research reactor as well as from the environment. The SNR measurements could not be performed as the printed pattern was not visualized even after image correction.

4.1.5 Evaluation of Glass Samples with the Direct Film Technique

The optical photographic image of BSiGdCaO:0.45Eu glass along with thermal neutron radiographic images recorded on the industrial film after five minutes of irradiation are depicted in Figures 4.1.7 (a) and (b) sequentially. Likewise, Figures 4.1.8 (a), (b), and Figures 4.1.9 (a), (b) show the same for BLiGd:0.5Eu glass and BLiY:1.5Eu glass, respectively. The highest average gray value was recorded, 0.29 in the arbitrary unit for BLiGd:0.5Eu glass using a digital optical densitometer. However, this value was not sufficient for further detailed characterization. Among radiographic images irradiated for five minutes, BLiGd:0.5Eu glass emitted the sheerest number of energetic photons, representing the gray value from the radiographic film. Photon emission from BLiY:1.5Eu glass was not up to the level of detection. X-ray luminescence spectra, shown in Figure 4.1.2, narrated the highest photon emission from BSiGdCaO:0.45Eu glass due to X-ray excitation at 2.0 mA tube current and 100 kV operating voltage. At the same time, the other two samples were comparable to each other. These results adequately establish the key fact that the luminescence characteristic due to neutron absorption is incompatible with that of X-ray excitation.

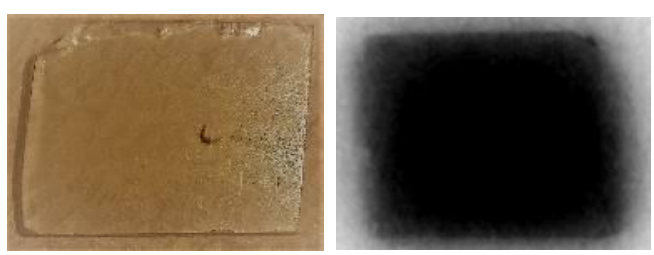

(a) (b)

Figure 4.1.7. (a) A photographic image and (b) an NR image of BSiGdCaO:0.45Eu glass after 5 min irradiation.

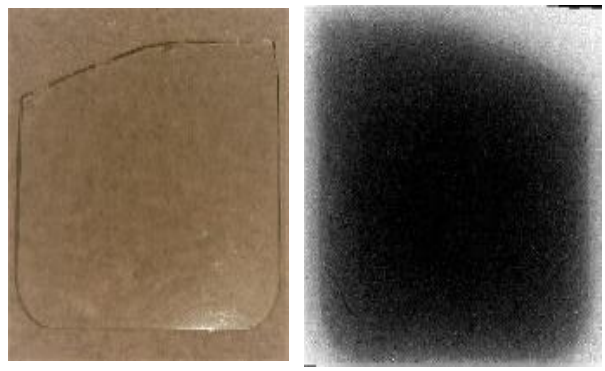

(a) (b)

Figure 4.1.8. (a) A photographic image and (b) R image of BLiGd:0.5Eu glass after 5 min irradiation.

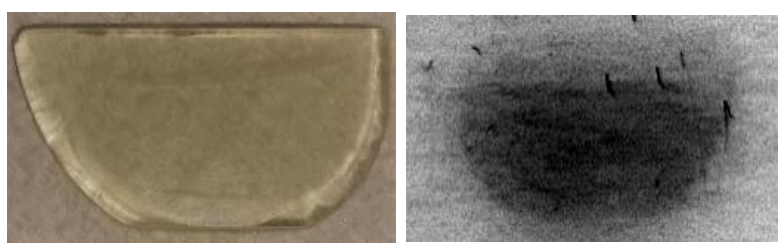

(a) (b)

Figure 4.1.9. (a) A photographic image and (b) an NR image of BLiY:1.5Eu glass after 5 min irradiation.

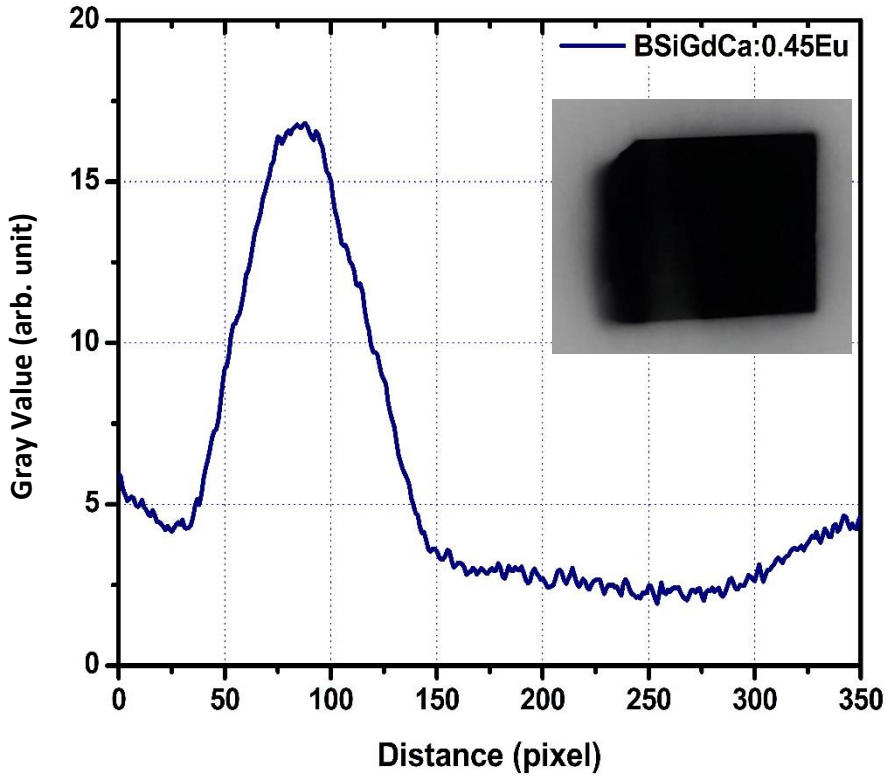

Figure 4.1.10. The NR image (Inset) and the corresponding graphical interpretations of BSiGdCaO:0.45Eu glass with ball pen refill as a sample after 10 min irradiation.

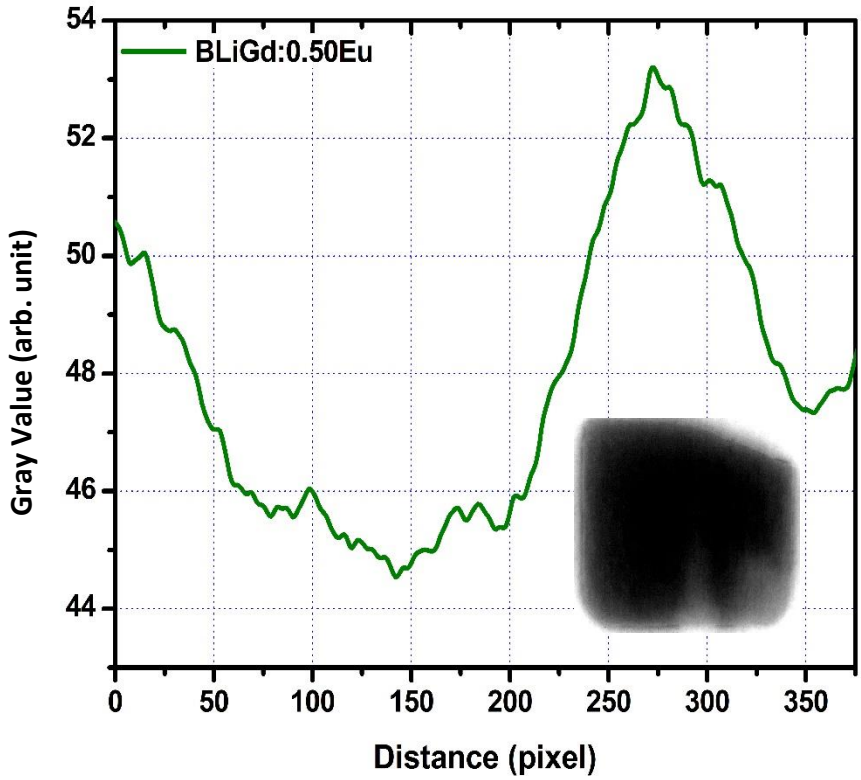

Figure 4.1.11. The NR image (Inset) and the corresponding graphical interpretations of BLiGd:0.5Eu glass with ball pen refill as a sample after 10 min irradiation.

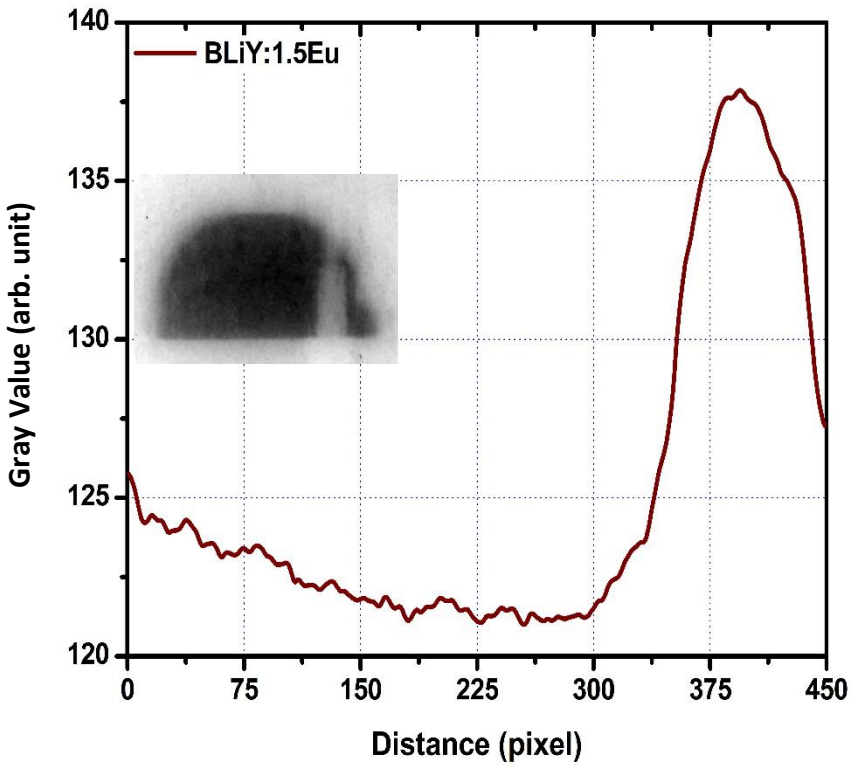

Figure 4.1.12. The NR image (Inset) and the corresponding graphical interpretations of BLiY:1.5Eu glass with ball pen refill as a sample after 10 min irradiation.

To record the higher gray value intensities, the incident beam exposure time was increased to 10 minutes on the next step to obtain the NR image of a ball pen refill as a sample. The ball pen refill contained both plastic and metal, which makes it a suitable candidate as a sample for neutron radiography investigations. The neutron radiographic images of the ball pen refill and their corresponding graphical interpretations from BSiGdCaO:0.45Eu, BLiGd:0.5Eu, and BLiY:1.5Eu glass samples are shown

in Figures 4.1.10, 4.1.11, and 4.1.12, subsequently. The average gray values of the sample NR images are compared in Table 4.1.4. The broad peaks in each graph rendered the ball pen refill and its position though it was impossible to identify clearly with the ordinary vision. BSiGdCaO:0.45Eu provided the highest number of light yields after ten minutes of irradiation among three samples. The light output increased by more than ten times compared to the five minutes NR image. By the standardization of ASTM International, the background average gray value should be 2 to 3. The sample produced the required light yield but failed to visualize neutron radiographic images. The most probable cause of having a dark image is the γ -rays sensitivity of Gadolinium. The thermal neutron beam containing about three percent of γ -ray which is also strong enough in ten minutes to pass through the plastic part of the ball pen refill and eliminate its response from the radiograph. The light yield of BLiY:1.5Eu was also increased by more than three times and the ball pen refill is visualized in the NR image, as shown in Figure 4.1.12. The recorded image with BLiY:1.5Eu glass provided the required variation in gray value intensity after minor software correction that allowed to identify the refill precisely.

Table 4.1.4. NR images and average gray values of the three glass samples.

	Average Gray Value of Glass Samples (arb. unit)		
	BSiGdCaO:0.45Eu	BLiGd:0.5Eu	BLiY:1.5Eu
NR Image in 5 min	0.23	0.29	0.05
NR Image in 10 min	2.46	0.68	0.171

4.2 Luminescence and Scintillation Properties of Dy^{3+} Doped $Li_6Y(BO_3)_3$ Crystal

4.2.1 X-Ray Diffraction Analysis

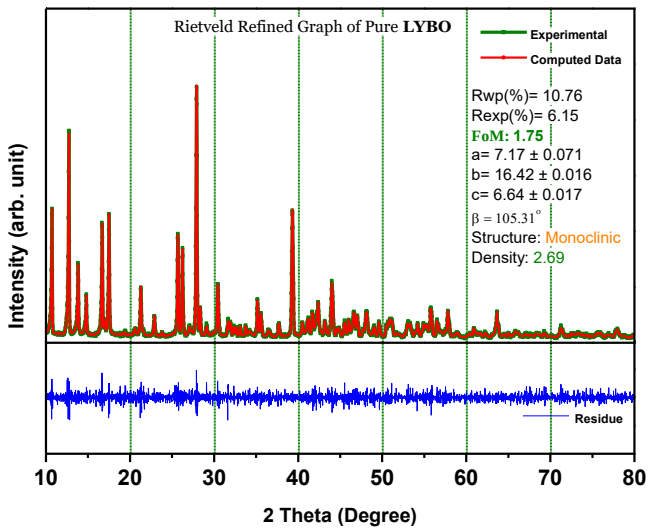

Figure 4.2.1. Rietveld refined plot obtained from powder XRD pattern of pure LYBO crystal sample.

The powder XRD patterns were analyzed with the Rietveld refinement method using the MAUD program in order to confirm the structural uniqueness of the pure $Li_6Y(BO_3)_3$ crystalline material [78]. Comparing the experimental results to the reference (Ref. $98-006-8653$) acquired from the International Center for Diffraction Data is depicted in Figure 4.2.1 [91]. The residual part verifies the diffracted peak locations and intensities in good agreement with the reference. The experimental data and calculated data had a figure of merit of 1.747, indicating excellent agreement too. The sample's unit cell volume and density were determined to be 753.99 $Å^3$ and 2.69 $g \cdot cm^{-3}$, with the lattice parameters: a = 7.17, b = 16.42, c = 6.64,

and β = 105.31°. The measured PXRD patterns on a 2 theta (Degree) scale obtained from the pure and LYBO:Dy^{3+} single crystals were compared with the reference data in Figure 4.2.2. However, a few minor peaks could not be found in the obtained pattern for the LYBO:Dy^{3+} crystalline powder. The most probable reason was the bigger radius of the dopant Dy^{3+} ions than the Y^{3+} ions to replace in the crystal structure. The XRD patterns confirmed the monoclinic crystal structure belonging to a space group of $P2_1/c$ for all grown crystal samples.

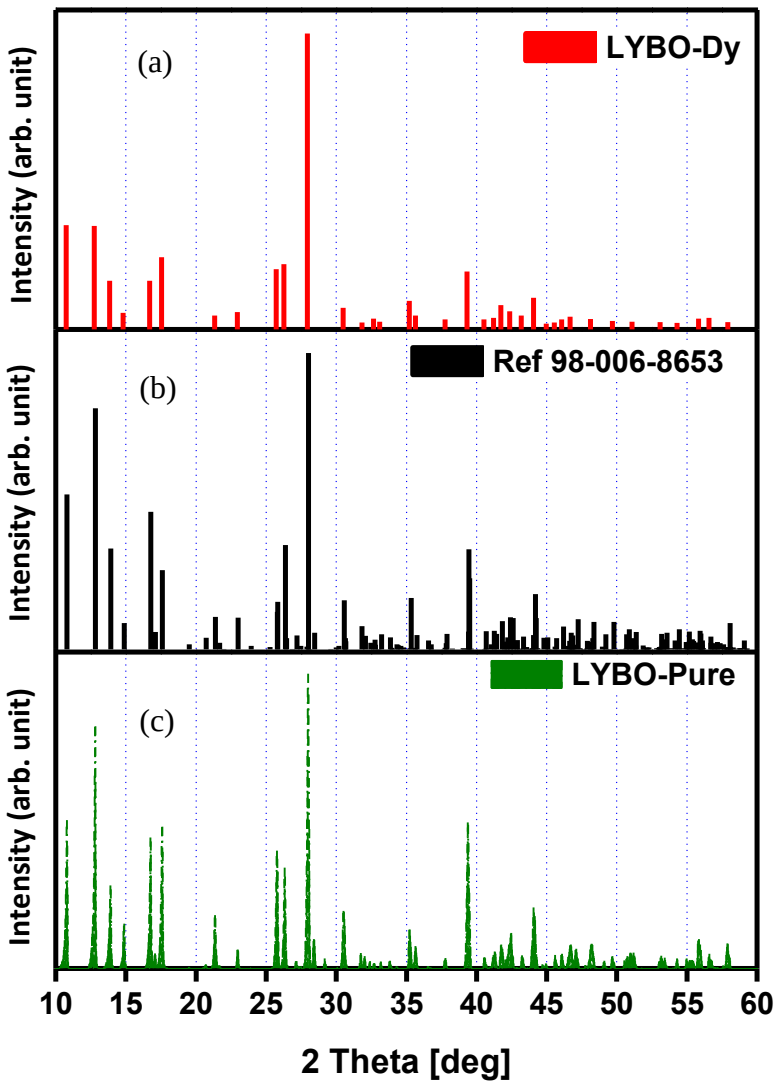

Figure 4.2.2. Powder XRD pattern of (a) LYBO:Dy^{3+}, (b) reference data of the LYBO compound (Ref. 98-006-8653), and (c) LYBO-pure.

4.2.2 X-Ray Induced Luminescence

The measured X-ray induced emission spectra from similarly thick crystal samples of pure and Dy^{3+} -ions doped LYBO are plotted in Figure 4.2.3. The emission intensity from LYBO:Dy^{3+} crystal is ruling out the intrinsic emission intensity of the pure crystal. The data points were normalized to compare in the emission peak positions for both crystals. The pure LYBO appeared with a single peak emission centered at 328 nm. However, the LYBO:Dy^{3+} crystal provided the characteristic emission peak of Dy^{3+} due to 4f-4f transitions while the intense peak was centered at 578 nm. The calculated ratio of the integrated emission peak area for the LYBO:Dy^{3+} to the pure LYBO crystal is 13.5.

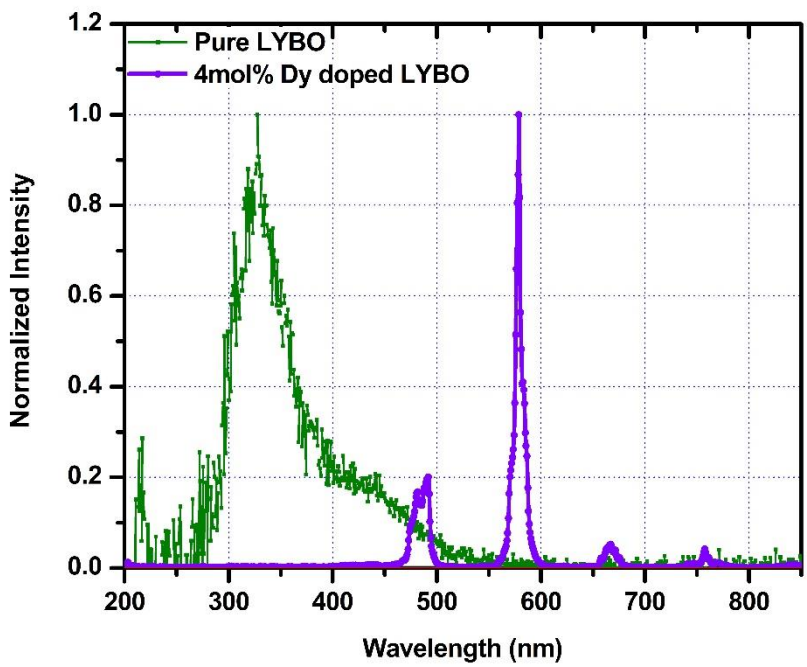

Figure 4.2.3. Comparison of the emission spectra obtained from pure LYBO and LYBO:Dy^{3+} crystals under X-ray excitation.

4.2.3 Photoluminescence

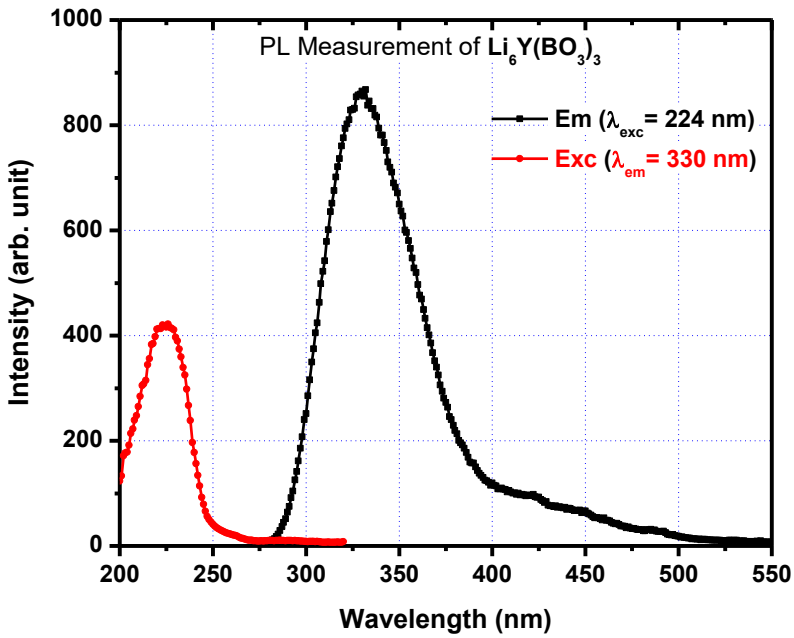

Figure 4.2.4. Excitation (red) and emission (black) spectra were obtained from the Pure LYBO crystal sample measured during the photoluminescence study.

The photoluminescence (PL) excitation and emission spectra of the pure LYBO crystal sample were studied at room temperature and plotted in Figure 4.2.4. A broadband excitation can be observed, summit at 224 nm while the emission band peaked at 330 nm. The PL emission shows a good agreement with the spectrum obtained under X-ray excitation (Figure 4.2.3), which can be considered the intrinsic luminescence of the host crystal.

To obtain the temperature-dependent PL excitation and emission spectra in the UV-NIR range, measurements were carried out with the LYBO:Dy^{3+} crystal. The gradual increase in the intensity of the excitation

spectra for the emission peak at 578 nm with the decreasing temperature from 290 to 10 K is depicted in Figure 4.2.5. Twelve (12) specific excitation peaks were identified in the spectra including the band for charge transfer from O^{2-} to Dy^{3+} -ions [25]. The retrieved peaks over 300 nm agree with the previous reports that demonstrated the studies on Dy^{3+} -ions doped phosphors and glass materials [73,92]. The observed excitation peaks at 241, 255, and 273 nm for the grown single crystal in this experiment support the theoretically calculated values found in the literature [93].

For Dy^{3+} -ions, the lowest electronic energy level is $^6H_{15/2}$ ($4f^9$), from which the excited electron is determined to manifest in the higher energy levels of the $4f^9$ configuration. The charge transfer band (CTB) was identified at 206 nm and other excitation peaks for the corresponding energy level transitions are 241 nm ($^6H_{15/2} \rightarrow {}^2L_{17/2}$), 255 nm ($^6H_{15/2} \rightarrow {}^4P_{3/2}$, $^4F_{3/2}$), 273 nm ($^6H_{15/2} \rightarrow {}^4K_{11/2}$, $^4G_{5/2}$, $^4P_{5/2}$, $^4G_{9/2}$), 295 nm ($^4H_{15/2} \rightarrow {}^4H_{13/2}$, $^4D_{7/2}$), 324 nm ($^4H_{15/2} \rightarrow {}^6P_{3/2}$), 350 nm ($^6H_{15/2} \rightarrow {}^6P_{7/2}$), 364 nm ($^6H_{15/2} \rightarrow {}^4M_{19/2}$, $^6P_{5/2}$, $^4P_{3/2}$, $^4D_{3/2}$), 385 nm ($^6H_{15/2} \rightarrow {}^4I_{11/2}$, $^4F_{7/2}$), 426 nm ($^6H_{15/2} \rightarrow {}^4G_{11/2}$), 448 nm ($^6H_{15/2} \rightarrow {}^4I_{15/2}$), and 474 nm ($^6H_{15/2} \rightarrow {}^4F_{9/2}$), as shown in Figure 4.2.5 [93]. However, the most dominant peak was identified at 350 nm for the $^6H_{15/2} \rightarrow {}^6P_{7/2}$ transition.

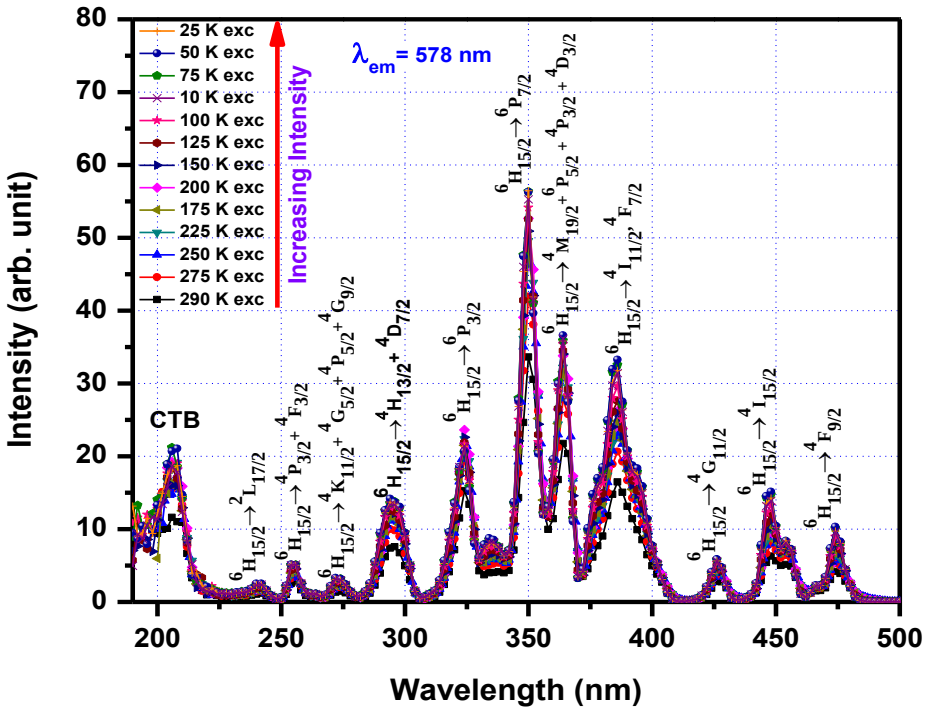

Figure 4.2.5. Temperature-dependent excitation spectra of LYBO:Dy^{3+} crystal.

The temperature-dependent emission spectra, depicted in Figure 4.2.6, were achieved for the excitation at 350 nm due to the transition of $^6H_{15/2} \rightarrow {}^6P_{7/2}$. In the blue region, the first emission peak appeared peaking at 481 and 490 nm, caused by the magnetic dipole (MD) transition from $^4F_{9/2}$ to $^6H_{15/2}$ [92]. Ion-ion cross-relaxation process is common in this region due to absorption from $^6H_{15/2}$ to $^4F_{9/2}$ energy level. A combination of transitions from $^4F_{9/2}$ and $^6H_{15/2}$ to $^6H_{5/2}$ level finally conclude to such polarized emission as the observed dual peak [94,95].

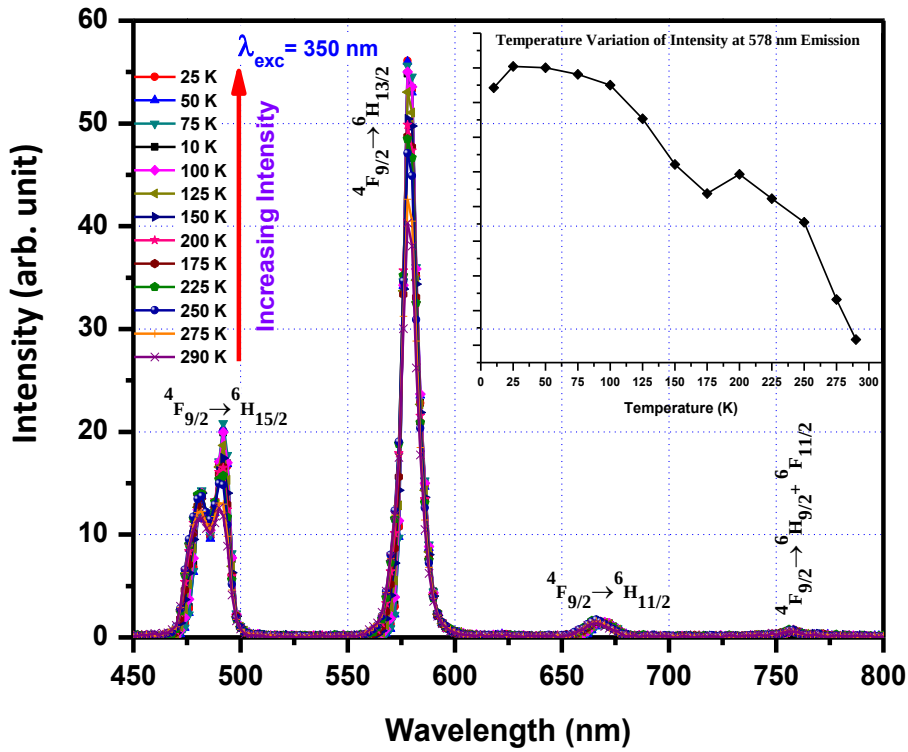

Figure 4.2.6. The temperature-dependent emission spectrum of LYBO:Dy^{3+} crystal.

The next emission peak appeared with the highest intensity in the yellow region, peaking at 578 nm due to the transition of $^4F_{9/2} \rightarrow {}^6H_{13/2}$. This transition was reported to be hypersensitive and strongly dependent on the host environment originated by a forced electric dipole [18]. Generally, $^4F_{9/2} \rightarrow {}^6H_{13/2}$ appears dominant when Dy^{3+} -ions are occupied at low-symmetry sites without an inversion center [96]. The dominant nature is reflected by the yellow to blue (Y/B) ratio, which is also regulated by the charge (Z) to radius (r) ratio, Z/r, as well as the electronegativity (E) of the next-neighboring alkali element (Li) [97]. The yellow to blue (Y/B) ratio was calculated to be 2.57

based on the area of each emission peak in each region, confirming the location of Dy^{3+} ions in low symmetry locations without inversion centers. The third emission peak was discovered in the red Vis-color area at 666 nm due to the Dy^{3+} characteristic electronic transition, $^4F_{9/2} \rightarrow {}^6H_{11/2}$. This shift can be identified by a low-intensity peak. However, the emission intensity was lowest at 756 nm, in the infrared region generated by the transition $^4F_{9/2} \rightarrow {}^6F_{11/2} + {}^6H_{9/2}$. Our result fits with prior studies on the phosphor, except for the split peak in the blue region for the $^4F_{9/2} \rightarrow {}^6H_{15/2}$ transition [73]. The emission intensity in the blue and yellow regions increased at low temperatures. The continuous change in the intensity with the temperature of the peak in the yellow region is represented in the inset of Figure 4.2.5, which also displays the maximum emission peak value at 25 K. The excitation and emission spectra were quantified in energy units of cm^{-1} and compared to prior investigations [92,93,97,98]. Figure 4.2.7 shows a sketch of the energy band structure based on the peak positions of the energy waves.

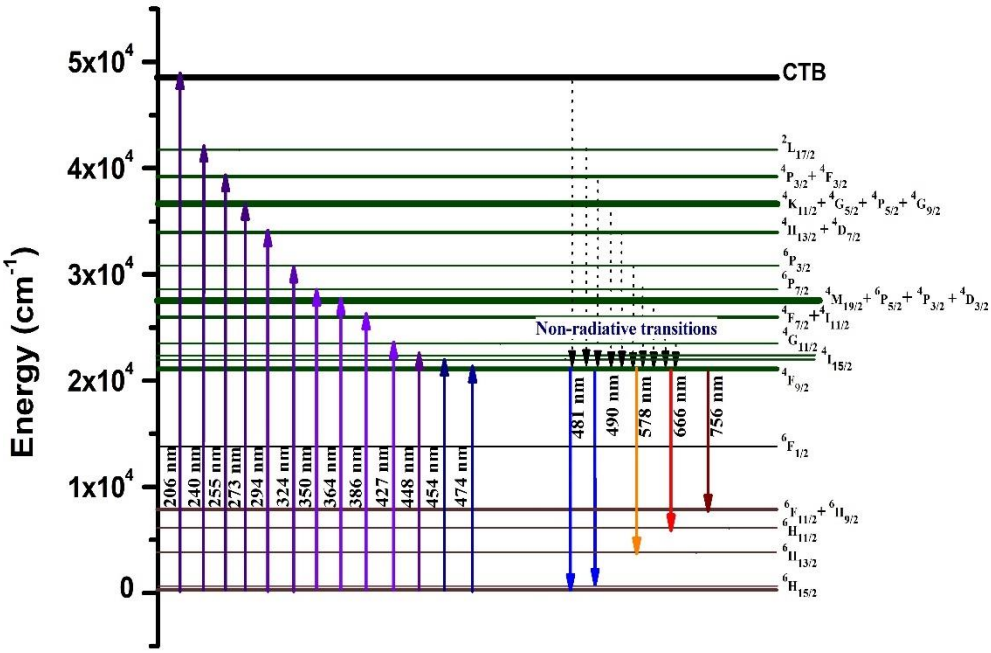

Figure 4.2.7. Observed energy states of Dy^{3+} in the excitation and emission spectrum in LYBO:Dy^{3+} crystal.

4.2.4 Decay Time Measurement

The fluorescence lifetime determined at room temperature for LYBO:Dy^{3+} single-crystal excitation at 350 nm and emission at 578 nm is given in Figure 4.2.8 (a). Using equation (3.4), the observed decay time was fitted with three exponential components. At room temperature, the empirically determined lifetimes are 78 ± 2, 386 ± 16, and 815 ± 11 μs with 18.7, 33.6, and 47.5% contributions under excitation at 350 nm and for emission at 578 nm, respectively.

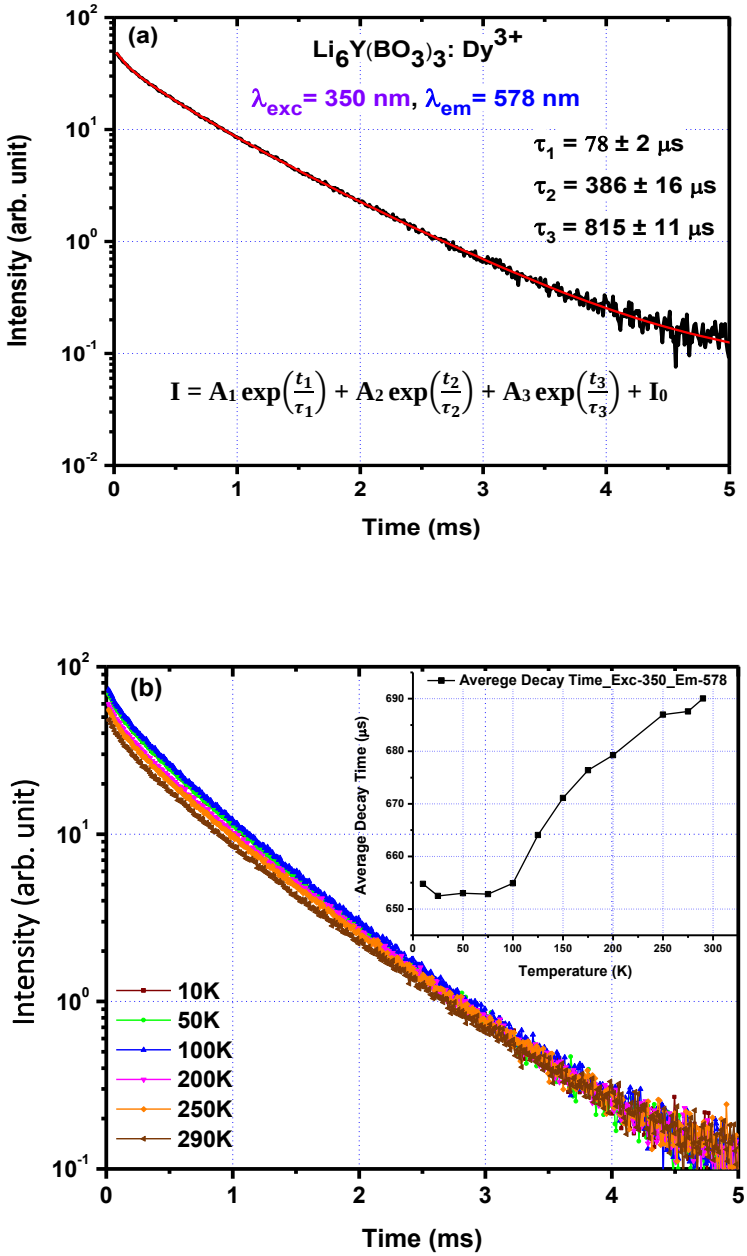

Figure 4.2.8. The fluorescence lifetime curve of the LYBO:Dy^{3+} crystal, excited at 350 nm and emitting at 578 nm (a) at ambient temperature and (b) at low temperatures ranging from 290 to 10 K while the variation in average decay time is presented inset.

At ambient temperature, the average decay time of the three components was determined to be 690 μs using the equation (3.5). The value decreased with increasing temperature from 290 K to 10 K, as seen in the inset of Figure 4.2.8 (b). At a temperature of 10 K, the shortest average lifetime was determined to be 655 μs. The variation in decay time as a function of temperature is shown in detail in Figure 4.2.8 (b). This property can be explained by the stark component and cross-relaxation processes. The decay time variation with temperature follows the previous findings acquired from dysprosium doped crystals with various host materials. [99,100].

4.2.5 Transmittance

Transmission characteristics can provide valuable information regarding the possibility of scintillation performance of the sample. To determine the amount of self-absorption and validate the effectivity of photoluminescence peaks stated in Section 4.2.4, the transmittance spectra of LYBO:Dy^{3+} and reference CMO crystals were produced, as seen in Figure 4.2.9. Both crystals were about 1 centimeter thick for this measurement. The LYBO:Dy^{3+} crystal exhibited about 45 % transparency between 475 and 500 nm (defined by green dotted lines) and approximately 55 % transparency between 560 and 590 nm (marked by blue small-dotted lines). These are the regions where Dy^{3+} characteristic emissions were intense for the sample crystal. On the other hand, the standard CMO crystal has high transparency of around 75 % above 300 nm and is practically flat until the near-infrared range. The transmittance spectra of the LYBO:Dy^{3+} crystal revealed absorptions at 206, 257, 274, 294, 325, 351, 365, 386, 427, 448, 456, and 474 nm. Except for the excitation peak at 241 nm, the absorption locations agree well with prior

photoluminescence data. The absorptions at 750, 801, and 894 nm can be observed due to the transitions from $^6H_{15/2}$ to $^6F_{3/2}$, $^6F_{5/2}$, and $^6F_{7/2}$, respectively.

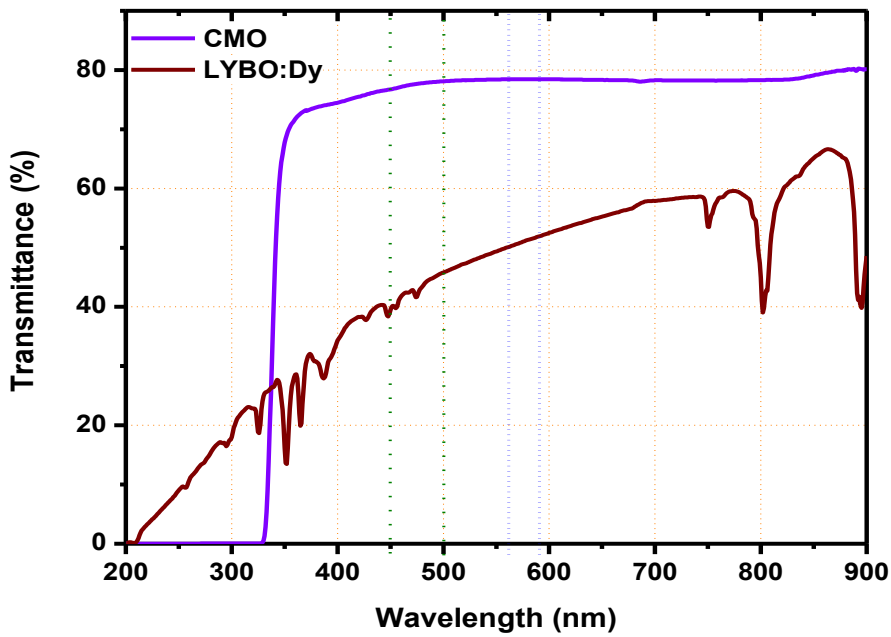

Figure 4.2.9. Transmittance spectra were obtained for the grown LYBO:Dy^{3+} and the reference CMO crystals.

4.2.6 Scintillation Properties Measurement

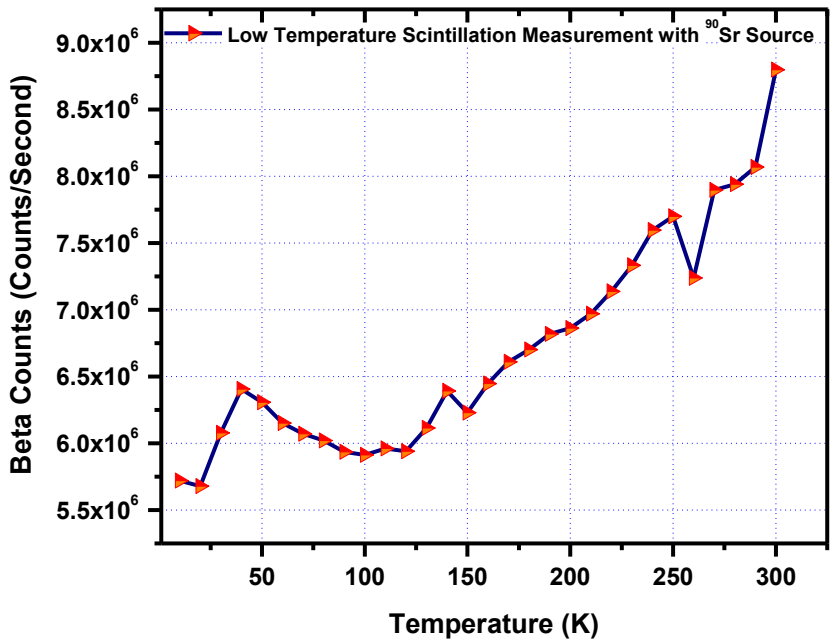

Figure 4.2.10. Variation in the number of single photons counts under β^- excitation from ^{90}Sr source at a temperature ranging from 300 K to 10 K.

As seen in Figure 4.2.10, the single-photon counting approach was used to determine the beta scintillation capabilities of the Dy^{3+} doped LYBO crystal both at room and low temperatures. The numbers decreased as the temperature decreased, as seen by the curve. The most likely explanation for this quenching feature in radioluminescence is the presence of trap-centers between the bandgaps. The emission weighted quantum efficiency ($\overline{\text{EMQE}}$) of the PMT and the associated crystal were determined using the X-ray induced emission spectrum of that crystal sample and the quantum efficiency (QE) curve of the PMT using the equation 2.20 [61,62]:

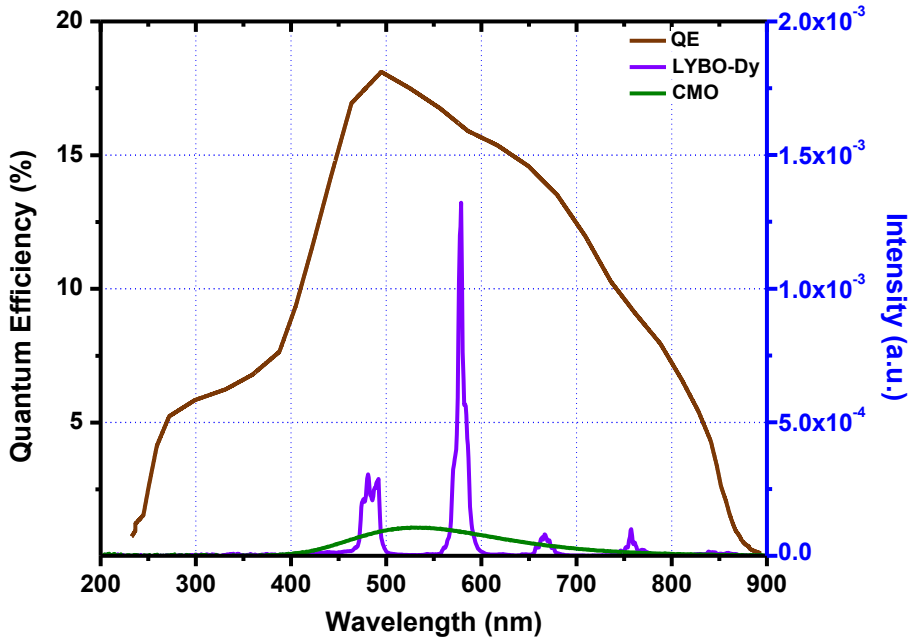

Figure 4.2.11. Comparison of the quantum efficiency (QE) spectrum of R7400U-20 PMT and X-ray induced emission spectrum of CMO and LYBO:Dy^{3+} crystals.

where $QE(\lambda)$ and $E_m(\lambda)$ are the intensity functions at respective wavelengths, determined for the QE curve of the PMT and emission spectra obtained from the crystals. $\overline{EMQE}$ can also be specified as the ratio of the PMT-generated photoelectron (N_{pe}) and the photons numbers created in the crystal (N_{ph}) under the excitation of radiation, as appeared in equations 2.22 and 2.23. In the next step, the comparative light yield of the grown LYBO:Dy^{3+} crystal in comparison to the reference CMO crystal was determined using equation (4.2.1) [101,102] :

$$LY_{LYBO:Dy} = \frac{N_{pe\,(LYBO:Dy)} \times \overline{EMQE}_{CMO}}{N_{pe\,(CMO)} \times \overline{EMQE}_{LYBO:Dy}} LY_{CMO}, \qquad (4.2.1)$$

where $LY_{LYBO:Dy}$ and LY_{CMO} denote the photon yields per MeV. At ambient temperature, the X-ray emission spectra of CMO and LYBO:Dy^{3+} were compared to the quantum efficiency (QE) of the Hamamatsu PMT-R7400U-20, as shown in Figure 4.2.11, to minimize discrimination in the detection of the distinct luminescence centers of different crystal samples. The estimated area of the LYBO:Dy^{3+} X-ray emission spectrum was 92% that of the CMO reference crystal. The results in Table 4.2.1 compare the emission peak values, $\overline{EMQE}$, and scintillation light yields of CMO and LYBO:Dy^{3+} crystals. At ambient temperature, the absolute scintillation light production of LYBO:Dy^{3+} crystal was measured to be 4500 ± 550 Photons/MeV, or 92.8% photon counts in comparison to CMO crystal under β^- irradiation. In brief, the α/β ratio for LYBO:Dy^{3+} was estimated to be around 0.24 using this method, while the value for the reference CMO crystal was 0.20 [86]. The absolute amount is difficult to determine since the ^{90}Sr source has a beta energy distribution spectrum that necessitates spectroscopic examination. The light yield of an LYBO compound doped with 1 mol% Ce^{3+} was previously reported to be 1200 Photons/MeV [19,103]. However, certain inconsistencies in single-photon counting measurement and ambiguity while unfolding the QE curve of the PMT may be considered throughout the experiment. Despite certain discrepancies in the precise measurement of light yields, the LYBO:Dy^{3+} showed promising results.

Table 4.2.1. Emission peaks, emission weighted quantum efficiency, and beta scintillation light yield comparison of CMO and LYBO:Dy^{3+} crystals

Crystal	λ_{em} (nm)	$\overline{EMQE}$	Relative Scintillation Light Yield (%)	
			^{90}Sr	^{241}Am
CMO	540	15.66	100 [86]	20
LYBO:Dy^{3+}	481, 578	15.85	92.8	24

4.2.7 Thermally Stimulated Luminescence Studies

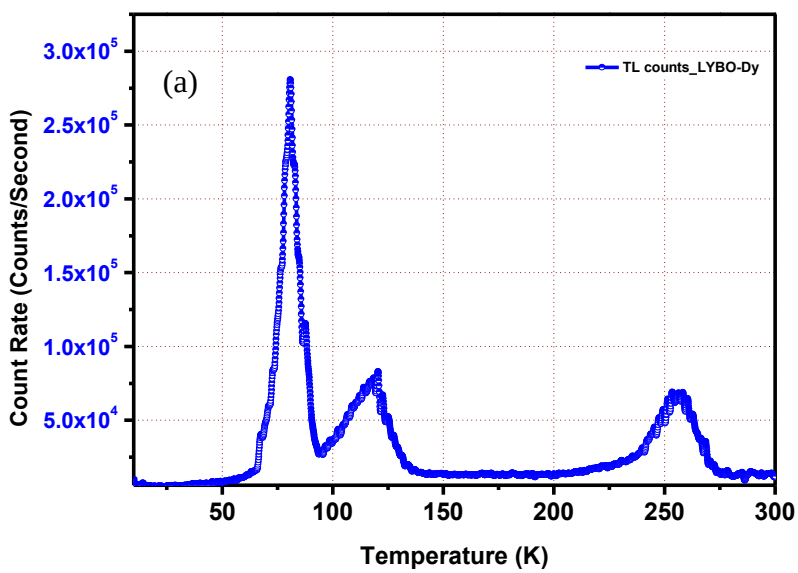

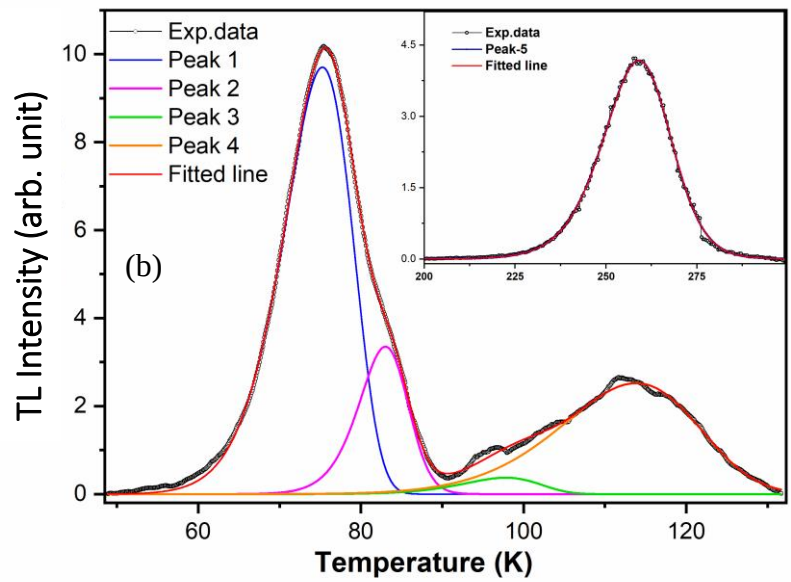

Figure 4.2.12. (a) The measured TSL glow curve of Dy^{3+} doped LYBO samples after X-ray irradiation (b) TSL Glow curve deconvolution for Dy^{3+} sample.

Luminescence and scintillation performances can be affected by the trapped (localized) electrons and holes as a result of energy absorption from external UV or radiation sources. Under thermal stimulation, the delocalization of these electrons and holes can result in luminescence, which can be used to determine the trap levels inside the material. The thermally stimulated luminescence (TSL) technique is a useful tool for studying the de-trapping and relaxation processes of luminous materials. TSL glow curve of Dy^{3+} doped single crystals were measured after X-ray irradiation at 10 K for 30 minutes. Figure 4.2.12 (a) shows the recorded TSL curve in the temperature range of 10 − 300 K with a linear heating rate of 0.1 K/s of the Dy^{3+} doped

LYBO single crystal. At 75, 83, 98, 113, and 259 K, the recorded glow peaks reveal the presence of five trap centers. TSL kinetic parameters such as trap depth (E) and frequency factor (s) were computed using an analytical expression presented in equation (4.2.2), which Kitis et al. [104] recommended for general order kinetics.

$$I\,(T) = I_m b^{\left(\frac{b}{b-1}\right)} e^{\left(\frac{E}{k.T}\frac{T-T_m}{T_m}\right)} \left[(b-1)(1-\Delta)\frac{T^2}{T_m^2} \times e^{\left(\frac{E}{k.T}\frac{T-T_m}{T_m}\right)} + Z_m\right]^{\frac{-b}{b-1}}, \tag{4.2.2}$$

where $\Delta = \frac{2kT}{E}$, $\Delta_m = \frac{2kT_m}{E}$, and $Z_m = 1 + (b-1)\Delta_m$

The curve fittings are done using the Microsoft Excel spreadsheet program, with the solver utility [105].The fitting quality has been monitored using the figure of merit (FOM) given in equation (7).

$$FOM = \frac{\sum_P |TL_{exp} - TL_{fit}|}{\sum_P TL_{fit}}, \tag{4.2.3}$$

where TL_{exp} and TL_{fit} are the experimentally measured and fitting function intensities, respectively. The FOM value of the fitting is 3.8, indicating that it fits well. Figure 4.2.12 (b) depicts the deconvoluted TSL glow curves, and Table 4.2.2 lists the derived values. Peak 2 has high E and s values attributable to its narrower form than the prior peak. It is likely because two first-order peaks arise at the same temperature area with different activation energies, resulting in one peak with greater energy and smaller width. Localization of excited electrons and holes, which serve as luminescence centers, is typically

required for luminescence materials. These electrons and holes that have been stimulated are impacted by the trap centers, which can capture electrons and holes. It was discovered that the TL light peaks of doped crystal are identical to those of pure crystal, confirming that the host material is the source of the trap. I.N. Ogorodnikov et al. [106] observed and adequately explained comparable results for $Li_6Gd(BO_3)_3$ doped with Ce^{3+} ions. X-ray irradiation at low temperature leads to the creation of several forms of the electron and hole trapping centers, according to extensive research on the lattice defects of lithium borates in LYBO crystal. In order to compensate for the extra electric charge of heterovalent impurities or a few structural lattice defects, lithium vacancies can occur not only after irradiation, but also during crystal formation. In samples doped with Dy^{3+}, however, a shoulder peak was found at 83 K (#Peak 2). The intensity of the Dy^{3+} -doped sample is about three times that of the pure sample. Due to the mismatch in ionic radius size, substituting 4 mol% Dy^{3+} for yttrium ions may shift the concentration of point defects. Due to the presence of these identified trap centers, the light production drops in locations with low temperatures (under β^- stimulation; see Figure 4.2.10).

Table 4.2.2. Calculated TSL kinetic parameters: activation energy (E), frequency factor (s), order of kinetics (b), and T_{max}.

Peaks	T max (K)	Order of kinetics (b)	Activation energy (E, meV)	Frequency factor (s, s^{-1})
Peak -1	75	1	110	5.67×10^{05}
Peak -2	83	1.2	218	6.31×10^{11}
Peak -3	98	1	166	7.51×10^{06}
Peak -4	113	1	127	5.06×10^{03}
Peak -5	259	1.4	740	3.10×10^{12}

4.2.8 Imaging with Thermal Neutron

To assess the performance of the sample crystal as a thermal neutron scintillator for imaging, it was put in the position of a scintillation screen in a standard digital neutron imaging facility. Figure 4.2.13 shows the corrected picture of the crystal as a consequence of photons following thermal neutron absorption throughout a 300 s exposure with a 0.1 ms pulse rate. The picture, however, seemed to be too noisy to define and compare to other standards when sensitivity or modulation transfer functions were measured. [107,108]. The average gray value ratio between the crystal and the surroundings is just 1.2, which must be increased significantly before the crystal can be utilized for thermal neutron imaging. However, as a preliminary discovery, the crystal has been shown to act as a thermal neutron scintillation imaging screen. A CCD camera with a greater QE value in the emission zone of the crystal along

with enhanced quality crystal and its optimized thickness can be applied to resolve the issue.

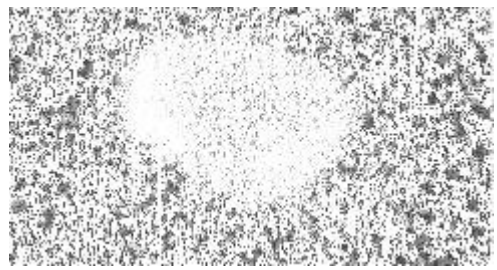

Figure 4.2.13. Thermal neutron-induced image while LYBO:Dy^{3+} crystal was used as the scintillating screen, captured by a CCD at 300 s exposure with a 0.1 ms pulse.

4.3 Luminescence and Scintillation Properties of Czochralski Grown Pr^{3+} Doped $Li_6Y(BO_3)_3$ Single Crystal

4.3.1 Structure Analysis

The Rietveld refinement method investigated the powder XRD pattern of the Pr^{3+} activated LYBO single crystal [78]. The experimental data were analyzed here to a reference ($\mathrm{Ref.}\,98-006-8653$) from the International Center for Diffraction Data, which has a Figure of merit of 2.01, as shown in Figure 4.3.1 [91]. Crystallization of the doped LYBO compound revealed a monoclinic structure with the space group $P2_1/c$. The unit cell has a volume of 755.913 $Å^3$ and a density of 2.69 $g \cdot cm^{-3}$, with lattice parameters a = 7.184, b = 16.43, c = 6.64, and β = 105.30°. The parameters correlate well with the reference because the difference between experimental and computed data is visually represented in the residue section [25]. A little increase in cell volume relative to previous reports of pure crystals may explain the integration of praseodymium atoms in the unit cell in place of yttrium, which has smaller atomic radii [109].

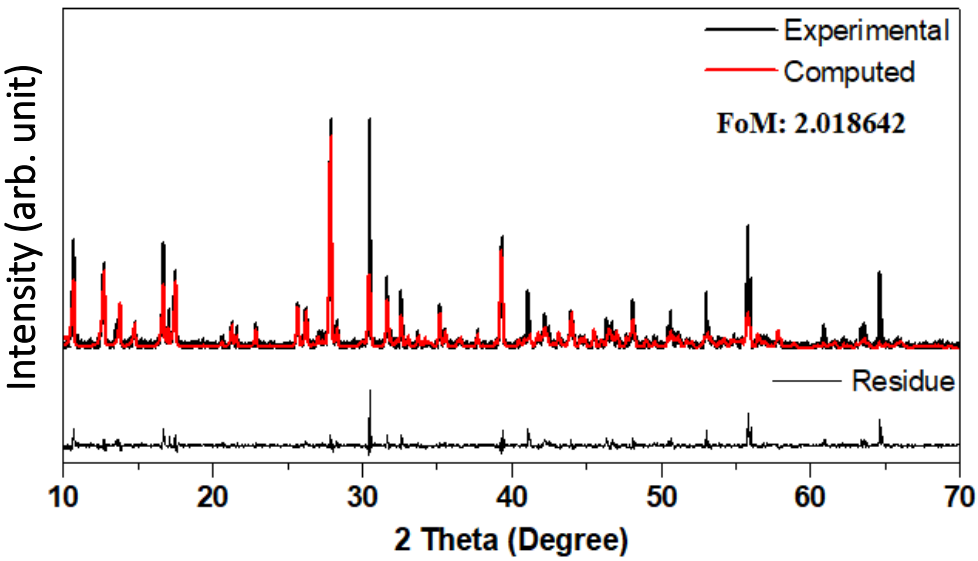

Figure 4.3.1. Rietveld refined spectra of Czochralski grown Pr^{3+} doped LYBO single-crystal plotted with experimental (black) and computed (red) data while residual data plot at the bottom.

4.3.2 Luminescence Properties

The optimum concentration of 1 mol% doping was determined by analyzing the integrated X-ray-induced luminescence spectral area, obtained using polycrystalline powders of LYBO, while the doping concentrations of Pr^{3+} ions ranged from 0.5 to 3 mol%. Figure 4.3.2 demonstrates the X-ray-induced luminescence of an optically polished 7 mm × 7 mm × 7 mm sized sample of 1 mol% Pr^{3+} doped LYBO single-crystal. For all doped phosphors and produced crystals, a low-intensity signal between 300 and 375 nm was recorded, which might be identified as the combined response of intrinsic and dopant luminescence [11,110]. The exposition is comprehensive, including emission spectra of a single crystal of pure and Pr^{3+} doped material (Figure 4.3.2). The spectrum of the pure LYBO crystal in the red line (Figure 4.3.2)

had a peak at 327 nm, whereas the spectrum of the doped crystal in the black line (Figure 4.3.2) peaked at 307 and 327 nm. Meanwhile, the dominant emission occurred between 400 and 550 nm, with peaks at 438 and 456 nm. At 603, 618, and 638 nm, respectively, intraconfigurational emission peaks owing to $^1I_6/^3P_1 \rightarrow ^3H_6$, $^3P_0 \rightarrow ^3H_6$, $^3P_0 \rightarrow ^3F_2$ transitions were detected [93].

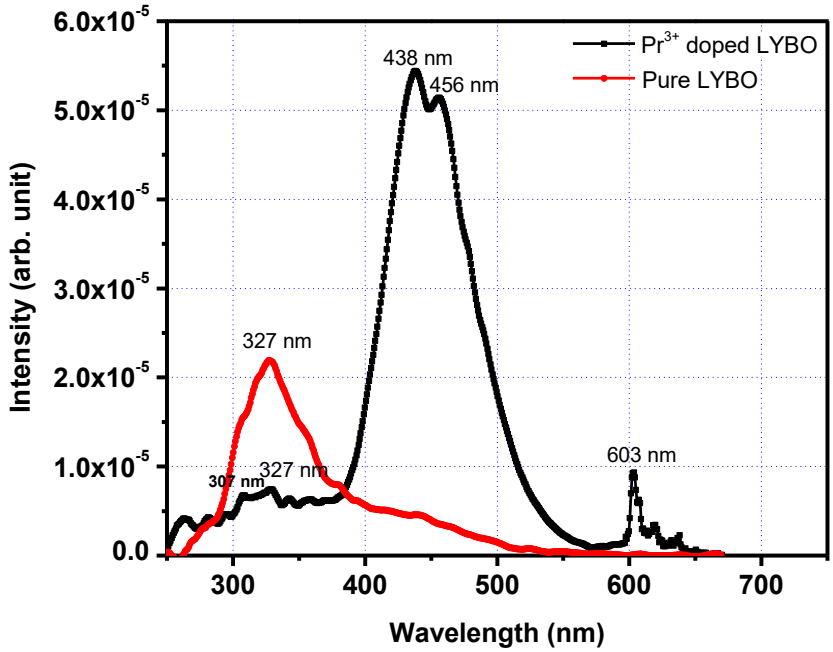

Figure 4.3.2. X-ray induced luminescence of Pr^{3+} doped LYBO crystal (black) and Pure LYBO crystal (red).

Figure 4.3.3 shows excitation spectra for the emission peaks at 309 (blue), 421 (black), and 603 (red) nm as a function of the PL excitation wavelength. The excitation peaks for 309 nm emission were found to be 205, 227, and 249 nm in wavelength, whereas 603 nm emission had 447, 473, and 484 nm additional excitation positions due to the $4f^2$-$4f^2$ transition from $^3H_6$ to $^3P_2$, $^1I_6/^3P_1$, and $^3P_0$ energy levels, respectively. The excitation for the

emission peak at 421 nm was achieved at 257 nm, showing that the luminescence center was located at a different wavelength.

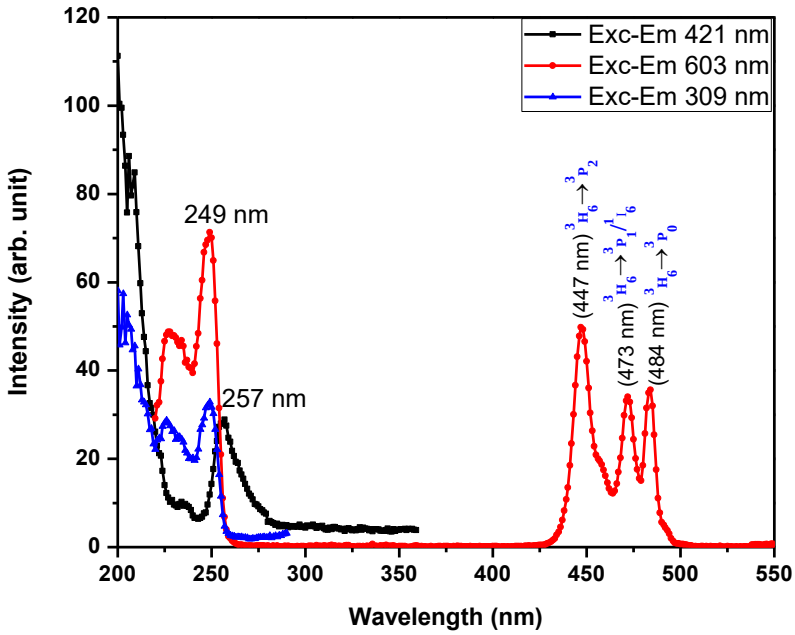

Figure 4.3.3. The photoluminescence excitation spectra were measured for the emission peaks at 421 nm (black), 603 nm (red), and 309 nm (blue).

The PL emission peaks were identified at 309, 421, 485, 588, 603, 618, 638, and 710 nm from the spectra in Figure 4.3.4 under excitation with UV-Vis wavelengths at 205 nm (green), 227 nm (black), 250 nm (purple), 256 nm (cyan), and 447 nm (orange). The emission spectrum in blue (Figure 4.3.4) was obtained using a 266 nm pulsed laser source, indicating a peak at 327 nm, corresponding to intrinsic emission. The peak at 421 nm matched other spectra obtained using various PL excitations. The intensity ratios of the emission peak sites fluctuated with various PL excitations, as illustrated in the contour map in Figure 4.3.5.

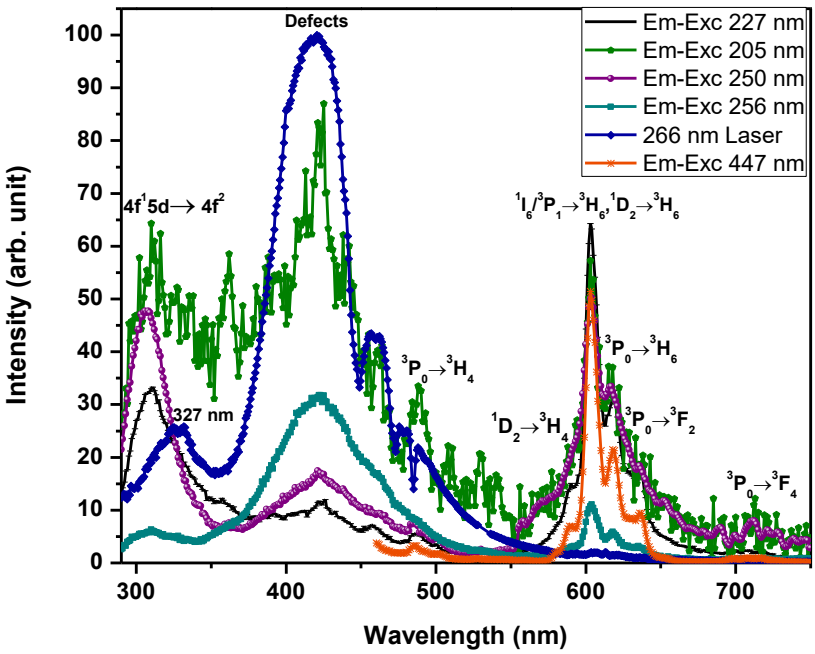

Figure 4.3.4. Photoluminescence emission for different excitations 205 nm (green), 227 nm (black), 250 nm (purple), 256 nm (cyan), 447 nm (orange) and 266 nm laser excitation source (blue).

According to Yiyi Ou et al.'s research, on the vacuum referred binding energy (VRBE) curve for LYBO, the emission peak at 309 nm might be attributed to the $4f^15d$-$4f^2$ transition [25]. Compared to other borates such as LaB_3O_6 and $LaMgB_5O_{10}$, LYBO has a greater Stokes shift, allowing the lowest level of the 5d band to be relaxed farther and reached below the $^1S_0$ level of the 4f state [26,111–113]. However, the emission in the 400∼500 nm range seen in Figures 4.3.2, 4.3.4, and 4.3.5 corresponds to a different luminescence center than the PL excitation peaks in Figure 4.3.3. The black curve in Figure 4.3.3 has a lower intensity peak at 227 nm, but the prominent peak location has been relocated to 257 nm. It indicates that charge carriers

were transferred from the 4f–5d excitation area to defect centers. In their work, S. A. Kiselev and his team found an almost identical event that was explained using Dieke's energy level diagram, but the PL and XRL peak locations were different than in our work [49,110]. The emission peaks, however, may correspond to previously reported emissions from Ce^{3+} doped LYBO crystals, which showed peaks at 390 and 410 nm [17,19,26,114]. ICP-OES analysis was done to validate the absence of Ce^{3+} -ions in 1 mol% Pr^{3+} doped LYBO phosphor and crystal samples by comparing them with a separately synthesized 0.2 mol% Ce^{3+} doped LYBO phosphor sample, as shown in Table 4.3.1. Within the instrument's detection limit (≥ 60 ppm (mg/kg)), there was no evidence of Ce^{3+} -ions in the Pr^{3+} -ion doped samples.

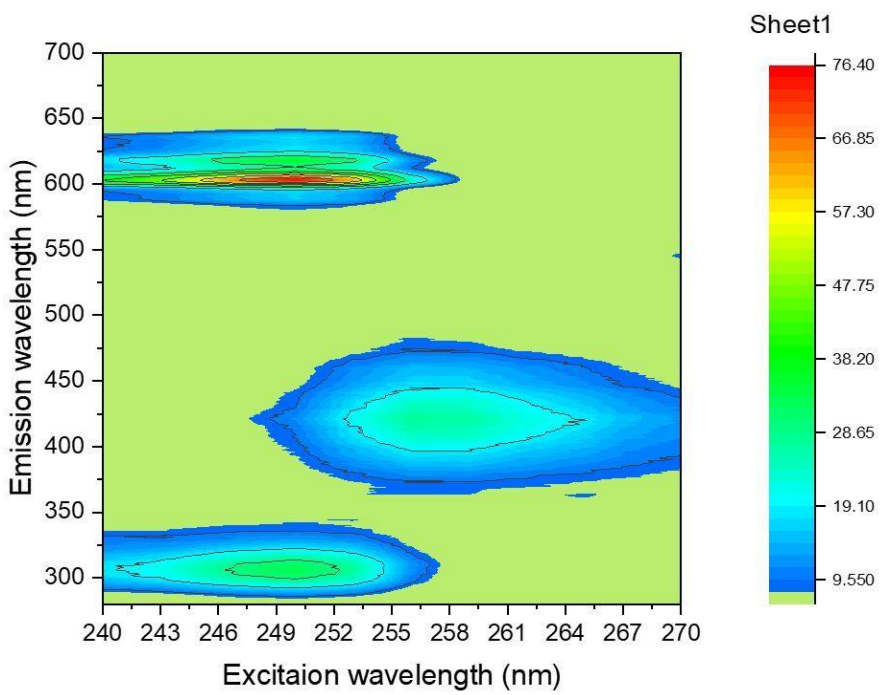

Figure 4.3.5. The contour plot is shows the change in PL emission wavelengths on the Y-axis with the change of PL excitation wavelengths on the X-axis at room temperature.

Meanwhile, the emission peak sites associated with the $4f^2$-$4f^2$ transitions were detected in Figure 4.3.4 at 485, 588, 603, 618, 638, and 710 nm, respectively, corresponding to $^3P_0 \rightarrow {}^3H_4$, $^1D_2 \rightarrow {}^3H_4$, $^1I_6/{}^3P_1 \rightarrow {}^3H_6$ or $^1D_2 \rightarrow {}^3H_4$, $^3P_0 \rightarrow {}^3H_6$, $^3P_0 \rightarrow {}^3F_2$, and $^3P_0 \rightarrow {}^3F_4$ electronic energy band transitions.

Table 4.3.1. The measured amount of Cerium and Praseodymium in the 1 mol% Pr^{3+} doped LYBO phosphor and crystal samples in comparison with 0.2 mol% Ce^{3+} doped LYBO phosphor sample using inductively coupled plasma optical emission spectrometer (ICP-OES) technique.

Sample	Measurements	Ce in ppm (mg/kg)	Standard Deviation (S.D.)	Pr in ppm (mg/kg)	Standard Deviation (S.D.)
1 mol% Pr^{3+} doped LYBO Phosphor	1st	N.D*	0.48 %	2970.94	0.40 %
	2nd	N.D*	0.80 %	3016.91	0.55 %
1 mol% Pr^{3+} doped LYBO crystal	1st	N.D*	3.97 %	879.81	0.57 %
	2nd	N.D*	2.68 %	903.01	1.05 %
0.2 mol% Ce^{3+} doped LYBO Phosphor	1st	561.65	0.98 %	64.07	0.71 %
	2nd	552.62	0.63 %	64.08	0.87 %

* ND= Not Detected, refers to the content below 60 ppm.

4.3.3 Optical Properties

The optical absorption spectrum of the Pr^{3+} -doped sample crystal was determined in the UV–Vis-NIR region ranges between 250 and 2000 nm, as displayed with normalized units in Figure 4.3.6. Several absorption peaks were identified at 447, 473, 484, 603, 1015, 1494, 1547, and 1864 nm, which correspond to energy transitions from the ground state $^3H_4$ to the higher energy states of $^3P_2$, $^3P_1/^1I_6$, $^3P_0$, $^1D_2$, $^1G_4$, $^3F_4$, $^3F_3$, and $^3F_2$, respectively [93]. Four absorption peaks were found in the near-infrared (NIR) region at the wavelength of 1015, 1493, 1543, and 1864 nm. However, above 1900 nm, any absorption peak was not detected that could identify the energy transition, $^3H_4 \rightarrow ^3H_6$.

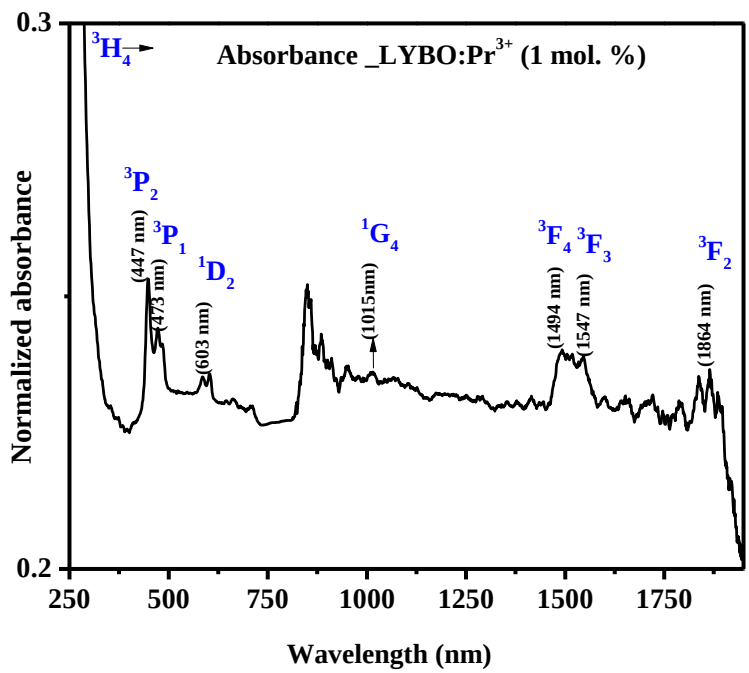

Figure 4.3.6. The normalized absorbance spectrum measured for the LYBO:Pr^{3+} crystal ranged from 250-2000 nm.

As shown in Figure 4.3.7, the transmittance spectrum for the Pr^{3+} ion-doped LYBO crystal sample with a shape of 3 mm × 9 mm × 7 mm at room temperature was obtained. The transparency was more than 50% in the area between 300 and 900 nm, confirming the crystal's adequate optical quality for scintillation experiments. At wavelengths below 245 nm, the transmittance value was zero owing to dopant absorption inside the crystal. Other absorptions at 266, 448, 473, and 484 nm were also observed in the PL excitation spectra (Fig. 4.3.3) and absorption spectra (Fig. 4.3.6).

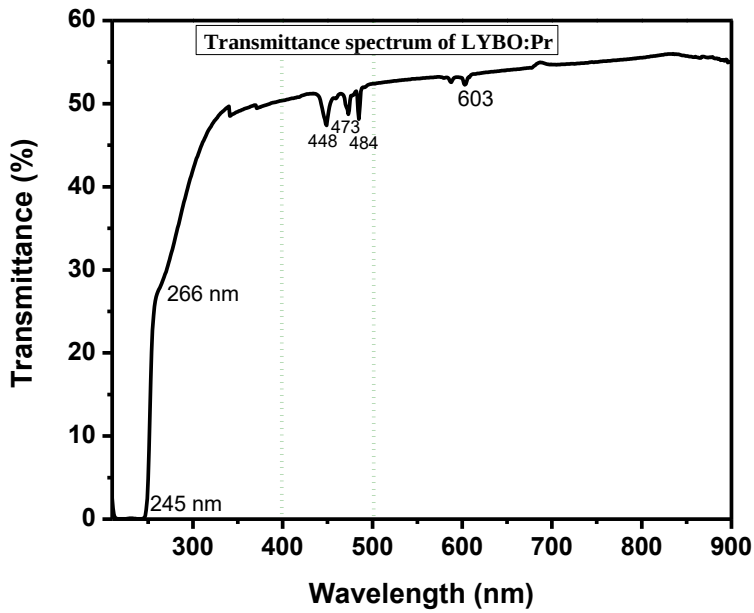

Figure 4.3.7. The transmittance spectra were measured for the 3 mm thick LYBO:Pr^{3+} crystal from 200 to 900 nm.

4.3.4 Commission International De I'Eclairage (CIE) Chromaticity

The combined emission colors for the Pr^{3+} ion-doped LYBO crystal under PL excitations at 205, 227, 249, 256, 266, and 447 nm were obtained

using Commission International De I'Eclairage (CIE) 1931 chromaticity coordinates, as shown in Figure 4.3.8. As the intensities of emission peaks at distinct wavelength regions altered under different excitation wavelengths, the CIE color coordinates were also varied. The identified emission colors are blue for 266 nm, magenta for 256 nm, light pink for 205 nm, light orange for 227 and 250 nm, and orange-red for 447 nm excitations, respectively, which might be distinguished in visual color range.

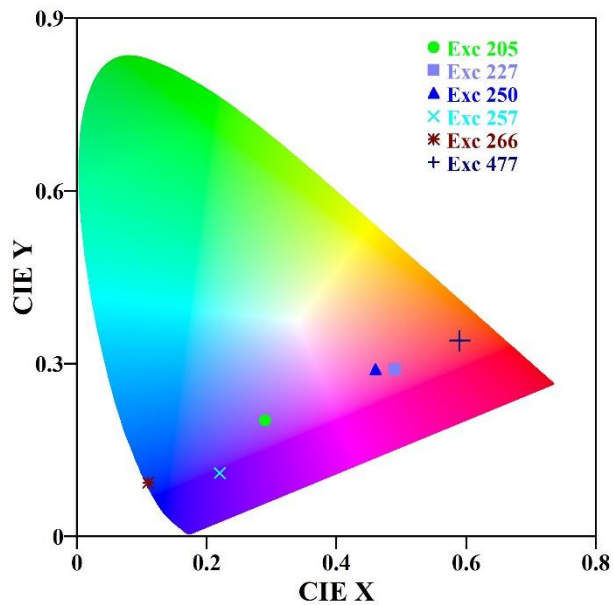

Figure 4.3.8. CIE 1931 chromaticity diagram shows the combined emission color for six different photo-excitations for the LYBO:Pr^{3+} crystal.

4.3.5 Scintillation Decay Time

The estimated photon lifetimes emitted from the sample crystal are displayed in Figure 4.3.9 (a) under α-particle excitation from a ^{241}Am source after extracting the incident γ-ray from PMT noise (see section 4.3.6). Three-

components exponential decay functions (equation 3.4) were used to fit the obtained lifetime curve, while $\frac{\chi^2}{ndf}$ value was $\frac{645}{794}$ (ndf = number of degrees of freedom). The estimated components τ_1, τ_2, and τ_3 are 15.2 ns, 219.2 ns, and 1.74 μs with a contribution of 37, 8, and 55%, respectively. The shortest component, τ_1, was generated from the $4f^15d$-$4f^2$ transition belonging to Pr^{3+} ions [115]. The slower components τ_2 and τ_3 correspond to the forbidden $4f^2$-$4f^2$ transitions that were responsible for the orange-red glow in the spectrum [62]. The decay time curve obtained under γ-ray excitation from ^{60}Co is shown in Figure 4.3.9 (b). Three-component exponential decay-time functions (equation 3.4) were used to fit the curve with $\frac{\chi^2}{ndf}$ value $\frac{1722}{994}$. The observed decay components τ_1, τ_2, and τ_3 are 14.3 ns, 255.4 ns, and 2.64 μs, respectively, with contributions of 59.1, 3.5, and 37.4%. Individual contributions of interconfigurational and intraconfigurational transitions are represented by these three components alike under α-particle excitation. The contrast between the signals from γ-rays and α-particles represents the feasibility of using the crystal sample for thermal neutron detection.

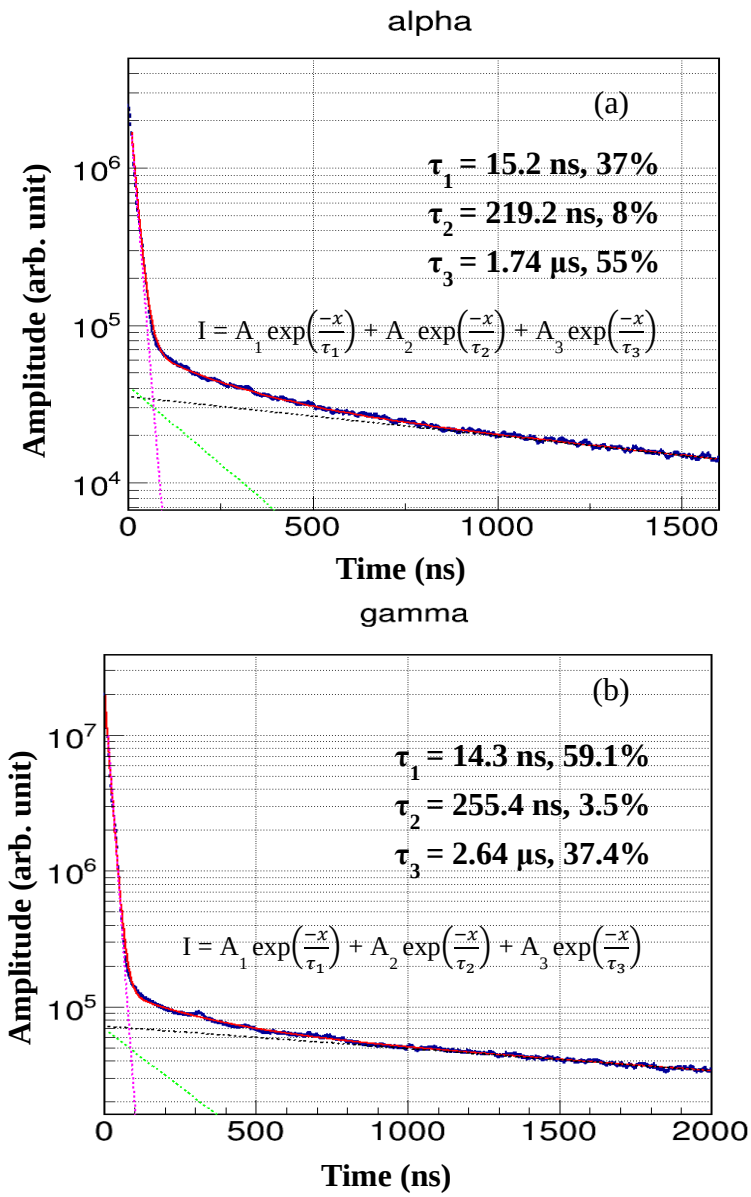

Figure 4.3.9. Decay time projection (a) under alpha excitation from ^{241}Am radioactive source after separation with PSD ratio where τ_1 is due to $4f^1,5d$ - $4f^2$ transition, τ_2 and τ_3 for 4f-4f intraconfigurational transition. (b) Under γ-ray excitation with ^{60}Co source, which separately shows three components of interconfigurational and intraconfigurational transitions.

4.3.6 Pulse Shape Discrimination study

The charge integration method was used to determine the PSD ability of the Pr^{3+} -ion doped LYBO crystal for α-particles, γ-rays, and thermal neutrons from ^{241}Am, ^{60}Co, and ^{252}Cf radioactive sources, respectively. With the varied PSD ratios (equation 2.24) shown in Figure 4.3.10 (a), the α-particles and γ-rays responses from ^{241}Am and ^{60}Co sources were distinguished with a high degree of separation from PMT noise. Event detection in the bottom half of the PSD matrix (Figure 4.3.10 (a)) was due to interactions between α-particles on the surface of the crystal sample. The overall charge amount of these events was less varying than that of the γ-ray responses in the center of the PSD matrix. Figure 4.3.10 (b) shows the pulse height spectrum obtained under α-particles excitation, revealing a distinct peak with a 37.7 % energy resolution when fitted well with the Gaussian function. The sample crystal had a low scintillation light yield that might contribute to the peak broadening. A fairly small distance (~0.5 mm) between the crystal and the source may impact the incident energy of α-particles, resulting in a smaller energy charge contribution.

The detection capacity of the grown crystal sample for thermal neutrons was determined using a weak ^{252}Cf source. The spontaneous fission neutrons and γ-ray responses are shown in Figure 4.3.10 (c), accompanied by high PMT noise due to the extended data acquisition period. Thermal neutrons were detected via charge particle products formed by neutron interactions with the detector volume, as shown by the indicated region in the lower part of the PSD matrix. The alpha energies of ^{6}Li and ^{10}B thermal neutron-driven nuclear events are roughly 2.05 and 1.47 MeV, respectively, with Q-values of 4.78 and 2.79 (2.31) MeV, consecutively [30]. When the quenching factor (α/β ratio) is considered, the variation in the energies of the daughter alpha particles

from ^{6}Li and ^{10}B is hard to distinguish since the luminescence output of the sample was relatively low [116]. The interactions with the spontaneous fission γ-rays from the source are shown in the marked area in the center of Figure 4.3.10 (c). The top region was the consequence of dominating ambient PMT responses in comparison to other forms of radiation. The dominance of PMT response over the crystal response also reflects a moderately low light output. Due to the limited trigger ability of low scintillation light production, only the PMT noise could be recorded. Discriminating between PMT noise and radioactive sources is projected to be more effective using the coincidence approach, which is currently under development. However, the non-hygroscopic characteristics of the grown crystal sample, along with its low atomic number, and density, make it significantly more promising for detecting thermal neutrons and distinguishing ambient γ-ray radiation than previously reported Li-based scintillating crystals.

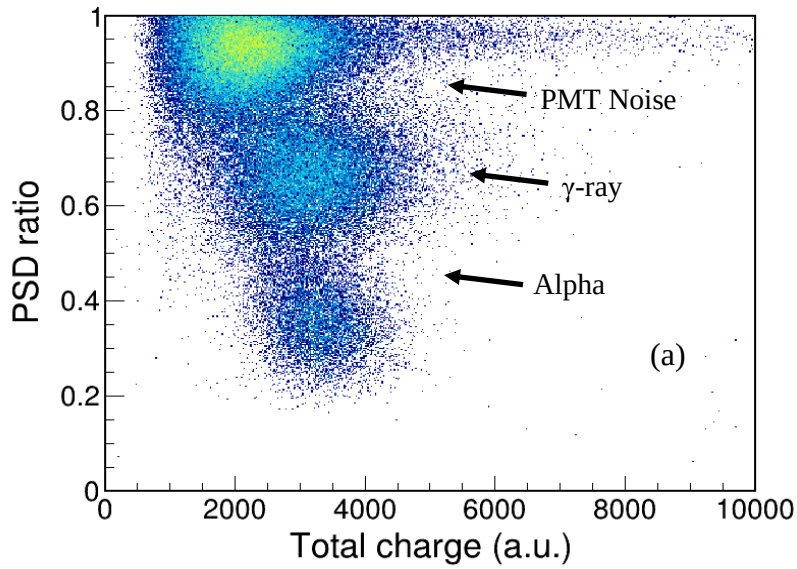
PSD ratio
Total charge (a.u.)
PMT Noise
γ-ray
Alpha
(a)

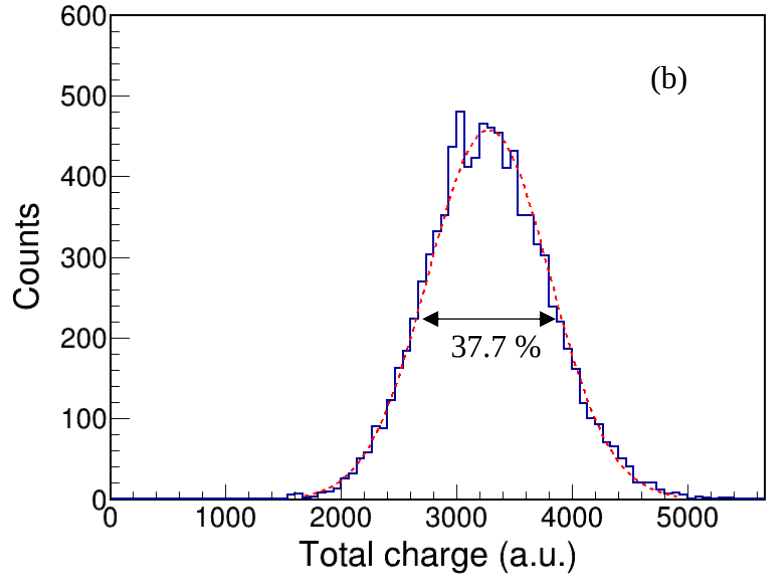
Counts
Total charge (a.u.)
(b)
37.7 %

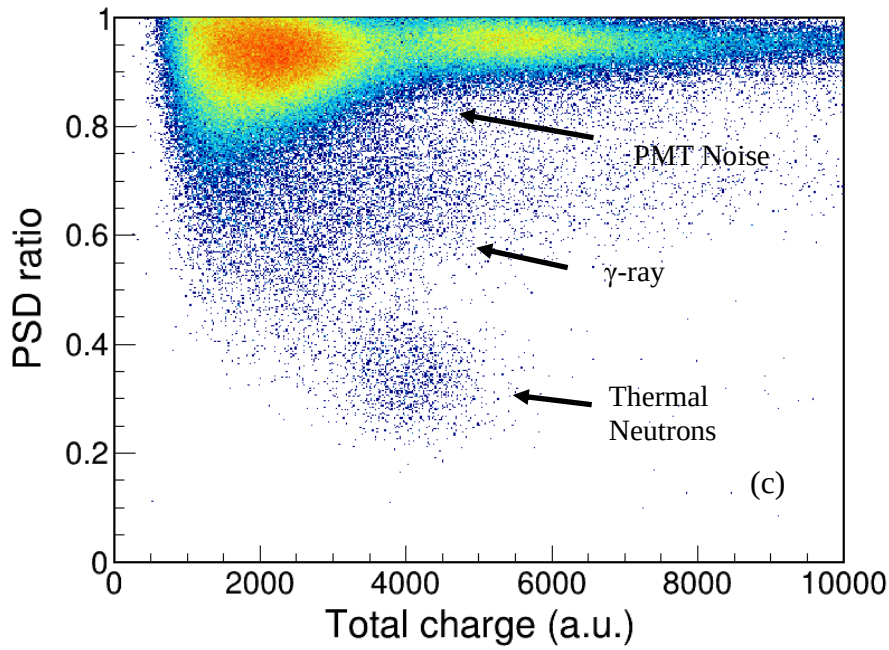

Figure 4.3.10. Pulsed shape analysis with the LYBO:Pr^{3+} crystal. (a) The α-particle response is observed at the lower PSD ratio from 0.20 to 0.45, originating from the ^{241}Am source, γ-ray response from the ^{60}Co source in the middle, and PMT response at the top. (b) A pulse height spectrum under α-particle excitation from ^{241}Am source that was completely separated from the background and the plotted α -peak has FWHM of 37.7 %. (c) Pulse shape discrimination ratio is plotted for the sample crystal under excitation of ^{252}Cf radioactive source. The detected responses from moderated thermal neutron-induced alpha can be identified at the lower part of the PSD ratio from 0.20 to 0.45.

Chapter 5. Summary and Conclusions

To find a suitable compound that can discriminate thermal neutron from γ-rays, three different glass compositions containing high concentrations of thermal neutron-sensitive elements were studied. It was a successful approach to fabricating those borate and silico-borate glasses using the conventional melt-quenching technique, named BLiGd:xEu, BSiGdCaO:xEu, and BLiY:xEu. A highly luminescent sample from each composition was identified by studying X-ray-induced emission characteristics. The identified samples are BLiGd:0.5Eu, BSiGdCaO:0.45Eu, and BLiY:1.5Eu, while BSiGdCaO:0.45Eu showed the highest intensity of emission among all. Beam purity evaluation was performed by applying the conventional beam purity indicator (BPI). Following the ASTM standard procedures, the thermal neutron content was 58.3 % associated with 1.98 % γ-rays. The existing scintillation screen was evaluated based on its luminescent ability due to the absorption of thermal neutrons. The emitted photons passing through the printed pattern in a semi-transparent sheet were detected by the CCD camera and visualized after required software corrections. The phantom lines emerged in the output picture, as well as a low discrepancy to the background. The SNR was evaluated as very low to perform further characterization. Glass samples were used as the scintillation screen in these conditions, and their performances were evaluated using the response of CCD sensors as well as film. The samples could not emit a sufficient number of photons to surpass the existing scintillation screen in the digital imaging technique with CCD. However, the performance was enough to record a significant response on the radiographic film. Over the irradiation duration of 5 min and 10 min, BLiGd:0.5Eu and BSiGdCaO:0.45Eu were found to emit sufficient photons

but could not discriminate the γ-rays. On the other hand, BLiY:1.5Eu produced a smaller number of photons but successfully discriminated thermal neutrons, resulting in an image of the sample ball pen refill on the film. The recognition was critical in identifying the crystalline compound, $Li_6Y(BO_3)_3$, to be grown by the Czochralski method in the following step.

After sintering the powder in the solid-state reaction process, pure and 4 mol% Dy^{3+} doped LYBO single crystals were successfully grown using the Czochralski technique. Pure crystals showed an intrinsic band emission peaking at 330 nm with very low intensity, whereas the crystal doped with Dy^{3+} -ions gave Dy^{3+} characteristic emission under X-ray excitation. Both photoluminescence and X-ray-induced emission revealed a split peak at 484 and 490 nm for the transition from $^4F_{9/2}$ to $^6H_{15/2}$. These peaks exhibit polarization, as shown by their intensity fluctuations in different structural orientations. The highest intensity emission peak was obtained at 578 nm (yellow region). The yellow to blue (Y/B) peak intensity ratio was obtained to be 2.37. The fastest decay component at 10 K was determined to be 77 μs. Scintillation light yield was determined to be 4500 ± 550 Photons/MeV in comparison to the reference CMO crystal under β^- particle excitation from ^{90}Sr source. The α/β ratio was calculated to be 0.24. Though additional quality-control experiments for thermal neutron scintillation application revealed an expected outcome, further research can be performed using a better-quality crystal sample accompanied by a suitable CCD camera. Because the LYBO:Dy^{3+} crystal exhibits excellent luminescence and scintillation capabilities, more studies on imaging applications are possible to be conducted.

To study the real-time detection ability of LYBO crystal, 1 mol% Pr^{3+} -ion was doped as the optimized concentration. The doped crystal sample was grown successfully by the Czochralski method and characterized. The grown crystal showed emission at 309 nm corresponding to the $4f^15d$-$4f^2$ transition along with other $4f^2$-$4f^2$ transition luminescence at 485, 588, 603, 638, and 710 nm. However, a broad emission was observed from 400 to 550 nm, originating from the growth defect. The varied luminescence intensity under different excitation wavelengths caused various emission colors in the CIE chromaticity diagram. Due to the $4f^15d$-$4f^2$ transition, the fastest decay component was found to be 15.2 and 14.3 ns under α-particles and γ-ray excitations. The alpha scintillation finding was persuasive enough to suggest that slow neutrons can be easily distinguished from ambient γ-rays. With a weak ^{252}Cf source, successful thermal neutron and fission γ-ray discrimination was also achieved. The crystal may be grown even further to achieve a defect-free luminescence that can be used to detect thermal neutrons in a γ-ray environment.

References

[1] C.L. Wang, Gd-containing scintillators for thermal neutron detection via graph-based particle discrimination, Rev. Sci. Instrum. 92 (2021) 103304. https://doi.org/10.1063/5.0061426.

[2] R. Barman, S. Saha, M.S. Hossain, A. Das, M.K.A. Rabby, A. Al Mahmud, D. Chowdhury, Study of Structural Characteristics of Ancient Bricks With Neutron Radiography Facility At Btrr, Image Anal. Stereol. 40 (2021) 141-159. https://doi.org/10.5566/IAS.2593.

[3] E. Lehmann, D. Mannes, A. Kaestner, C. Grünzweig, Recent Applications of Neutron Imaging Methods, Phys. Procedia. 88 (2017) 5-12. https://doi.org/10.1016/j.phpro.2017.06.055.

[4] M.K. Alam, S. Islam, S. Saha, M.N. Islam, M.A. Khan, J.M.M. Islam, S.M. Azharul Islam, Characterization of single layer wound healing dressing by using different techniques, African Rev. Phys. 9 (2014) 95-102.

[5] A.M. Shaikh, Applications of various imaging techniques in neutron radiography at BARC, Trombay, 18th World Conf. Nondestruct. Testing, 16-20 April 2012, Durban, South Africa. (2012) 16-20.

[6] E. Lehmann, M. Raventos, R.P. Harti, P. Trtik, A. Kaestner, D. Mannes, C. Grünzweig, Methodical Progress in Neutron Imaging at PSI, Phys. Procedia. 88 (2017) 250-257. https://doi.org/10.1016/j.phpro.2017.06.035.

[7] N. Kardjilov, I. Manke, M. Strobl, A. Hilger, W. Treimer, M. Meissner, T. Krist, J. Banhart, Three-dimensional imaging of magnetic fields with polarized neutrons, Nat. Phys. 4 (2008) 399-403. https://doi.org/10.1038/nphys912.

[8] A. Hilger, I. Manke, N. Kardjilov, M. Osenberg, H. Markötter, J. Banhart, Tensorial neutron tomography of three-dimensional magnetic vector fields in bulk materials, Nat. Commun. (2018). https://doi.org/10.1038/s41467-018-06593-4.

[9] P. von der Hardt, H. Roettger, Neutron Radiography Handbook, Springer Netherlands, Dordrecht, 1981. https://doi.org/10.1007/978-94-009-8567-4.

[10] S. Koerner, E. Lehmann, P. Vontobel, Design and optimization of a CCD-neutron radiography detector, Nucl. Instru. Meth. Phys.

Res. Sect. A Accel. Spectrometers, Detect. Assoc. Equip. 454 (2000) 158-164. https://doi.org/10.1016/S0168-9002(00)00819-6.
[11] S. Saha, H.J. Kim, A. Khan, D.J. Daniel, R. Absar, R. Barman, P. Aryal, J. Kaewkhao, S. Kothan, Luminescence and Scintillation Properties of Dy^{3+} doped $Li_6Y(BO_3)_3$ crystal, Opt. Mater. (Amst). 106 (2020) 109973. https://doi.org/10.1016/j.optmat.2020.109973.
[12] D.M. Schubert, Borates in Industrial Use, 2003. https://doi.org/10.1007/3-540-46110-8_1.
[13] Q. Wei, Y.-J. Zhang, Y. Song, G.-Y. Yang, X. Zou, A series of inorganic-organic hybrid cadmium borates with novel Cd-centred $[Cd@B14O20(OH)6]^{2-}$ clusters, Dalt. Trans. 45 (2016) 13937-13943. https://doi.org/10.1039/C6DT02875F.
[14] S. Saha, H.J. Kim, A. Khan, J. Cho, S. Kang, A. V. Ntarisa, Synthesis and luminescence studies of Dy^{3+} doped $Li_3Sc(BO_3)_2$ polycrystalline powder for warm white light, Ceram. Int. 48 (2022) 10667-10676. https://doi.org/10.1016/j.ceramint.2021.12.281.
[15] C. Huang, M. Mutailipu, F. Zhang, K.J. Griffith, C. Hu, Z. Yang, J.M. Griffin, K.R. Poeppelmeier, S. Pan, Expanding the chemistry of borates with functional $[BO_2]^-$ anions, Nat. Commun. 12 (2021) 2597. https://doi.org/10.1038/s41467-021-22835-4.
[16] S. Pan, J. Zhang, J. Pan, G. Ren, N. Li, Z. Wu, Y. Heng, Optimized crystal growth and luminescence properties of Ce^{3+} ions doped $Li_6Gd(BO_3)_3$, $Li_6Y(BO_3)_3$ and their mixed crystals, J. Alloys Compd. 751 (2018) 129-137. https://doi.org/10.1016/j.jallcom.2018.04.099.
[17] A.K. Singh, M. Tyagi, S.G. Singh, B. Tiwari, D.G. Desai, S. Sen, S.S. Desai, S.S. Ghodke, S.C. Gadkari, Performance characteristics of thermal neutron detectors based on $Li_6Y(BO_3)_3$:Ce single crystals, Nucl. Instruments Methods Phys. Res. Sect. A Accel. Spectrometers, Detect. Assoc. Equip. 804 (2015) 189-193. https://doi.org/10.1016/j.nima.2015.09.077.
[18] U. Fawad, M. Oh, H. Park, S. Kim, H.J. Kim, Luminescent investigations of $Li_6Lu(BO_3)_3$:Tb^{3+}, Dy^{3+}phosphors, J. Alloys Compd. 610 (2014) 281-287. https://doi.org/10.1016/j.jallcom.2014.05.001.
[19] T.S. Koroleva, M.M. Kidibaev, A. Nehari, C. Pedrini, K. Lebbou, A.N. Belsky, A.N. Tcherepanov, A. V. Ishchenko, V.Y. Ivanov,

I.N. Sedunova, O.S. Teslenko, L. V. Viktorov, B. V. Shulgin, L.H. Zheng, J. Xu, V. Kononets, O. Sidletskiy, Ce-doped $Li_6Ln(BO_3)_3$ (Ln = Y, Gd) Single crystals fibers grown by micro-pulling down method and luminescence properties, Opt. Mater. (Amst). 35 (2013) 868-874. https://doi.org/10.1016/j.optmat.2012.10.045.

[20] K. Mariselvam, R.A. Kumar, Borate Glasses for Luminescence Applications - Potential Materials for White LEDs and Laser Sources, Univers. J. Chem. 4 (2016) 55-64. https://doi.org/10.13189/ujc.2016.040202.

[21] A.K. Varshneya, J.C. Mauro, Fundamentals of Inorganic Glasses, Elsevier, 2019. https://doi.org/10.1016/C2017-0-04281-7.

[22] RC TRITEC AG, (2022). https://www.rctritec.com/de/home.html.

[23] B. Schillinger, S. Saha, The Signal Chain - how the Removal of an Image Intensifier at the AERE Reactor in Bangladesh Improves Neutron Imaging, Phys. Procedia. 88 (2017) 243-249. https://doi.org/10.1016/j.phpro.2017.06.034.

[24] S. Saha, H.J. Kim, P. Aryal, M. Tyagi, R. Barman, J. Kaewkhao, S. Kothan, S. Kaewjaeng, Synthesis and characterization of borate glasses for thermal neutron scintillation and imaging, Radiat. Meas. 134 (2020) 106319. https://doi.org/10.1016/j.radmeas.2020.106319.

[25] Y. Ou, W. Zhou, D. Hou, M.G. Brik, P. Dorenbos, Y. Huang, H. Liang, Impacts of 5d electron binding energy and electron-phonon coupling on luminescence of Ce^{3+} in $Li_6Y(BO_3)_3$, RSC Adv. 9 (2019) 7908-7915. https://doi.org/10.1039/c9ra00381a.

[26] A.M. Srivastava, Aspects of Pr^{3+} luminescence in solids, J. Lumin. 169 (2016) 445-449. https://doi.org/10.1016/j.jlumin.2015.07.001.

[27] W.W. Piper, J.A. DeLuca, F.S. Ham, Cascade fluorescent decay in Pr^{3+}-doped fluorides: Achievement of a quantum yield greater than unity for emission of visible light, J. Lumin. 8 (1974) 344-348. https://doi.org/10.1016/0022-2313(74)90007-6.

[28] E.Y. Wong, Configuration Interaction of the Pr^{3+} Ion, J. Chem. Phys. 38 (1963) 976-978. https://doi.org/10.1063/1.1733794.

[29] S. Saha, A. Khan, H.J. Kim, P.Q. Vuong, I.R. Pandey, J. Kaewkhao, S. Kothan, N. Kiwsakunkran, Luminescence and scintillation properties of Czochralski grown Pr^{3+} doped $Li_6Y(BO_3)_3$ single crystal, Opt. Mater. (Amst). 119 (2021) 111361.

https://doi.org/10.1016/j.optmat.2021.111361.
[30] G.F. Knoll, Radiation detection and measurement, 4th ed., John Wiley and Sons, Inc., 1981. https://www.wiley.com/en-kr/Radiation+Detection+and+Measurement,+4th+Edition-p-9780470131480.
[31] V.I. Groshev, L. V., Demidov, A. M., Ivanov, V. A., Lutsenko, V. N., & Pelekhov, Gamma-rays and conversion electrons from the (n, γ) reaction on gadolinium isotopes, Izv. Akad. Nauk SSSR. 26 (1962) 1119-1133.
[32] G.C. Smith, Neutron Imaging, Radiography Tomography*, Instrumentation. (2002).
[33] C.W.E. van Eijk, Neutron detection and neutron dosimetry, Radiat. Prot. Dosimetry. 110 (2004) 5-13. https://doi.org/10.1093/rpd/nch155.
[34] Z. Fu, S. Pan, F. Yang, S. Gu, X. Lei, Y. Heng, G. Ren, M. Qi, Neutron detection properties of $Li_6Y(BO_3)_3$:Ce crystal, Radiat. Meas. 72 (2015) 39-43. https://doi.org/10.1016/j.radmeas.2014.11.010.
[35] P. Bilski, B. Marczewska, M. Kłosowski, W. Gieszczyk, M. Naruszewicz, Detection of neutrons with LiF fluorescent nuclear track detectors, Radiat. Meas. 116 (2018) 35-39. https://doi.org/10.1016/j.radmeas.2018.06.022.
[36] M.A. Stanojev Pereira, R. Pugliesi, F. Pugliesi, Neutron induced alpha radiography, Radiat. Meas. 43 (2008) 1226-1230. https://doi.org/10.1016/j.radmeas.2008.02.012.
[37] D.J. Hughes, L.B. Borst, Neutron Cross Sections, Phys. Today. 11 (1958) 43-43. https://doi.org/10.1063/1.3062525.
[38] V.F. Sears, Neutron scattering lengths and cross sections, Neutron News. 3 (1992) 26-37. https://doi.org/10.1080/10448639208218770.
[39] J.E. Turner, Atoms, Radiation, and Radiation Protection, Wiley, 2007. https://doi.org/10.1002/9783527616978.
[40] P.A. Rodnyi, P. Dorenbos, C.W.E. van Eijk, Energy Loss in Inorganic Scintillators, Phys. Status Solidi. 187 (1995) 15-29. https://doi.org/10.1002/pssb.2221870102.
[41] Mikhail S. Alekhin, New halide scintillators for γ-ray detection, Delft University, 2013. http://repository.tudelft.nl/assets/uuid:6048c4dc-84c9-48f5-98e7-d5a19cdc6800/Thesis_online.pdf.

[42] B.C.G. G. Blasse, Luminescent Materials, Springer-Verlag, 1994.
[43] Arshad Khan, Development of Tl-based Novel (La, Gd, Ca) Chloride Scintillators for Radiation Detection, Kyungpook National University, 2020.
[44] P. Atkins, M.H. Tina Overton, Jonathan Rourke, Mark Weller, Fraser Armstrong, Inorganic Chemistry, 5th ed., W. H. Freeman and Company, New York, USA, 2010.
[45] J.M. Ogieglo, Luminescence and Energy Transfer in Garnet Scintillators, University of Utrecht, Netherland, 2012.
[46] P. Dorenbos, The 4f ↔ 4f-5d transitions of the trivalent lanthanides in halogenides and chalcogenides, J. Lumin. 91 (2000) 91-106. https://doi.org/10.1016/S0022-2313(00)00197-6.
[47] L. Brewer, Energies of the Electronic Configurations of the Singly, Doubly, and Triply Ionized Lanthanides and Actinides, J. Opt. Soc. Am. 61 (1971) 1666. https://doi.org/10.1364/josa.61.001666.
[48] K. Ogasawara, S. Watanabe, Y. Sakai, H. Toyoshima, T. Ishii, M.G. Brik, I. Tanaka, Calculations of complete $4f^n$ and $4f^{n-1}5d^1$ energy level schemes of free trivalent rare-earth ions, Japanese J. Appl. Physics, Part 2 Lett. 43 (2004). https://doi.org/10.1143/jjap.43.1611.
[49] Gerhard Heinrich Dieke, G.H. Dieke, H.M. Crosswhite, H.M. Crosswhite, Spectra and Energy Levels of Rare Earth Ions in Crystals, John Wiley & Sons, Inc, New York, 1968. https://books.google.co.kr/books?id=mM84AAAACAAJ.
[50] H.N.R. and F.A. Saunders, New Regularities in the Spectra of the, Astrophys. J. 61 (1925) 38-69.
[51] C.R. Ronda, T. Jüstel, H. Nikol, Rare earth phosphors: Fundamentals and applications, J. Alloys Compd. 275-277 (1998) 669-676. https://doi.org/10.1016/S0925-8388(98)00416-2.
[52] M.R. Hawkesworth, J. Walker, Review: Radiography with neutrons, J. Mater. Sci. 4 (1969) 817-835. https://doi.org/10.1007/BF00551079.
[53] P. Von Der Hardt, H. Röttger, Principles and Practice of Neutron Radiography, in: Neutron Radiogr. Handb., (2011). https://doi.org/10.1007/978-94-009-8567-4_1.
[54] Standard Test Method for Determining the L / D Ratio of Neutron Radiography Beams 1, ASTM, 1996. https://gost-snip.su/download/astm_e_803_91_standard_test_method_for_deter

mining_the_l_d_r.
[55] J. Jakůbek, S. Pospíšil, J. Uher, J. Vacík, D. Vavřík, Properties of the single neutron pixel detector based on the Medipix-1 device, Nucl. Instruments Methods Phys. Res. Sect. A Accel. Spectrometers, Detect. Assoc. Equip. 531 (2004) 276-284. https://doi.org/10.1016/j.nima.2004.06.017.
[56] J.O. P. Gade-Nielsen, NEUTRON RADIOGRAPHY, D. REIDEL PUBLISHING COMPANY, 1883. https://doi.org/10.1016/0048-9697(89)90300-8.
[57] M. Welvaert, Y. Rosseel, On the definition of signal-to-noise ratio and contrast-to-noise ratio for fMRI data, PLoS One. 8 (2013). https://doi.org/10.1371/journal.pone.0077089.
[58] S.E. Joel, B.S. Caffo, P.C.M. Van Zijl, J.J. Pekar, On the relationship between seed-based and ICA-based measures of functional connectivity, Magn. Reson. Med. 66 (2011) 644-657. https://doi.org/10.1002/mrm.22818.
[59] K. Persson, Materials Data on $Li_6Y(BO_3)_3$ (SG:14) by Materials Project, 2014. https://doi.org/10.17188/1190843.
[60] I.R. Pandey, Development and characterization of Mo / W based oxide crystals for rare event search experiment, Kyungpook National University, 2018.
[61] C. Leroy, P.-G. Rancoita, Principles of Radiation Interaction in Matter and Detection, 4th ed., WORLD SCIENTIFIC, 2016. https://doi.org/10.1142/9167.
[62] I.R. Pandey, S. Karki, H.J. Kim, Y.D. Kim, M.H. Lee, N. V. Ivannikova, Luminescence and Scintillation Properties of Novel Disodium Dimolybdate ($Na_2Mo_2O_7$) Single Crystal, IEEE Trans. Nucl. Sci. 65 (2018) 2125-2131. https://doi.org/10.1109/TNS.2018.2822340.
[63] P.Q. Vuong, H. Kim, H. Park, G. Rooh, S. Kim, Pulse shape discrimination study with Tl_2ZrCl_6 crystal scintillator, Radiat. Meas. 123 (2019) 83-87. https://doi.org/10.1016/j.radmeas.2019.02.007.
[64] K. Boonin, W. Sa-ardsin, J. Kaewkhao, The luminescence characteristics of Eu^{3+}-doped lithium-gadolinium borate glasses, SNRU J. Sci. Technol. 8 (2016) 122-126. https://doi.org/10.14456/snrujst.2016.16.
[65] E. Kaewnuam, N. Chanthima, C.K. Jayasankar, H.J. Kim, J. Kaewkhao, Optical, Luminescence and Judd-Oflet Study of Eu^{3+} Doped Lithium Yttrium Borate Glasses for Using as Laser Gain

Medium, Key Eng. Mater. 675-676 (2016) 364-367. https://doi.org/10.4028/www.scientific.net/KEM.675-676.364.
[66] S. Kaewjaeng, S. Kothan, H. Kim, J. Kaewkhao, Comparison study of Dy^{3+} and Eu^{3+} of Gd_2O_3-CaO-SiO_2-B_2O_3 Glasses with BGO Crystal, in: Proc. Int. Conf. Technol. Soc. Sci., 2017: pp. 0-5.
[67] R. Pynn, Neutron Applications in Earth, Energy and Environmental Sciences, Springer US, Boston, MA, 2009. https://doi.org/10.1007/978-0-387-09416-8.
[68] J. Czochralski, Ein neues Verfahren zur Messung der Kristallisationsgeschwindigkeit der Metalle, Zeitschrift Für Phys. Chemie. 92U (1918) 219-221. https://doi.org/10.1515/zpch-1918-9212.
[69] R. Uecker, The historical development of the Czochralski method, J. Cryst. Growth. 401 (2014) 7-24. https://doi.org/10.1016/j.jcrysgro.2013.11.095.
[70] A.D.W. Jones, Hydrodynamics Of Czochralski Growth - A Review Of The Effects Of Rotation And Buoyancy Force, Prog. Cryst. Growth Charact. 9 (1984) 139-168.
[71] M.S. Akselrod, F.J. Bruni, Modern trends in crystal growth and new applications of sapphire, J. Cryst. Growth. 360 (2012) 134-145. https://doi.org/10.1016/j.jcrysgro.2011.12.038.
[72] Á. Péter, K. Polgár, M. Tóth, Synthesis and crystallization of lithium-yttrium orthoborate $Li_6Y(BO_3)_3$ phase, J. Cryst. Growth. 346 (2012) 69-74. https://doi.org/10.1016/j.jcrysgro.2012.02.034.
[73] U. Fawad, H.J. Kim, S. Khan, M. Khan, L. Ali, Photoluminescent properties of white-light-emitting $Li_6Y(BO_3)_3$:Dy^{3+}phosphor, Solid State Sci. 62 (2016) 1-5. https://doi.org/10.1016/j.solidstatesciences.2016.08.008.
[74] K. Alam, R. Islam, S. Saha, N. Islam, S.A. Islam, Quality Study of Automated Machine Made Environmentally Friendly Brick (KAB) Sample Using Film Neutron Radiography Technique, J. Build. Constr. Plan. Res. 01 (2013) 141-152. https://doi.org/10.4236/jbcpr.2013.14015.
[75] S. Saha, M.N. Islam, M.K. Alam, A.K.M. Azad Rahman, M.H. Ahsan, A Study of the internal defects of Terrazzo and Engraved construction materials using direct film neutron radiography technique, Proc. Pakistan Acad. Sci. 51 (2014) 331-336.
[76] J.S. Brenizer, Current and Future Neutron Radiography Standards,

in: Int. Conf. Nucl. Energy Cent. Eur., 1999: pp. 17-24.
[77] A.E. Craft, B.A. Hilton, G.C. Papaioannou, Characterization of a Neutron Beam Following Reconfiguration of the Neutron Radiography Reactor (NRAD) Core and Addition of New Fuel Elements, Nucl. Eng. Technol. 48 (2016) 200-210. https://doi.org/10.1016/j.net.2015.10.006.
[78] L. Lutterotti, Maud: a Rietveld analysis program designed for the internet and experiment integration, Acta Crystallogr. Sect. A Found. Crystallogr. 56 (2000) s54-s54. https://doi.org/10.1107/S0108767300021954.
[79] F. Ullah, Development and Characterization of Inorganic Borate Phosphor and Crystal Scintillators, Thesis, 2013.
[80] F. Timischl, The contrast-to-noise ratio for image quality evaluation in scanning electron microscopy, Scanning. 37 (2015) 54-62. https://doi.org/10.1002/sca.21179.
[81] Z.Wang, A.C.Bovik, A Universal Image Quality Index, IEEE Signal Process. Lett. 09 (2002) 81-84. https://doi.org/10.1109/97.995823.
[82] E. Browne, NDS 82, 379 (1997), n.d. http://nucleardata.nuclear.lu.se/toi/nuclide.asp?iZA=380090.
[83] A.N. Annenkov, O.A. Buzanov, F.A. Danevich, A.S. Georgadze, S.K. Kim, H.J. Kim, Y.D. Kim, V. V. Kobychev, V.N. Kornoukhov, M. Korzhik, J.I. Lee, O. Missevitch, V.M. Mokina, S.S. Nagorny, A.S. Nikolaiko, D. V. Poda, R.B. Podviyanuk, D.J. Sedlak, O.G. Shkulkova, J.H. So, I.M. Solsky, V.I. Tretyak, S.S. Yurchenko, Development of $CaMoO_4$ crystal scintillators for a double beta decay experiment with ^{100}Mo, Nucl. Instruments Methods Phys. Res. Sect. A Accel. Spectrometers, Detect. Assoc. Equip. 584 (2008) 334-345. https://doi.org/10.1016/j.nima.2007.10.038.
[84] P.Q. Vuong, H.J. Kim, A. Khan, S. Khan, S.H. Kim, H. Park, J. Kim, Silver-Doped LiI Crystal: A Sensitive Thermal Neutron Detector With Pulse Shape Discrimination, IEEE Trans. Nucl. Sci. 67 (2020) 2290-2294. https://doi.org/10.1109/TNS.2020.3004936.
[85] R. Brun, F. Rademakers, ROOT - An object oriented data analysis framework, Nucl. Instruments Methods Phys. Res. Sect. A Accel. Spectrometers, Detect. Assoc. Equip. 389 (1997) 81-86. https://doi.org/10.1016/S0168-9002(97)00048-X.
[86] H.J. Kim, A.N. Annenkov, R.S. Boiko, O.A. Buzanov, D.M. Chernyak, J.H. Cho, F.A. Danevich, A.E. Dossovitsky, G. Rooh,

U.K. Kang, M.J. Kim, S.C. Kim, S.K. Kim, Y.D. Kim, V. V. Kobychev, V.N. Kornoukhov, M.B. Kosmyna, S.J. Lee, J.I. Lee, J.H. Lee, S.S. Myung, B.P. Nazarenko, A.S. Nikolaiko, R.B. Podviyanuk, V.M. Puzikov, A.N. Shekhovtsov, J.H. So, I. Solskii, V.I. Tretyak, A. V. Veresnikova, Neutrino-less double beta decay experiment using $Ca^{100}MoO_4$ scintillation crystals, IEEE Trans. Nucl. Sci. 57 (2010) 1475-1480. https://doi.org/10.1109/TNS.2010.2043264.

[87] S. Arunkumar, K. Venkata Krishnaiah, K. Marimuthu, Structural and luminescence behavior of lead fluoroborate glasses containing Eu^{3+} ions, Phys. B Condens. Matter. 416 (2013) 88-100. https://doi.org/10.1016/j.physb.2013.02.022.

[88] N. Wantana, E. Kaewnuam, B. Damdee, S. Kaewjaeng, S. Kothan, H.J. Kim, J. Kaewkhao, Energy transfer based emission analysis of Eu^{3+} doped Gd_2O_3-CaO-SiO_2-B_2O_3 glasses for laser and X-rays detection material applications, J. Lumin. 194 (2018) 75-81. https://doi.org/10.1016/j.jlumin.2017.10.004.

[89] I. Khan, G. Rooh, R. Rajaramakrishna, N. Sirsittapokakun, H.J. Kim, J. Kaewkhao, K. Kirdsiri, Energy transfer phenomenon of Gd^{3+} to excited ground state of Eu^{3+} ions in Li_2O-BaO-Gd_2O_3-SiO_2-Eu_2O_3 glasses, Spectrochim. Acta - Part A Mol. Biomol. Spectrosc. 210 (2019) 21-29. https://doi.org/10.1016/j.saa.2018.11.008.

[90] P.H. Gregson, Using Angular Dispersion of Gradient Direction for Detecting Edge Ribbons, IEEE Trans. Pattern Anal. Mach. Intell. 15 (1993) 682-696. https://doi.org/10.1109/34.221169.

[91] Z.D. Luo, H. Zhang, Y.D. Huang, M.W. Qiu, Y.C. Huang, C.Y. Tu, A.D. Jiang, Study of $Li_6Y(BO_3)_3$:Nd^{3+} Crystal - A New Laser Crystal, Cryst. Res. Technol. 26 (1991) K5-K8. https://doi.org/10.1002/crat.2170260125.

[92] E. Kaewnuam, N. Wantana, H.J. Kim, J. Kaewkhao, Development of lithium yttrium borate glass doped with Dy^{3+} for laser medium, W-LEDs and scintillation materials applications, J. Non. Cryst. Solids. 464 (2017) 96-103. https://doi.org/10.1016/j.jnoncrysol.2017.03.027.

[93] W.T. Carnall, P.R. Fields, K. Rajnak, Electronic Energy Levels in the Trivalent Lanthanide Aquo Ions. I. Pr^{3+}, Nd^{3+}, Pm^{3+}, Sm^{3+}, Dy^{3+}, Ho^{3+}, Er^{3+}, and Tm^{3+}, J. Chem. Phys. 49 (1968) 4424-4442. https://doi.org/10.1063/1.1669893.

[94] L. Xu, H.M. Crosswhite, J.P. Hessler, Fluorescent and dynamic

properties of optically excited dysprosium trifluoride, J. Chem. Phys. 81 (1984) 698. https://doi.org/10.1063/1.447752.
[95] B. Liu, J. Shi, Q. Wang, H. Tang, J. Liu, H. Zhao, D. Li, J. Liu, X. Xu, Z. Wang, J. Xu, Crystal growth and yellow emission of Dy:$YAlO_3$, Opt. Mater. (Amst). 72 (2017) 208-213. https://doi.org/10.1016/j.optmat.2017.06.005.
[96] F. Zhang, T. Zhang, G. Li, W. Zhang, Single phase M+ (M = Li, Na, K), Dy^{3+} co-doped $KSrBP_2O_8$ white light emitting phosphors, J. Alloys Compd. 618 (2015) 484-487. https://doi.org/10.1016/j.jallcom.2014.08.178.
[97] Q. Su, Z. Pei, L. Chi, H. Zhang, Z. Zhang, F. Zou, The yellow-to-blue intensity ratio (Y/B) of Dy^{3+} emission, J. Alloys Compd. 192 (1993) 25-27. https://doi.org/10.1016/0925-8388(93)90174-L.
[98] M.G. Brik, T. Ishii, A.M. Tkachuk, I. Tanaka, Energy Level Structure of $LiYF_4$:Dy^{3+} : Crystal Field Analysis, Mater. Trans. 45 (2004) 2026-2030. https://doi.org/DOI 10.2320/matertrans.45.2026.
[99] E. Cavalli, E. Bovero, A. Belletti, Optical spectroscopy of $CaMoO_4$:Dy^{3+} single crystals, J. Phys. Condens. Matter. 14 (2002) 5221-5228. https://doi.org/10.1088/0953-8984/14/20/317.
[100] E. Cavalli, E. Bovero, N. Magnani, M.O. Ramirez, A. Speghini, M. Bettinelli, Optical spectroscopy and crystal-field analysis of $YAl_3(BO_3)_4$ single crystals doped with dysprosium, J. Phys. Condens. Matter. 15 (2003) 1047-1056. https://doi.org/10.1088/0953-8984/15/7/303.
[101] R. Mao, L. Zhang, R.-Y. Zhu, Optical and Scintillation Properties of Inorganic Scintillators in High Energy Physics, IEEE Trans. Nucl. Sci. 55 (2008) 2425-2431. https://doi.org/10.1109/TNS.2008.2000776.
[102] A. Khan, D.J. Daniel, M. Tyagi, H.J. Kim, M.H. Lee, Y. Kim, Czochralski growth, electronic structure, luminescence and scintillation properties of $Cs_2Mo_3O_{10}$: A new scintillation crystal for $0\nu\beta\beta$ decay search, J. Alloys Compd. 821 (2020) 153466. https://doi.org/10.1016/j.jallcom.2019.153466.
[103] M.J. Knitel, P. Dorenbos, C.W.E. Van Eijk, B. Plasteig, B. Viana, A. Kahn-Harari, D. Vivien, Photoluminescence, and scintillation/thermoluminescence yields of several Ce^{3+} and Eu^{2+} activated borates, Nucl. Instruments Methods Phys. Res. Sect.

A Accel. Spectrometers, Detect. Assoc. Equip. 443 (2000) 364-374. https://doi.org/10.1016/S0168-9002(99)01154-7.
[104] G. Kitis, J.M. Gomez-Ros, J.W.N. Tuyn, Thermoluminescence glow-curve deconvolution functions for first, second and general orders of kinetics, J. Phys. D. Appl. Phys. 31 (1998) 2636-2641. https://doi.org/10.1088/0022-3727/31/19/037.
[105] D. Afouxenidis, G.S. Polymeris, N.C. Tsirliganis, G. Kitis, Computerised curve deconvolution of TL/OSL curves using a popular spreadsheet program, Radiat. Prot. Dosimetry. 149 (2012) 363-370. https://doi.org/10.1093/rpd/ncr315.
[106] I.N. Ogorodnikov, D.O. Vostrov, V.A. Pustovarov, I.N. Sedunova, Thermoluminescence kinetics of $Li_6GdB_3O_9$ crystals, Opt. Mater. (Amst). 36 (2014) 1571-1579. https://doi.org/10.1016/j.optmat.2014.04.033.
[107] J. Kim, M. Cho, S. Westland, M. Luo, Image quality assessment for photographic images, AIC Colour. 5 (2005) 1095-1098. https://doi.org/10.5923/j.ajsp.20150503.01.
[108] E. Lehmann, P. Vontobel, The use of amorphous Silicon flat panels as detector in neutron imaging, Appl. Radiat. Isot. 61 (2004) 567-571. https://doi.org/10.1016/j.apradiso.2004.03.102.
[109] F. Zhang, Y. Wang, Y. Tao, Investigation of the luminescence properties of Tb^{3+} -doped $Li_6Y(BO_3)_3$ phosphors in VUV - VIS range, J. Lumin. 136 (2013) 51-56. https://doi.org/10.1016/j.jlumin.2012.11.021.
[110] S.A. Kiselev, V.A. Pustovarov, Luminescence of $Li_6Y(BO_3)_3$ doped with Pr^{3+} ions under x-ray, electron beam and ultraviolet excitation, in: AIP Publishing, 2019: p. 020120. https://doi.org/10.1063/1.5134271.
[111] A.M. Srivastava, D.A. Doughty, W.W. Beers, On the Vacuum-Ultraviolet Excited Luminescence of Pr^{3+} in LaB_3O_6, J. Electrochem. Soc. 144 (1997) L190-L192. https://doi.org/10.1149/1.1837795.
[112] A.M. Srivastava, D.A. Doughty, W.W. Beers, Photon Cascade Luminescence of Pr^{3+} in $LaMgB_5O_{10}$, J. Electrochem. Soc. 143 (1996) 4113-4116. https://doi.org/10.1149/1.1837346.
[113] A.A. Bagatur'yants, I.M. Iskandarova, A.A. Knizhnik, V.S. Mironov, B. V. Potapkin, A.M. Srivastava, T.J. Sommerer, Energy level structure of 4f5d states and the Stokes shift in $LaPO_4$: Pr^{3+}: a theoretical study, Phys. Rev. B - Condens. Matter Mater.

Phys. 78 (2008) 1-11. https://doi.org/10.1103/PhysRevB.78.165125.
[114] A.K. Singh, M. Tyagi, S.G. Singh, S. Sen, S.S. Desai, S.S. Ghodke, S.C. Gadkari, Performance characteristics of a thermal neutron detector based on $Li_6Y(BO_3)_3$:Ce single crystals, 59 (2014) 896-897.
[115] K. V. Ivanovskikh, V.A. Pustovarov, S. Omelkov, M. Kirm, F. Piccinelli, M. Bettinelli, Phase transition, radio- and photoluminescence of $K_3Lu(PO_4)_2$ doped with Pr^{3+} ions, J. Lumin. 230 (2021) 117749. https://doi.org/10.1016/j.jlumin.2020.117749.
[116] A.K. Singh, M. Tyagi, D.G. Desai, S.G. Singh, S. Sen, S.C. Gadkari, A Comparative Study of $Li_6R(BO_3)_3$; R = Gd, Lu, & Y), Single Crystals for Thermal Neutron Detection, Phys. Status Solidi. 215 (2018) 1800224. https://doi.org/10.1002/pssa.201800224.

열중성자 검출 및 영상화를 위한 붕소 기반 섬광기의 합성과 특성 분석

수딥타 사하

경북대학교 대학원 물리학과 핵물리학전공
(지도교수: 김홍주)

(초 록)

열중성자 이미징 기술은 다양한 응용분야의 요구 사항을 충족하도록 발전되었다. 이 연구는 열중성자 이미징을 위한 섬광 스크린의 목적에 부합할 수 있는 적절한 투명한 결정 화합물을 찾기 위해 진행되었다. 다양한 원소들은 다양한 열 중성자 흡수 단면을 가지며 Li, B, Gd 를 포함한 화합물이 높은 미세 흡수 단면으로 인해 가장 많이 열 중성자를 검출하였다. 선원과 환경의 서로 다른 에너지의 감마선을 고려할 때 섬광기에 의한 열 중성자와 감마선을 구별하는 것이 매우 중요하다.

세 가지 새로운 유리 조성물이 열 중성자와 감마선을 구별하는 능력을 테스트하였다. 진행에 앞서, 열중성자와 감마선을 결정하기 위해 유리샘플의 발광성과 마찬가지로 열중성자 시설의 특성이 측정되었다. 샘플에 Eu^{3+} 이온을 도핑하였고 샘플의 발광성의 특징 또한 측정되었다. 감마선에서 열중성자를 분리하기 위해 디지털 및 필름기반 방사선 촬영 기술을 사용하여 BLIY:1.5Eu 샘플을 확인하였다. 그 결과, $Li_6Y(BO_3)_3$ 는 이상적인 원소를 포함하는 결정 성장 후보로 확인되었다.

Czochralski 방법은 4 mol% Dy^{3+} 와 1 mol% Pr^{3+} 이 첨가된 $Li_6Y(BO_3)_3$ 의 단결정을 성공적으로 성장시키는 데 사용되었다. 이 단결정은 X 선 및 광 들뜸 하에서의 발광 연구를 통해 특성이 확인되었다. 이러한

단결정 샘플의 섬광 성능은 ^{90}Sr, ^{241}Am, ^{60}Co 및 ^{252}Cf 선원에서 나오는 감속 열 중성자와 β^- -및, α -입자, ɣ-선을 사용하여 평가되었다. 성장한 샘플은 핵 원자로 및 방사능 선원에 의해 생성된 감마선과 열 중성자를 구별할 수 있을 만큼 효율적이라는 것이 확인되었다. $Li_6Y(BO_3)_3$ 는 향후 열 중성자 섬광기로 사용이 유망한 것으로 확인되었다.

Appendix-I: Synthesis and characterization of borate glasses for thermal neutron scintillation and imaging

In an effort to identify suitable neutron scintillators, several glassy compositions were synthesized and their performance as the scintillation screen of thermal neutron imaging systems was evaluated. In the current work, three novel compositions with Li, B, and Gd as their primary components, doped with Eu, were produced through melt quenching, and studied for the first-time using neutron imaging. By using X-ray generated emission on these glass samples, the concentration of the luminous activator Eu^{3+} was adjusted. Prior to the comprehensive examination of the thermal neutron scintillation properties of the compositions, beam purity investigations and the luminescence capability of the commercial screen were also conducted. The glass samples were subjected to thermal neutrons for 5 and 10 minutes at the beam port of the research reactor in order to evaluate their performance using the traditional direct film neutron radiography method. Due to the energy transfer from Gd ions to Eu activators, it was discovered that Gd-containing glasses produced more luminescent photons. However, the composition of $60Li_2O_3{:}10Y_2O_3{:}28.5B_2O_3{:}1.5Eu_2O_3$ (mol%) was found to have high thermal neutron discrimination property from the gamma background while having the lowest X-ray luminescence of the three varieties.

The research work was reported in this thesis as Chapter 4.1 as well as published as,

S. Saha, H.J. Kim, P. Aryal, M. Tyagi, R. Barman, J. Kaewkhao, S. Kothan, S. Kaewjaeng, *Synthesis and characterization of borate glasses for thermal neutron scintillation and imaging*, Radiat. Meas. 134 (2020) 106319. https://doi.org/10.1016/j.radmeas.2020.106319

Appendix-II: Luminescence and Scintillation Properties of Dy^{3+} doped $Li_6Y(BO_3)_3$ crystal

The orthoborate crystals with a large optical bandgap enable a variety of rare earth ions ($^{Ce3+}$, Dy^{3+}, Eu^{3+}, etc.) to function as activators for effective luminescence. Pure $Li_6Y(BO_3)_3$ (LYBO) and 4 mol% Dy^{3+} doped single crystals were produced utilizing the Czochralski technique in the current investigation. X-ray luminescence, photoluminescence, and thermoluminescence studies have been used to describe the light emission of the produced crystals. Under X-ray stimulation, the pure crystal exhibited an intrinsic luminescence property at 330 nm, whereas the doped crystal exhibited the typical emission of Dy^{3+} -ions. The photoluminescence investigation of the doped crystal at low temperature revealed that the peak intensity rose as the temperature decreased from 290 to 10 K. At temperatures ranging from 290 to 10 K, the decay time, which comprises of three components at each stage, was measured. At temperatures ranging from 320 K to 10 K, the thermally induced luminescence of both pure and 4 mol percent Dy^{3+} -doped LYBO crystals was compared. Scintillation β^- counts are measured between 300 and 10 K. The performance of the doped crystal as a scintillator for thermal neutron imaging was also evaluated.

The work was reported in this thesis as Chapter 4.2 and published as,

S. Saha, H.J. Kim, A. Khan, D.J. Daniel, R. Absar, R. Barman, P. Aryal, J. Kaewkhao, S. Kothan, *Luminescence and Scintillation Properties of Dy^{3+} doped $Li_6Y(BO_3)_3$ crystal*, Opt. Mater. (Amst). 106 (2020) 109973. https://doi.org/10.1016/j.optmat.2020.109973.

Appendix-III: Luminescence and scintillation properties of Czochralski grown Pr^{3+} doped $Li_6Y(BO_3)_3$ single crystal

$Li_6Y(BO_3)_3:Pr^{3+}$, an alkali orthoborate compound, has been produced as polycrystalline powders with varying Pr^{3+} rare-earth doping concentrations. The clear single crystal was also produced in an argon environment using the Czochralski technique with 1 mol% Pr^{3+} doping. The crystal's structure is monoclinic, and its space group is $P2_1/c$. To examine the luminescence characteristics with X-ray, UV, α -particles, and γ -ray excitations, the crystal has been faceted and optically polished. The crystal exhibited relaxed 4f15d-4f2 emission at 309 nm in addition to transitional $4f^2$-$4f^2$ emission. The UV−Vis−NIR absorption spectrum was obtained between 250 and 2000 nm. Above 300 nm, the transmittance of the crystal was ∼50%. The Commission International De l'Eclairage (CIE) chromaticity diagram illustrates the variation in combined emission colors at various excitation positions. With γ -rays from ^{60}Co, α -particles from ^{241}Am, and moderated thermal neutrons from a ^{252}Cf source, the scintillation characteristics of the crystal have been examined. Pulse shape discrimination for γ-rays, α -particles, and moderated thermal neutrons has shown the capability of this scintillator to detect thermal neutrons.

The research was reported in this thesis as Chapter 4.3 and the published article can be found as,

S. Saha, A. Khan, H.J. Kim, P.Q. Vuong, I.R. Pandey, J. Kaewkhao, S. Kothan, N. Kiwsakunkran, *Luminescence and scintillation properties of Czochralski grown Pr^{3+} doped $Li_6Y(BO_3)_3$ single crystal*, Opt. Mater. (Amst). 119 (2021) 111361. https://doi.org/10.1016/j.optmat.2021.111361

Appendix-IV: Studies of Dy^{3+} doped $Li_3Sc(BO_3)_2$ Polycrystalline Powder for Warm White Light

Introduction

The performance of wLEDs is greatly influenced by luminescent phosphors, which are made up of a crystalline host and an activator. Red-green-blue (RGB) emitting color phosphors triggered by *n*-UV LEDs (360–420 nm) have been the subject of recent investigations to improve the color rendering capabilities of white and multicolor emitting phosphors. Due to its unique excitation in the UV region (~350 nm), strong physical, chemical, and thermal stability, non-hygroscopic nature, and modest manufacturing process, triply-ionized dysprosium (Dy^{3+}) doped borate phosphor may be considered a viable candidate for such use. The majority of the boron-oxygen (B-O) bonds in the borate compounds provide three- or four-fold coordinated anions (such as BO_3^{3-}, $B_3O_6^{3-}$, and BO_4^-). The structure of $A_3X(BO_3)_2$ (where A= Li, Na and X= Sc, Y, Gd, La) and the potential of doping them with rare earths were disclosed by earlier study on $(BO_3)^{3-}$ compounds. Depending on the uses, these transition metal-based metal alkali orthoborates can be changed to produce a compound with the necessary atomic number and density. In order to find such photoelectric functional materials, our group recently undertook an extensive research of a less known Li_2O–Sc_2O_3–B_2O_3 combination, which confirmed the presence of the borate possessing lower density (2.62 g/cm^3). $Li_3Sc(BO_3)_2$ is the chemical formula for the substance. The structure of $Li_3Sc(BO_3)_2$ was initially determined by H. Sun in his Ph.D. dissertation at Oregon State University (1989).

In this work, the solid-state reaction technique is optimized for the production of the chemical $Li_3Sc(BO_3)_2$. Following the confirmation of crystalline phases, Dy^{3+} ions were initially introduced as an activator within the polycrystalline powder form of the host $Li_3Sc(BO_3)_2$ compound. The synthesized material was examined to determine its effective atomic number (Zeff), crystalline structure, surface morphology, field emission scanning electron microscopy (FE-SEM) measurements, optical properties to show the optical energy gap and absorption spectra, radioluminescence with X-ray and proton beam excitation, UV-Vis-NIR excitation and emission, and decay time estimation.

The polycrystalline powder form of $Li_3Sc(BO_3)_2$ compound with high purity using solid-state reaction process following eqn (1)

$$3Li_2CO_3 + Sc_2O_3 + 2B_2O_3 \rightarrow 2Li_3Sc(BO_3)_2 + 3CO_2 \uparrow \quad (1)$$

Results and Discussions

The effective atomic number of the compound was determined to be ~13. Fig. 1 illustrates the comparison of the experimental results with the reference (PDF 98-024-1234) acquired from the International Center for Diffraction Data. The diffracted peak locations and intensities were in excellent agreement with the reference, as shown in the residual part. The experimental data had a figure of merit of 1.747 with the calculated data, which suggests high consistency. The synthesized chemical was found to crystallize in a monoclinic form with a space group of $P2_1/n$. The computed unit cell volume and density of the sample were 234.34 Å^3 and 2.59 g·cm-3, respectively, having the following lattice parameters: a = 4.796 Å, b = 5.97 Å, c = 8.184 Å, and β = 90.696°. The lattice properties are virtually comparable to the previously reported single crystal generated utilizing the flux approach.

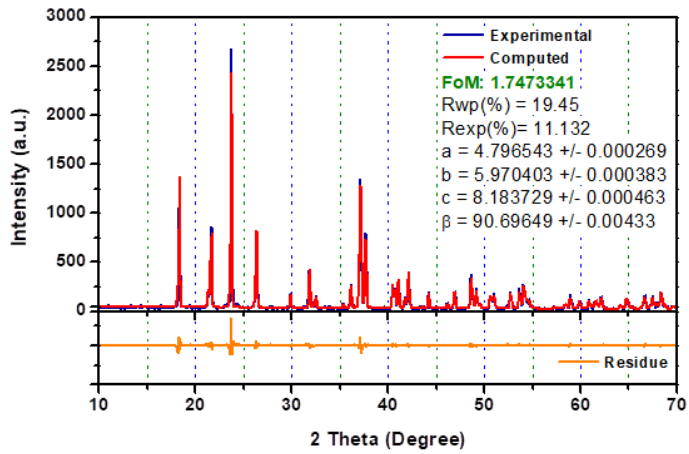

Fig. 1. Rietveld refined spectra of pure $Li_3Sc(BO_3)_2$ phosphor where the blue spectrum is drawn over the experimental data, and the red spectrum shows computed data.

FE-SEM of unadulterated and 4 mol% Dy^{3+}-doped $Li_3Sc(BO_3)_2$ Fig. 2 (a–d) and (e–h) show, respectively, two polycrystalline compounds. In this investigation, powders sintered at 850 °C were employed to determine the surface morphology. As found for the pure sample, the agglomeration of particles with comparable morphologies resulted in roughly homogeneous clusters (Fig. 2 (a, b)). The edges were smooth, with a few particles on the top, probably as a result of high-temperature combustion (Fig. 2 (b, c)). The distribution of particle size (diameter) is shown in the pie chart (Fig. 2 (d)), which indicates that 57% of the particles have a diameter between 6 and 9 μm. Incorporating Dy^{3+}, which has larger atomic radii than Sc^{3+}, altered the morphology of the doped material. The size of the particles grew, but their forms became more distinct, with less aggregation and inhomogeneous diffusion (Fig. 2 (e, f)). In addition, the number of surface aggregates increased (Fig. 2 (f) and (g)). The pie chart depicting the distribution of particle size (width) (Fig. 2 (h)) reveals that about 55% of particles have a width between 13 and 16 μm.

The optical bandgap is a crucial property for a compound that indicates the potential for luminescence when dopant components are present. To acquire the optical bandgap of the pure compound and the absorption spectra of the 4 mol% Dy^{3+}-doped $Li_3Sc(BO_3)_2$ and $Li_6Y(BO_3)_3$ for comparison, a diffuse reflectance experiment was performed. Using this data, the Kubelka-Munk (K-M) function was determined. In addition, it was used to determine the optical bandgap of the pure $Li_3Sc(BO_3)_2$ polycrystalline material, as described in the scientific literature. The K-M function, $F(R_\infty)$, may be calculated from reflectance data using the following eqn (2).

$$F(R_\infty) = \frac{(1-R_\infty)^2}{2R_\infty} = \frac{K}{S}, \qquad (2)$$

where $R_\propto$ stands for the reflectance value (normalized to unity). It was determined that the powder sample had an infinite thickness ($>$1.5 mm) since no incident beam could pass through it. The coefficients of absorption and scattering are denoted by K and S, respectively. Fig. 3 depicts the plot of $(F(R_\propto) \times h\nu)^2$ vs $h\nu$. By extrapolating the linear portion of the spectrum, the direct optical bandgap of pure $Li_3Sc(BO_3)_2$ was determined to be 3.13 eV.

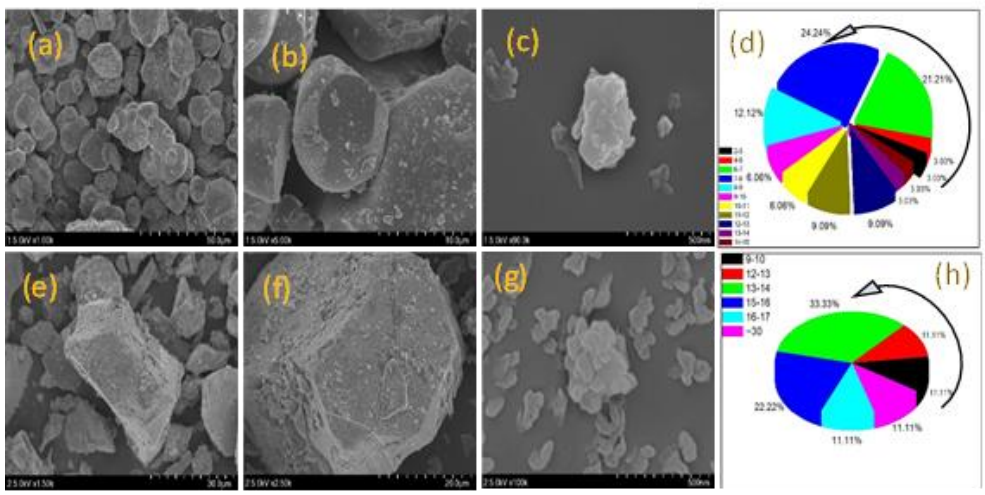

Fig. 2. ((a), (b)) The FE-SEM images, (c) the aggregates on particles, and (d) distribution of particle sizes (μm) of the pure $Li_3Sc(BO_3)_2$ phosphor. ((e), (f)) FE-SEM images, (g) the aggregates on particles, and (h) distribution of particle sizes (μm) of 4 mol.% Dy^{3+}-doped $Li_3Sc(BO_3)_2$ phosphor.

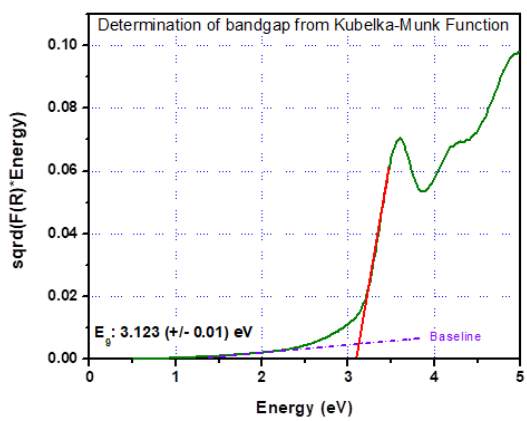

Fig. 3. The estimation of bandgap energy using reflectance data in the Tauc plot, identifying the intersection of the linear region and the baseline for the pure $Li_3Sc(BO_3)_2$ phosphor sample.

The luminescence qualities were established via photoluminescence investigations. In order to comprehend the luminescence process of Dy^{3+} ions in a crystal structure, it is essential to record and research the cross-relaxation process. The approach of non-radiative transitions (non-luminescent) involves a process of cross-relaxation. It has a significant impact on emission quenching and reducing the decay period; thus, it should be explored. In the instance of Dy^{3+} ions, the non-radiative energy transfer model for the depopulation of the $^4F_{9/2}$ level involves the three cross-relaxation channels (CRC) called CRC-1, CRC-2, and CRC-3, respectively.

CRC - 1: $^4F_{9/2} + {}^6H_{15/2} \rightarrow {}^6F_{11/2} + {}^6F_{3/2}$
CRC - 2: $^4F_{9/2} + {}^6H_{15/2} \rightarrow {}^6F_{5/2} + ({}^6F_{9/2} / {}^6H_{7/2})$
CRC - 3: $^4F_{9/2} + {}^6H_{15/2} \rightarrow {}^6F_{1/2} + ({}^6F_{11/2} / {}^6H_{9/2})$

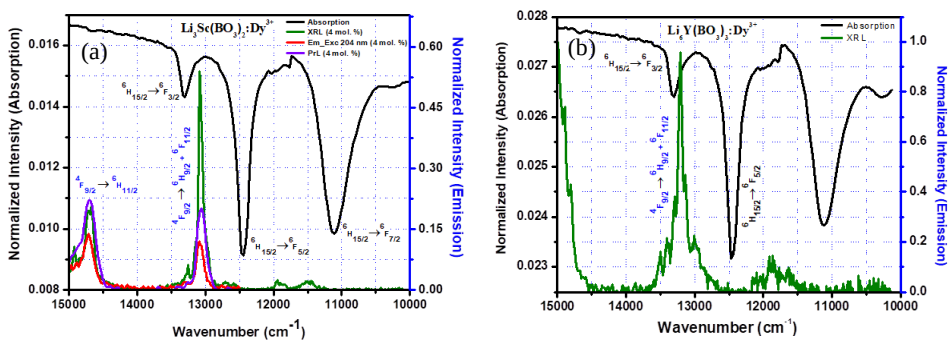

Fig. 4. (a). Comparison of absorption (black) and emission induced by X-ray (green), Proton beam (violet) and UV photons (red) plotted over wavenumbers to identify the possible overlap in cross-relaxation channel (CRC-1) for the 4 mol% Dy^{3+}-doped $Li_3Sc(BO_3)_2$ sample. (b) Comparison of absorption (black) and X-ray induced emission (green) plotted over wavenumbers to identify the possible overlap in cross-relaxation channel (CRC-1) for the 4 mol.% Dy^{3+}-doped $Li_6Y(BO_3)_3$ sample.

The absorption (K-M function) and emission spectra induced by X-ray and UV are plotted over wavenumbers, k (= $\frac{1}{\lambda}$), ranging from 15000 to 10000 cm^{-1}, to identify the possible overlap in CRC – 1 for the samples of 4 mol% Dy^{3+}-doped $Li_3Sc(BO_3)_2$ and $Li_6Y(BO_3)_3$ compounds, as depicted in Figs. 4 (a) and 4 (b), respectively. The emission intensity data, $I(\lambda)d\lambda$, were transformed to I(k)dk so as not to discriminate between observations of various configurations. (b) The XRL peak (13197 cm-1) coincided with the absorption peak (peak: 13303 cm^{-1}) for the $^6H_{15/2} \rightarrow {}^6F_{3/2}$ transition. It induces cross-relaxation, which decreases peak intensity; it may explain the findings on $CaMoO_4:Dy^{3+}$ crystal, $BaNb_2O_6:Dy^{3+}$ phosphor, and others. Nevertheless, the XRL and PL emission peaks for the $Li_3Sc(BO_3)_2$ host at 13088 cm^{-1} (765 nm) have less energy than the absorption peak at 13301 cm^{-1}. It renders the CRC -1 obsolete and is a likely cause of the extremely (XRL) or moderately (PL and PrL) strong emission peak at 765 nm (see Figure 4 (a)). Similar studies may be conducted on $Sr_2CaWO_6:Dy^{3+}$ phosphors and $CaF_2:Dy^{3+}$ crystal, since their emission properties are comparable.

Fig. 5 shows the plotted coordinates (x, y) on the CIE 1931 diagram, which were generated from emission spectra for the optimum emission under various excitations. We noted that the color of the combined emission was warm white. Under X-ray and UV excitation, the CCT was 3103 K and 4065 K, which are quite near to the typical blackbody locus points of 3142 K and 4065 K. Doping with a single Dy^{3+} -ion and co-doping with other rare earths resulted in the color temperatures predicted by earlier studies. During photoluminescence studies, the Y/B emission ratio was predicted to be 1, which should result in a bluish hue of white light. Evidently, the emission maxima in the red (680 nm) and far-red (765 nm) area pulled the CIE 1931 coordinates into the warm zone; nevertheless, this tendency contradicts the rise in energy of the excitation sources.

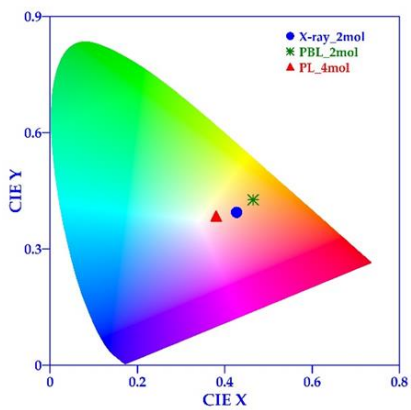

Fig. 5. The CIE 1931 chromaticity plot for the samples having optimized concentration under X-ray, proton beam, and UV excitation.

The cross-relaxation quenching mechanism via CRC-1 was found to be defunct (absorbance and emission spectra overlapped throughout wavenumbers), allowing for more intense emission in the far-red region (765 nm). The CIE 1931 coordinates and corresponding color temperature for the emission spectra under X-ray, proton beam, and UV excitation for all doped samples emerged in the warm white area, indicating the use of phosphors for warm wLEDs. Incorporating Dy^{3+} -doped $Li_3Sc(BO_3)_2$ phosphors into wLEDs has potential uses in workplaces or homes needing natural warm white light (CCT: 4000 K) that can be produced under UV (350 nm) stimulation. However, Dy^{3+}-doped $Li_3Sc(BO_3)_2$ phosphors may also be employed as X-ray and neutron imaging scintillators, but longer-wavelength cameras are more sensitive.

The published article can provide in-depth explanation of each experiment, can be found as,

S. Saha, H.J. Kim, A. Khan, J. Cho, S. Kang, A. V. Ntarisa, *Synthesis and luminescence studies of Dy^{3+} doped $Li_3Sc(BO_3)_2$ polycrystalline powder for warm white light*, Ceram. Int. 48 (2022) 10667–10676. https://doi.org/10.1016/j.ceramint.2021.12.281

Appendix-V: Synthesis and Elemental Analysis of Gadolinium Halides (GdX_3) in Glass Matrix for Radiation Detection Applications

Introduction

Glasses for radiation detection and scintillation applications in nuclear and high-energy physics research piqued the interest of several scientists. Gadolinium (Gd) compounds are commonly utilized to satisfy the criteria of density and luminescence enhancement. Gd halides (GdX_3) are hygroscopic salts that can serve as good sensitizers in a glass network to enhance the luminescence of an activator (Ce). To verify the elemental abundance of elements in glass samples after combustion at high temperatures, EDX reports at both the intermediate and end phases of the glass samples might be helpful. GdF_3 and $GdBr_3$ are both rare-earth salts, but their crystalline structure growth condition, melting temperature, and solubility are extremely pH-dependent. During combustion, regardless of whether the atmosphere is controlled (inert or acidic) or not (air), a rise in gaseous pressure may be observed for each GdX_3 (X = Cl, Br, I) above the melting temperature. For such chemical transport events, the change in Gibb's free energy is either negative or positive by a tiny margin, defining the chemical dissolution process as either spontaneously occurring or feasible owing to a temperature increase in the surrounding environment. The system is expressed as an equation (1),

$$G_T = \Delta H_T - T\Delta S \,, \tag{1}$$

where G_T and ΔH_T are the changes in Gibb's free energy and enthalpy, respectively, of the system at temperature T, and ΔS is the change in entropy at that temperature. Monitoring the complete thermodynamic process that occurs during the melting of glass precursors is challenging and is typically disregarded. As previously documented, the melting of batch glass precursors at high temperature (1400~1500 °C) can begin the gaseous state of $GdBr_3$ due to its boiling point of 1455 °C. Another necessity is to remodel the Si-O bonds in the glass network, which will impact the release of Br_2 as a gas. Observing and analyzing an increase in vapor pressure within the furnace chamber may thus be of interest.

In light of these factors, energy dispersive X-ray (EDX) analysis can be both informative and practical for identifying the component parts of samples of manufactured glass. The data is required to comprehend the glass network, which may then be studied further for change and improvement. EDX is an analytical technique for finding the characteristic X-ray energy emitted by an element when activated by a powerful electron beam. The characteristic X-ray energy released is classed as Kα, Kβ, Lα, Lβ, etc., based on the shell hole location (e.g., K, L, etc.) formed by the incident energetic electron and to be filled by the outer shell electron (e.g., L, M, etc.). Spectroscopy is utilized to ascertain the X-ray energy released. However, the EDX method cannot identify light elements (H, He, Li and Be).

In this experiment, two phosphate-based glass networks were produced, using P_2O_5 as the glass former and Al_2O_3 as the glass intermediate, GdX_3/Gd_2O_3 and $CeBr_3$ as the sensitizer and luminescence activator, and Li_2O (as Li_2CO_3) and CaO (as $CaCO_3$) as the glass modifiers, respectively. Traditionally, the structure of phosphate glasses has been described using the same nomenclature as silicates, which takes into account the quantity of bridging oxygen per tetrahedron and provides the basis for the Q^n (n = 3, 2, 1, 0) terminology. Compounds of GdX_3 (X = F, Cl, Br, I) and Gd_2O_3 were added at the same molar ratio in order to compare the presence of halides in the glass network after quenching. Gd is a well-known

element that, through efficient energy transfer, sensitizes the network and enhances the luminescence of Ce^{3+} ions. EDX analysis and scanning electron microscopy (SEM) pictures were used to examine powdered glass samples that had been manufactured. Under X-ray excitation, the luminescence, transmittance, and scintillation characteristics of the manufactured glass samples were evaluated, as well as under -particle excitation from a ^{241}Am source.

Glass samples were manufactured with a chemical composition of $62P_2O_5{:}20Li_2CO_3{:}10X{:}5Al_2O_3{:}3CeBr_3$, where X represents different gadolinium (Gd) compounds (Gd_2O_3, GdF_3, $GdCl_3$, $GdBr_3$ and GdI3). The glasses are designated PLACbGdO, PLACbGdF, PLACbGdCl, PLACbGdBr, and PLACbGdI, depending on the component Gd compounds as indicated in Table 1 with respective concentrations in mol as well as the optical images in Fig. 1. Later, two further glass samples were created using the formula $(46\text{-}X)P_2O_5{:}35Li_2CO_3{:}9GdI_3{:}5CaCO_3{:}5Al_2O_3{:}XCeBr_3$ (where X = 1, 2), indicated as $PLCaGdACe_1$ and $PLCaGdACe_2$, depending on the quantity of $CeBr_3$.

Table 1: The prepared PLACbGd glass series composition, reported in mol. %

Glass label	**P_2O_5**	**Li_2CO_3**	**10 X**	**Al_2O_3**	**$CeBr_3$**
PLACbGdO	62	20	Gd_2O_3	5	3
PLACbGdF	62	20	GdF_3	5	3
PLACbGdCl	62	20	$GdCl_3$	5	3
PLACbGdBr	62	20	$GdBr_3$	5	3
PLACbGdI	62	20	GdI_3	5	3

X = Different Gd compounds.

(a) (b) (c) (d) (e)

Fig. 1. The photographs of fabricated glasses as (a) PLACbGdO, (b) PLACbGdF, (c) PLACbGdCl, (d) PLACbGdBr, (e) PLACbGdI.

Results and Discussion

FE-SEM and Energy Dispersive Spectroscopy (EDX)

Fig. 2. (a. I), (b. I), (c. I), (d. I), and (e. I) display the SEM images and their corresponding EDX spectra in Fig. 2. (a. II), (b. II), (c. II), (d. II), and (e. II) of glasses PLACbGdO, PLACbGdF, PLACbGdCl, PLACbGdBr, and PLACbGdI, respectively, The SEM photos depict the surface morphology as an interim phase before to total

melting or as a result. It may be thought of as an irregular cluster of compounds that are traveling through the dissolving process. No grains or domains are displayed.

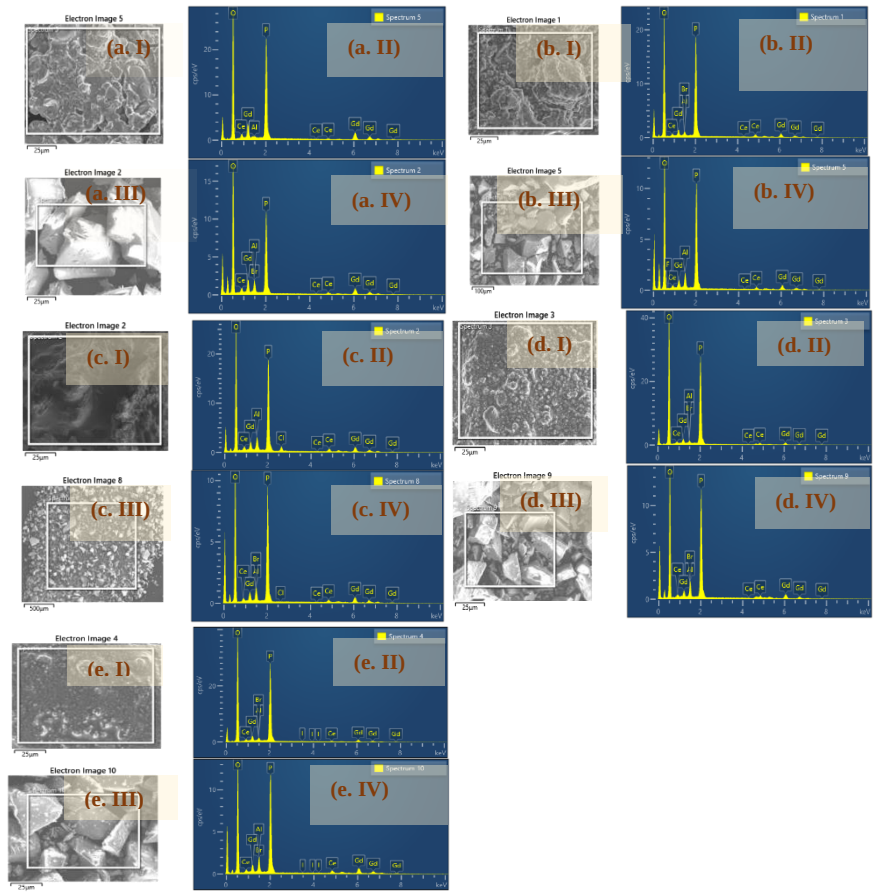

Fig. 2. The FE-SEM micrographs and their corresponding EDX spectroscopy plots, where (a. I), (b. I), (c. I), (d. I) and (e. I) are micrographs after heat treated at 325 °C along with (a. II), (b. II), (c. II), (d. II) and (e. II) showing their corresponding EDX plots, (a. III), (b. III), (c. III), (d. III) and (e. III) are micrographs of grinded glasses, melted at 1300 °C along with (a. IV), (b. IV), (c. IV), (d. IV) and (e. IV) showing their corresponding EDX plots. The depicted (a. I, II, III, IV), (b. I, II, III, IV), (c. I, II, III, IV), (d. I, II, III, IV), (e. I, II, III, IV), were obtained from PLACbGdO, PLACbGdF, PLACbGdCl, PLACbGdBr, and PLACbGdI samples, respectively.

Fig. 2 (a. III), (b. III), (c. III), (d. III), and (e. III) depicts the acquired SEM images and respective EDX plots in Fig. 2 (a. IV), (b. IV), (c. IV), (d. IV), and (e. IV) of thermally quenched, annealed, and grounded content of glasses PLACbGdO, PLACbGdF, PLACbGdCl, PLACbGdBr, and PLACbGdI, respectively, after melting at 1300 °C. The SEM images indicate a spectrum of micrometer-sized particles with no discernible crystallization pattern, suggesting the amorphous nature of the

materials. As a result of grinding glass samples into a powder, while microscopic particles were discovered.

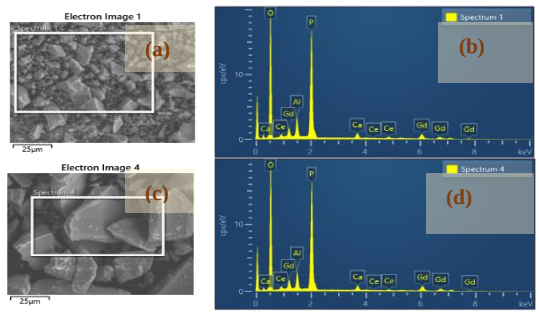

Fig. 3. (a) The FE-SEM micrograph and (b) the corresponding EDX spectroscopy plot of $PLCaGdACe_1$ sample after grinding, (c) The FE-SEM micrograph and (d) the corresponding EDX spectroscopy plot of $PLCaGdACe_2$ sample after grinding.

Fig. 3 (a) and (b) show a $PLCaGdACe_1$ glass sample's SEM micrograph and EDX spectrum, while Fig. 3 (c) and (d) show the same for $PLCaGdACe_2$. $PLCaGdACe_1$ glass has smaller particles than $PLCaGdACe_2$. EDX spectra show the atomic centration of components in produced glass compositions, see Table 2. Original elemental compositions are compared to heat-treated samples and glass powders. Technological restrictions prevented comparing Li content. The C sample base was disregarded to prevent misunderstanding. As shown, samples lack halide elements. Instead, O content rose, which may be explained by the environment's need to join glass network parts. Al content dropped during heat treatment but rose in the resulting glass sample, indicating alumina crucible participation during melting. Gd, Ce, and P contents are presumed unaltered throughout the process.

Table 3 details the obtained elemental composition for $PLCaGdACe_1$ and $PLCaGdACe_2$ samples. A similar pattern may be found here as well. I was completely absent from the composition. As Ce doping concentration increased, EDX trace content is also found to be increased. The next section describes the potential dissolving processes of rare-earth halogen salts in such a glass matrix.

Table 2: The atomic concentration (%) of elements of PLACbGd series at the initial condition, after heat treated at 325 °C, and after being glass

Elements	**PLACbGdO**			**PLACbGdF**			**PLACbGdCl**			**PLACbGdBr**			**PLACbGdI**		
	Initial	Heat treated	glass	Initial	Heat treated	glass	Initial	Heat treated	glass	Initial	Heat treated	glass	Initial	Heat treated	glass
Li	6.26	-	**-**	6.33	-	**-**	5.48	-	**-**	6.35	-	**-**	6.32	-	**-**
C	3.11	-	**-**	3.18	-	**-**	3.67	-	**-**	3.17	--	**-**	3.17	-	**-**
O	64.73	73.60	**78.05**	61.00	74.44	**77.75**	60.92	72.63	**77.18**	61.00	77.89	**77.77**	60.96	77.27	**76.36**
Al	1.57	0.24	**2.61**	1.59	0.78	**2.42**	1.58	2.58	**2.46**	1.59	0.56	**2.60**	1.58	0.64	**2.72**
Gd	3.12	4.29	**2.76**	1.59	2.03	**1.84**	1.58	2.76	**1.87**	1.58	1.29	**1.89**	1.62	1.51	**2.09**
Ce	0.46	0.23	**0.55**	0.48	0.92	**0.66**	0.47	1.18	**0.62**	0.48	0.42	**0.59**	0.48	0.33	**0.69**
Br	1.41	0	**0**	1.43	0	**0**	1.42	0	**0**	6.18	0	**0**	1.42	0	**0**
P	19.34	21.83	**16.03**	19.66	21.84	**17.33**	19.62	19.84	**17.87**	19.65	19.84	**17.15**	19.63	20.25	**18.14**
F	-	-	**-**	4.75	0	**0**	-	-	**-**	-	-	**-**	-	-	**-**
Cl	-	-	**-**	-	-	**-**	5.29	1.02	**0**	-	-	**-**	-	-	**-**
I	-	-	**-**	-	-	**-**	-	-	**-**	-	-	**-**	4.86	0	**0**
Total	100 %	100%	100%	100 %	100%	100%	100 %	100%	100%	100 %	100%	100%	100 %	100%	100%
O/P	3.35	3.37	**4.86**	3.10	3.41	**4.49**	3.10	3.66	**4.29**	3.10	3.93	**4.53**	3.11	3.82	**4.21**

Table 3: The atomic concentration (%) of elements in two glass samples of PLCaGdACe series

Elements	$PLCaGdACe_1$	$PLCaGdACe_2$
O	71.28	71.26
Al	3.64	3.31
P	20.83	20.93
Ca	1.22	1.15
Ce	0.55	0.86
Gd	2.48	2.49
Total	100	100
O/P ratio	3.42	3.40

Halide Dissolution

Rare earth halides are known to be hygroscopic that confirms the nature of absorbing moisture from their environment. Unless provided in a fully dry glove box, the substances will remain hydrated. Numerous studies have been undertaken on the nature of halide compounds. Each chemical component keeps its crystalline structure prior to the formation of a glass matrix. However, the dissolving properties of these halides are equivalent to $REX_3.nH_2O$, where n can range between 1 and 9 depending on the solubility of the individual halide molecule. Due to the concentration of water molecules, it is possible to represent the dissolving process as the equation (2)

$$REX_3 + H_2O \rightarrow REOX + 2HX \quad (2)$$

With oxygen (O) from air present during high-temperature combustion, the process can be represented by the equation (3)

$$2REX_3 + O_2 \rightarrow 2REOX + 2X_2 \quad (3)$$

At the combustion temperature condition, rare-earth halides generate either rare-earth oxyhalides dissociation halides or acidic hydrogen halides, both of which are gaseous. Solubility can also be stated as a function of temperature so long as the pH level is maintained precisely. Moisture debris increases when pH rises, but decreases when acidic gases, HX, are present.

The rationale for this finding is the magnitude of the lattice energy and Gibb's free energy, both of which decrease as the size of anions and bond-distances grow. The trend grows with the inclination of covalent bonding, which may also be observed in the melting and boiling temperatures of other rare-earth halides. In the meanwhile, it is important to consider the enthalpy required to create rare-earth cations (e.g., Gd^{3+}, Ce^{3+}, etc.). Mostafa et al. (1995) determined the heat and free energy necessary to generate trivalent rare-earth cations at 298

K using the group contribution method. Sergio et al. (2021) utilized this data to establish a linear relationship that illustrates the enthalpy requirements for the formation of RE_2O_3 from REX_3 and REOX. The ramifications of hydrolyzing rare-earth salts (REX_3 or REOX) to produce their basic oxides are consistent throughout all of these projections and studies. Electrochemical smelting at high temperatures permits the reduction of rare-earth halides or metal halides, therefore separating rare-earth metals or metals from halide ions.

Formation of Phosphate Structure

In addition to the hygroscopicity of rare earth halides, alkali metal compounds such as Li_2CO_3 and CaO undergo chemical reformations at high temperatures during melting. In the composition of glass, the electropositive metal compounds (Li, Ca, Al, Gd, etc.) are melted and ionized. The literature describes the breakdown of Li_2CO_3 by ionization in the presence of HX as the equation (4),

$$Li_2CO_3 \rightarrow 2Li^+ + 2e^- + \frac{1}{2}O_2 + CO_2 \uparrow \quad (4)$$

A thermogravimetric analysis (Tg) curve was published in a recent publication (Pabitra et al. 2021) on comparable glass compositions of PLACbGd series. At around 700 °C, which is the estimated melting point of Li_2CO_3 and other REX_3 (rare earth halides) present in the batch composition, the graph indicated the commencement of a comprehensive breakdown. The procedures reveal the ionization of Li following the melting of Li_2CO_3, which participates in subsequent chemical and solid-state reactions. Consequently, the metals are positively ionized in the presence of oxygen during high-temperature (1300 °C) combustion, releasing the halides as gaseous while leaving the positively ionized metals to undergo oxidation.

However, polymeric forms of P_4O_{10} (P_2O_5) hydrolyze quickly to produce H_3PO_4, which explains the extremely high dissolving or hydrating tendency of the phosphate network. Pentavalent (V) phosphorus (P) compounds are stable against oxidation state +3. The well-known Q^3 structure of phosphate glass is a four-fold coordination arrangement between P and oxygen. The amount of solubility of the glass intermediate, Al_2O_3, which was employed in the current batch composition, depends on the ratio of P_2O_5 concentration. The Q^3 structured phosphate network is often compromised to Q^2, Q^1, and even Q^0 in the presence of the glass intermediate (Al_2O_3) and glass modifier (Li_2O), depending on its electronegativity states to the electropositive Al^{3+}, Li^+, or Ca^{2+}. The P-O-P bonds separate once the modifier oxides (Li_2O, CaO, etc.) are added to the P_2O_5 network, creating negatively charged single bonded oxygens ($P\text{-}O^-$), whose charges are counterbalanced by the modifier cations. By modifying P-O-P bonds to generate Me-O-P bonds, the network becomes more stable and can fend against depolymerization. According to the magnitude of the O/P ratio, the vitreous phosphate compositions may be divided into three categories: ultraphosphates (<3), polyphosphates (>3), and metaphosphates ($= 3$). The categorization indicates that our manufactured glasses belong to the polyphosphate group based on the O/P ratio shown in Tables 2 and 3. Additionally, it was found that the PLCaGdACe glass series had lower O concentrations than the PLACbGd glass series. The amount of NBOs is expected to rise as a result of the high concentration of electropositive components like Li and Ca.

X-ray Induced Luminescence

The PLACbGd glass series' and PLCaGdACe$_2$'s X-ray induced luminescence (XRL) spectra were captured at room temperature and are shown in Fig. 4. The collected spectra revealed broad emission bands between 300 and 400 nm, which points to a 5d-4f transition brought on by Ce^{3+} -ion activation. The PLACbGdI sample, which had the greatest peak intensity in the PLACbGd glass series and was second to the PLCaGdACe2 sample in terms of peak intensity. The peak positions in the depicted spectra show a little redshift. Such a propensity might be attributed to optical basicity (O/P ratio). Another explanation is the impact of the glass samples' transmittance, which is covered in Section 3.5.

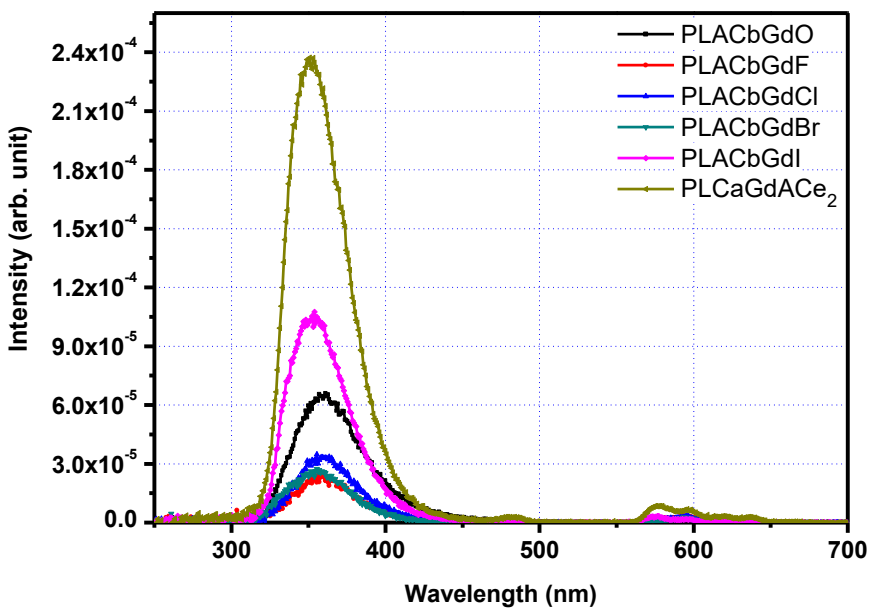

Fig. 4. X-ray induced luminescence spectra of PLACbGd glass series and PLCaGdACe$_2$ glass sample.

Transmittance Measurements

Photons generated inside the sample should be able to cross its thickness under the excitation of radiation and reach the detector. The absorption of each sample differs based on the glass network and dopants employed. Transmittance begins to rise when sample absorption for the target wavelength gets closer to zero. This rising nature is reliant on the environment, and the ideal value changes greatly depending on the level of surface polishing. According to what we previously found in a similar network, the absorption spectrum and the emission spectrum might overlap. The Stokes shift phenomenon has direct implications for the repercussions. The transmittance value is influenced by reflectance and optical scattering in addition to the standard absorption properties. If we assume that the total is equal to 1, we can say that reducing the other parameters will give a rise in the region of luminous photon wavelength. Thus, a sample's optical quality and amount of self-absorption are indicated by

the transmittance value. Transmittance spectrum and X-ray-generated emission were compared, and Fig. 5 (a-f) shows the result. A lower transmittance value may have an adverse influence on the emission intensity with a slight change to the peak location.

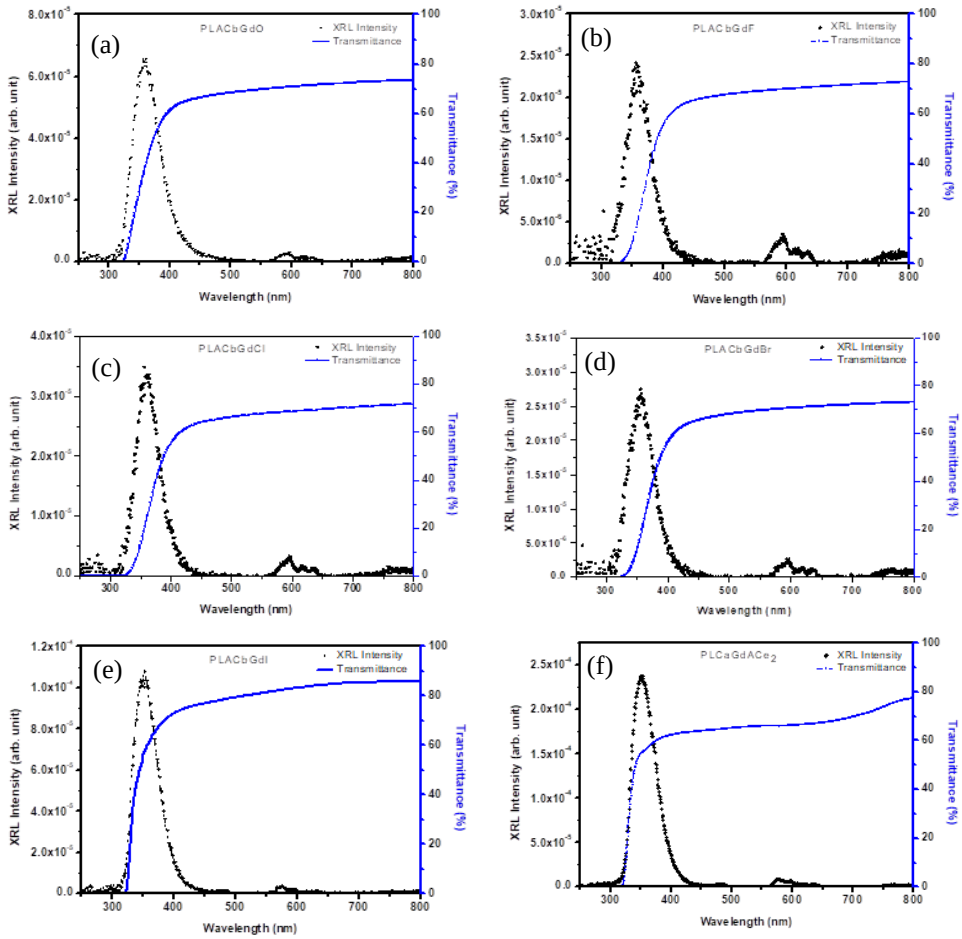

Fig. 5. The transmittance spectra in comparison to XRL are plotted for samples (a) PLACbGdO, (b) PLACbGdF, (c) PLACbGdCl, (d) PLACbGdBr, (e) PLACbGdI, and (f) $PLCaGdACe_2$.

Scintillation Properties

Using a 5.5 MeV α -particle excitation from a ^{241}Am source, the scintillation properties of produced glass samples were studied. However, as shown in Fig. 6. (a) and (b), a clear α -peak was discovered in the pulse height spectra of PLACbGdI and $PLCaGdACe_2$ glass samples. PLACbGdI and $PLCaGdACe_2$ glass samples yielded energy resolution (ER) values of 29% and 31%, respectively.

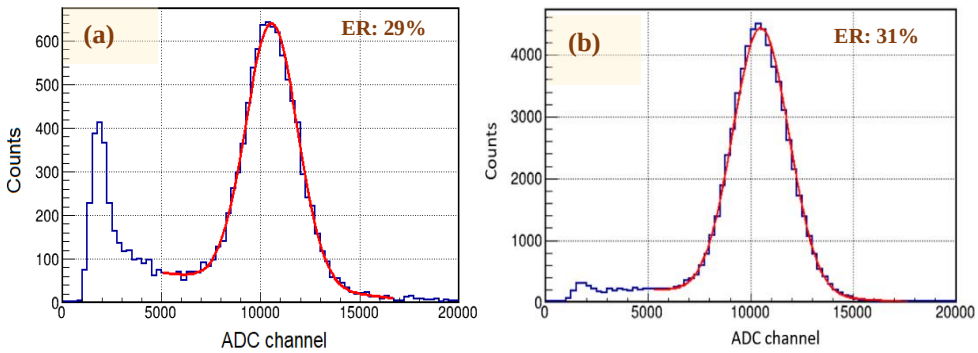

Fig. 6. Pulse height spectrum identifying α -peak under ^{241}Am radiation source obtained from (a) PLACbGdI and (b) PLCaGdACe$_2$ glass samples.

Two different combinations of Gd compounds, including halides and oxides, with equivalent beginning concentrations were used to create glass samples using the traditional melt quenching method in an airy atmosphere. We assessed the FE-SEM images and the accompanying EDX information. The EDX findings showed that no halides were found in the samples of manufactured glass. This potential under some conditions is also supported by earlier studies on the rare-earth halide dissolving process. In comparison to the other batches, the changed batch composition with a high percentage of glass modifiers had a stronger XRL peak. It was demonstrated that the transmittance spectrum had a substantial impact on where and how intense the XRL peak was. For the PLACbGdO, PLACbGdF, PLACbGdCl, PLACbGdBr, PLACbGdI, and PLCaGdACe2 samples, the transmittance values at the XRL peak sites were determined to be 37%, 12%, 19%, 16%, 58%, and 55%, respectively. Only PLACbGdI and PLCaGdACe$_2$ samples could clearly distinguish a α -peak during scintillation measurements. Such results might be explained by either a very low transmittance value or considerable self-absorption. For the PLACbGdI and PLCaGdACe$_2$ samples, three scintillation decay components were captured during α -excitation. Another study that may be carried out is the systematic measuring of EDX and transmittance after the production of glasses in a controlled environment in order to ascertain the effect on luminescence and scintillation qualities. The full report was published as,

Sudipta Saha, Amos V. Ntarisa, Nguyen Duy Quang, H.J. Kim, S. Kothan, J. Kaewkhao, *Synthesis and Elemental Analysis of Gadolinium Halides (GdX_3) in Glass Matrix for Radiation Detection Applications*, Opt. Mater. (Amst). 129 (2022) 112490. https://doi.org/10.1016/j.optmat.2022.112490.

Appendix-VI: Scintillation Performance of the Ce^{3+} - Activated Lithium Phosphate Glass

Introduction

For decades, scientists have studied glass scintillators for nuclear detection applications, such as ^{6}Li-based scintillating glass for neutron detection, scintillating glass fibers for tracking detectors, large-scale, and low-cost detectors for radiation monitoring systems, etc. Until date, glass networks have been reported to be composed of silicate, borosilicate, borates, tellurite, germinate, and phosphate, as well as combinations of these and other substances. Among all of them, silicate (SiO_2)-based glasses have been most frequently utilized to define and deploy glass scintillators for radiation detection. These compositions of scintillation glass had an enough amount of Gadolinium (Gd) to successfully absorb gamma rays. A high Gd concentration enhances the density of the compound and accelerates the migration of electronic excitations via the Gd subsystem, which acts as a reservoir for metastable carriers and transports them to emission sites such as Ce^{3+} ions.

To fulfill the requirements of a scintillating material, the Gd-Ce concentration was changed in an effort to discover the optimal combination that can absorb full energy from γ-rays and α-particles before producing a broadband emission of short wavelength and short lifespan. Thermal analysis, optical characteristics, luminescence, and scintillation properties were utilized to characterize the synthesized glasses. The absolute light yield and energy resolution (ER) of one of the synthetic glass samples were determined to be 1600 ± 200 Photons/MeV and 31%, respectively, when stimulated with a 662 keV γ-ray from a ^{137}Cs source. The optical images of polished glasses and the batch glass compositions were estimated in molar ratio and displayed with observed density (±standard deviation) and refractive index (±standard deviation) in Table 1.

G-1 G-2 G-3 G-4 G-5

Fig. 1. The photographic images of optically polished glasses.

Table 1: The given code name of each glass composition, the concentration of constituent compounds, the dimension of the polished glasses, density, and refractive index are listed.

Sample	Li_2CO_3	P_2O_5	GdI_3	Al_2O_3	$CaCO_3$	$CeBr_3$	Dimension (mm^3)	Density (g/cm^3)	Refractive Index
	(mol%)								
G-1	35	45	9	5	5	1	8.5×7.5×2.5	2.9058 ±0.0027	1.5662 ±0.0002
G-2	35	45	8	5	5	2	8.7×8.5×2.7	2.8521 ±0.0122	1.5605 ±0.0002
G-3	35	44	9	5	5	2	8.5×8.0×2.7	2.8717 ±0.0081	1.5595 ±0.0002
G-4	35	45	7	5	5	3	8.6×6.4×2.9	2.8483 ±0.0027	1.5609 ±0.0002
G-5	35	45	5	5	5	5	8.7×7.5×2.7	-	-

Result and Discussion

DSC-TGA Analysis

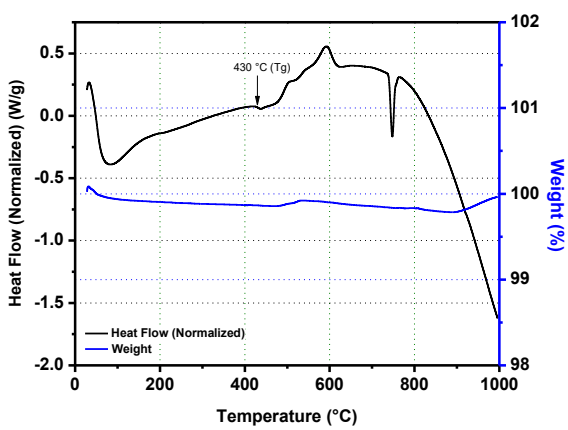

Fig. 2. The DSC (black line) and TGA (blue line) analysis spectra were plotted to identify the Tg and other thermal properties varying the temperature until 1000 °C.

The differential scanning calorimetry (DSC) and thermogravimetric analysis (TGA) spectra depicted in Fig. 2 suggest that the desorption of the chemicals began as an endothermic process at room temperature and proceeded until 83 °C, which may correspond with the evaporation moisture content. This can be induced by a few chemicals that are hygroscopic at ambient temperature and are found in the composition of glass. After an exothermic climb to

430 °C, a rapid dip shows that the molecule may have softened. Thus, 430 °C is regarded the glass transition temperature (Tg) for the studied glasses. The TGA (blue) curve indicates that until 1000 °C, there is no substantial weight loss during the process.

FE-SEM and EDX Analysis

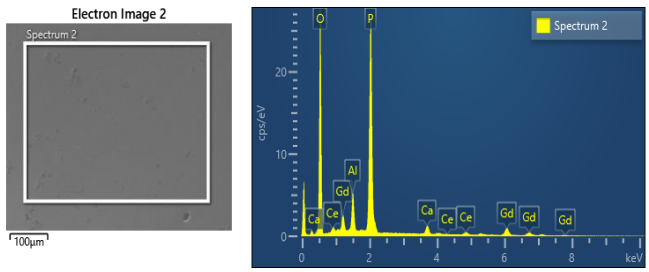

Fig. 3. (a) The FE-SEM image and (b) the corresponding EDX plot of G-1 glass sample surface.

Fig. 3 (a) and (b) depict, respectively, the FE-SEM picture and related EDX spectrum obtained from the G-1 glass sample. The SEM image displays the almost homogeneous surface morphology (8.5 × 7.5 mm^2) of the glass sample. There are a few microscopic black spots on this surface, which may have been formed by the freezing of the hot melt. In Table 2, the original elemental compositions are compared with the elemental compositions of a created glass sample, along with an estimate of the uncertainty. Li is excluded from quantitative and comparative analysis due to its low atomic number and insufficient distinctive X-ray emission, which cannot be efficiently identified by the EDX equipment. Despite the presence of carbon in the early compounds, the expected dissolving process allows CO_2 to evaporate, leaving Li_2O and CaO at the melting point of 1300 °C for the combined precursors. As can be seen, the Al content of the final glass material rose. During high-temperature melting, the most likely reason is the leaching of Al from the used crucible, which is composed of Al_2O_3. The remaining material remains unaltered.

Table 2. Elemental abundance of constituent elements at atomic % in the glass matrix at the initial and final stages of glass sample G-1.

Element	Initial (At. %)	Glass (At. %)
O	70.89 ± 0.01	71.15 ± 3.56
P	22.78 ± 0.01	21.20 ± 1.06
Al	2.54 ± 0.01	3.72 ± 0.19
Gd	2.27 ± 0.01	2.33 ± 0.12
Ca	1.26 ± 0.01	1.25 ± 0.06
Ce	0.26 ± 0.01	0.35 ± 0.02

Luminescence

X-ray Induced Luminescence

The X-ray-induced luminescence (XRL) of all glass samples is depicted in Figure 4. With increasing Ce^{3+} doping concentration, a continuous peak shift toward a longer

wavelength may be detected. The discovered peak locations for G-1, G-2, G-3, G-4, and G-5 glass samples are 347 nm, 349 nm, 350 nm, 356 nm, and 368 nm, respectively. A rise in Ce^{3+} concentration may result in a shift in the optical bandgap, which may account for a previously reported trend. The G-1 sample, which included 9 mol% GdI_3 and 1 mol. percent $CeBr_3$, exhibited the peak with the maximum intensity. Even while sample G-3 had the same quantity of GdI_3, the Ce^{3+} doping concentration was 2%, resulting in a peak emission intensity that was less intense. This potential is referred to as Ce^{3+} concentration quenching. Emission peak intensities of other samples are seen to decrease when the concentration of GdI_3 decreases.

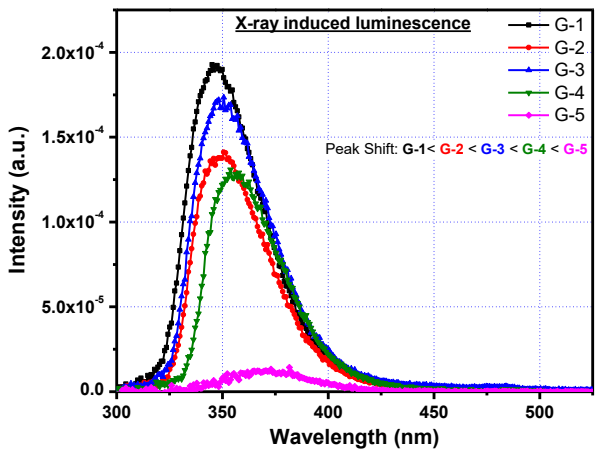

Fig. 4. The X-ray-induced luminescence spectra were obtained for all glass samples for intensity and peak position comparison.

Photoluminescence

As seen in Fig. 5, the excitation spectrum was produced for the G-1 sample by considering 350 nm as the Ce^{3+} characteristic emission due to its 5d-4f transition (green line). A wide excitation band encompassing the 4f electronic energy levels of Gd^{3+} ions (as $^6D_{9/2}$ at 252 nm, ^6I_J between 274 and 278 nm, and ^6P_J between 299 and 310 nm) and the 5d energy band of Ce^{3+} ions at 308 nm was discovered in the spectra. Photoluminescence (PL) emission spectra were obtained for the glass sample under UV excitations at 272 nm and 308 nm corresponding to Gd^{3+} and Ce^{3+} excitations, as shown in Fig. 5 (blue and red lines, respectively). The location of the emission peak coincides with the XRL peak, as seen in Fig. 4. A similarly wide emission seen during both Gd^{3+} and Ce^{3+} excitations that indicates a clear energy transfer from the 4f energy levels of Gd^{3+} to the 5d energy band of Ce^{3+} ions. As seen in Figure 5, the transmittance spectrum was produced for the same sample in the UV-Vis range from 200 nm to 900 nm and compared to the emission spectra. There was no transmission until 323 nm, after which the value was increased to 50% while the emission spectra overlapped at 336 nm. At the highest emission wavelength (347 nm), the transmittance value is 72%. The value was raised until it reached 85% in the region of longer wavelengths. Even if a portion of the produced photons may be absorbed due to self-absorption and poor transmittance, the transmittance value is sufficient for the sample to be used in scintillation applications.

To clearly illustrate the energy transfer mechanism from the Gd^{3+} subsystem to the Ce^{3+} subsystem, excitation and emission spectra from both relevant subsystems were necessary. During PL research in the UV-Vis region, the excitation and emission spectra for both immediate (Fluorescence) and delayed (Phosphorescence) mood scans were obtained for the G-1 glass sample, as shown in Fig. 6. The phosphorescence scan pinpointed the excitation peaks caused by the 4f-4f transitions of Gd^{3+} ions in the glass network as 246 nm ($^8S_{7/2} \rightarrow {}^6D_{1/2}$), 252 nm ($^8S_{7/2} \rightarrow {}^6D_{9/2}$), 273 nm ($^8S_{7/2} \rightarrow {}^6I_{11/2}$, $^6I_{13/2}$, $^6I_{15/2}$), and 278 nm ($^8S_{7/2} \rightarrow {}^6I_{7/2}$). Another excitation peak at 311 nm was detected as a peak in the emission spectrum (violet color) recorded in phosphorescence mood scan under UV excitation at 273 nm ($8S_{7/2}$ ^6I_J), related to Gd^{3+} ions. This suggests that photons released by the transition of Gd^{3+} ions from the $^6P_{1/2}$ state to the $^8S_{7/2}$ state contributed to the broad-band emission of the Ce^{3+} characteristics 5d-4f transition (Fig. 5 (Blue line) and Fig. 6 (Violet line)).

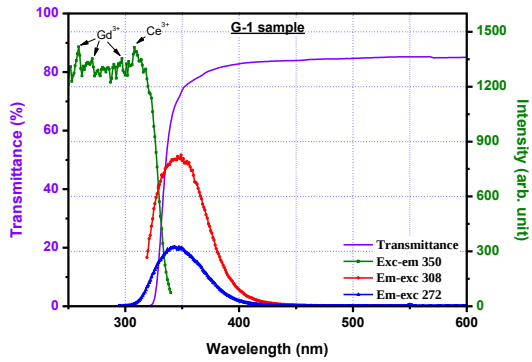

Fig. 5. The photoluminescence excitation and emission in comparison with transmittance spectra obtained from the sample G-1.

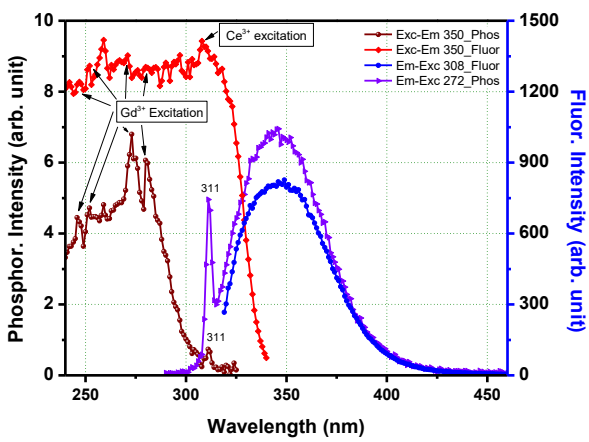

Fig. 6. The prompt (Fluorescence) and delayed (Phosphorescence) photoluminescence excitation and emission spectra obtained from the sample G-1 that are showing a separated excitation peak of Gd^{3+} and Ce^{3+} -ions.

Fig. 7 depicts a schematic partial level diagram of charge transfer, excitation, and emission mechanisms providing a comprehensive description of the electronic transitions in the manufactured G-1 glass sample.

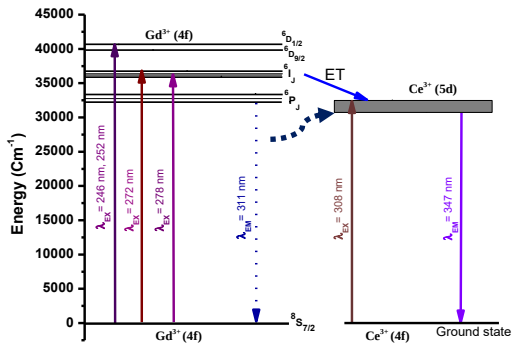

Fig. 7. The schematic partial energy level diagram presenting the possible energy transfer process from Gd^{3+} to Ce^{3+} ions inside the G-1 glass sample.

The PL emission fluorescence of all produced glass samples was plotted and compared in Fig. 8. As seen in Fig. 4 for the XRL research, the G-1 sample exhibited the most intense emission. The shift in intensity followed the same trend and may be expressed as G-1, G-3, G-2, G-4, and G-5 in descending order. Consideration was given to characterizing the scintillation properties of sample G-1 of glass, which was deemed superior to other tested samples.

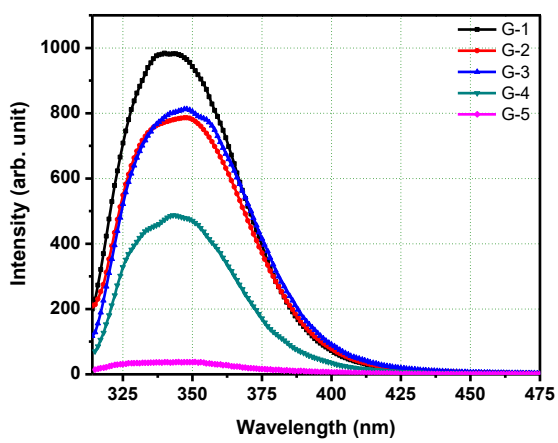

Fig. 8. The photoluminescence spectra were obtained under 308 nm excitation for all glass samples for comparison

Lifetime Measurement

UV Excited lifetime

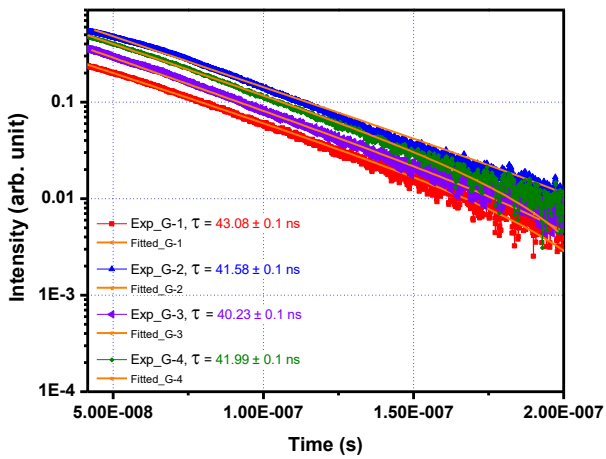

Fig. 9. The projected decay profiles were measured under 266 nm pulsed laser excitation and fitted with a single component exponential decay function.

As shown in Fig. 9, the UV-excited luminous lifetime of the glass samples (G-1, 2, 3, 4) was evaluated using a pulsed laser (266 nm) to determine the prompt lifetime. The best match for the predicted decay profiles was a single component exponential decay function as shown in Eq. 1:

$$y = Aexp^{-x/\tau} + y_0 \quad (1)$$

where y and y_0 are the intensities at periods t and 0, A is the contribution to the intensity, and is the decay time constant. The obtained decay constants for samples G-1, G-2, G-3, and G-4 are 43.08, 41.58, 40.23, and 41.99 ns with a fitting uncertainty of 0.1 ns. In agreement with the observed results, the Ce^{3+} ion experiences a 5d-4f transition, which largely contributed to the emission spectra seen in Fig. 5, 6, and 7. In terms of decay time, a number of Ce-doped luminescent materials have shown comparable findings, according to the scientific literature.

Scintillation lifetime

The scintillation lifetime of a G-1 glass sample under α -particles and γ-ray excitation from ^{241}Am and ^{137}Cs sources, respectively, was measured. The decay time projection under -particle excitation at room temperature was fitted with a three-component exponential decay function as shown in Eq. 2 and illustrated in Fig. 10. (a)

$$y = A_1exp^{-x_1/\tau_1} + A_2exp^{-x_2/\tau_2} + A_3exp^{-x_3/\tau_3}, \quad (2)$$

where y represents the intensity at time t, y_0 is constant (at t = 0), and A_1, A_2, and A_3 indicate the integrated areas of the fluorescent lifetimes τ_1, τ_2, and τ_3, accordingly. The estimated components are 32.5 ± 0.3 ns, 152.4 ± 1.5 ns, and 2.06 ± 0.3 µs with contributions of 39.4%,

16.7%, and 43.9%, respectively. Fig. 10 (b) depicts the decay profile under γ-ray excitation from a ^{137}Cs source for the identical material at room temperature. The experimental data were fitted using a three-component exponential decay function (see Eq. 2), where the components are 39.9 ± 0.4 ns, 221.7 ± 2.2 ns, and 2.29 ± 0.3 µs, with corresponding contributions of 39.4%, 16.7%, and 43.9%. Ce^{3+} -ions undergo an interconfigurational (5d-4f) transition that causes the shortest component under both excitations. The intermediate and longer components are caused by the energy transfer from the intraconfigurational (4f) states of Gd^{3+} to the 5d energy band of Ce^{3+} ions. As previously reported, a similar pattern was also seen for samples containing both Gd^{3+} and Ce^{3+} ions in a similar network.

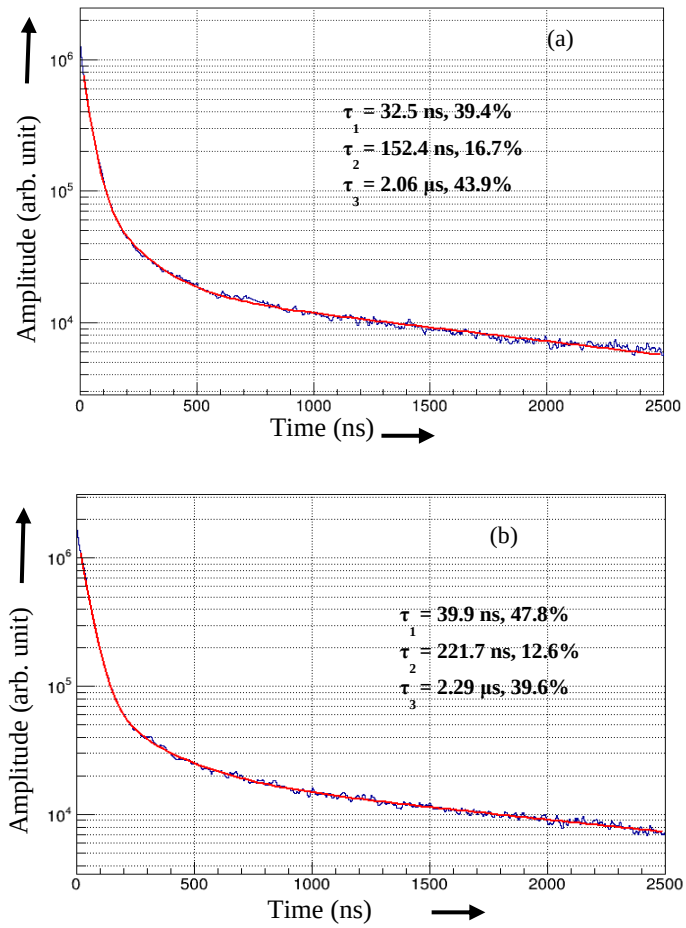

Fig. 10: Scintillation lifetime measured (a) under α -particle excitation from ^{241}Am radioactive source, and (b) under γ -ray excitation with ^{137}Cs source that shows three components exponential decay with contributions from both interconfigurational and intraconfigurational transitions.

Pulse Height Spectrum

As seen in Figure 11, the pulse height spectra for the G-1 glass sample were obtained by the excitation of α -particles with a 5.5 MeV energy from a ^{241}Am source. A

definite peak was seen as a result of the complete absorption of the full energy from the α -particles. As shown in Fig. 11, the alpha peak was fitted with a Gaussian function, and its energy resolution (FWHM) was around 22.45 %.

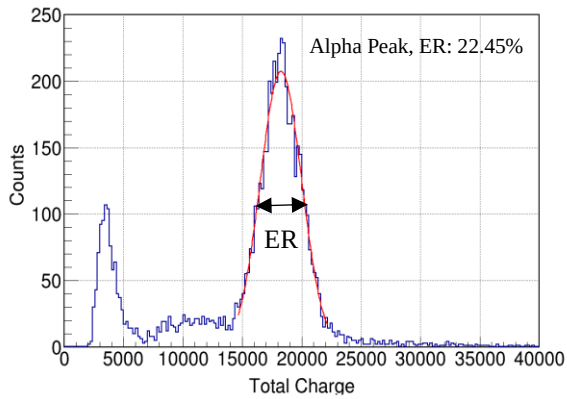

Fig. 11. The pulse height spectrum of the G-1 glass sample measured under α -particles excitation from ^{241}Am source shows a clear alpha peak with an energy resolution of 22.45%.

Fig. 12 depicts the pulse height spectrum of the G-1 glass sample acquired under 662 keV γ-ray excitation from a ^{137}Cs source. As shown in Fig. 12, the full energy absorption peak (photopeak) and Compton edge were overlay. For deconvolution, a sum of Gaussian function and a differential response function were fitted to the photopeak and Compton edge, respectively. The energy resolution was improved by 31% as a result of the photopeak's widening. The α/β ratio recorded for a sample of G-1 glass was 0.10.

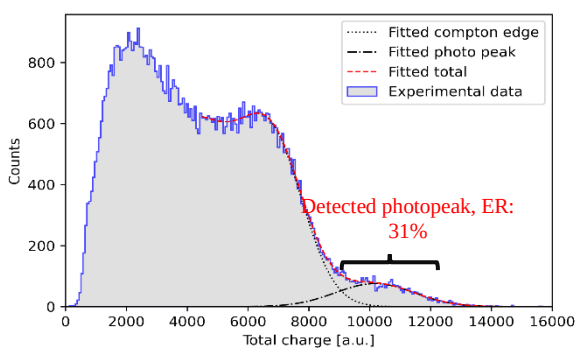

Fig. 12. The pulse height spectrum of the G-1 glass sample was measured under γ-ray excitation from ^{137}Cs source where the photopeak was separated from the Compton edge with an energy resolution of 31%.

In order to efficiently transport the absorbed energy to the emission centre (such as Ce^{3+}, Eu^{2+}, etc.) in a crystal, the network of component atoms is fairly uniform. However, the energy transmission efficiency is reduced in amorphous materials due to the absence of long-range order in the glass network. This may result in a fluctuating output of scintillation light with low energy resolution.

As we have successfully found the photopeak, it is necessary to additionally determine its light output. The scintillation light yield of the G-1 glass sample was separately evaluated using the absolute technique and compared to $Bi_4Ge_3O_{12}$ (BGO) crystal (as a standard). The approach demonstrated by J.T.M. de Haas et al. was utilized to measure the G-1 glass sample for the absolute light yield. Using Eq. 3, the absolute photon yields (Y_{ph}) were calculated.

$$Y_{ph} = Y_{pe} \frac{1-R_{eff}}{0.98 \times QE_{eff}}, \quad (3)$$

where Y_{pe} represents the photoelectron yield and R_{eff} represents the effective reflectivity of the PMT at the corresponding emission peak location. As shown in Fig. 13, the effective quantum efficiency (QE_{eff}) was calculated by averaging the X-ray induced emission spectra of the reference BGO crystal and G-1 glass sample in relation to the quantum efficiency (QE) of the Hamamatsu R6233-100 PMT at room temperature. The reflection loss was decreased by about 98% due to the 1 mm thick Teflon covering on the sample. Based on the total charge ratio of the photopeak of the sample (under γ-ray excitation) to that of the single photoelectron (SPE) response with the same PMT and voltage, the photoelectron yield was calculated. To record the single photoelectron (SPE) spectrum, the PMT was measured using only the LED generator and no other light source (dark current). As seen in Fig. 14, a single LED pulse was applied using PMT to record the SPE pulse as the reference photon peak. This number of created photoelectrons is comparable to the quantity of channels. The number of created photoelectrons (Y_{pe}) was translated to the number of photons per MeV (Y_{ph}). In addition to measuring the G-1 glass sample (see Fig. 15), the ^{137}Cs source was used to measure the BGO crystal. At 7900 Photons/MeV, the observed absolute light yield of the BGO crystal sample is consistent with prior results. 1600 ± 200 Photons/MeV were determined to be the absolute light yield of the glass sample G-1.

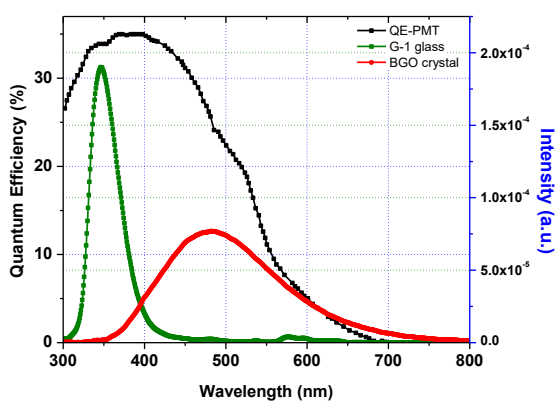

Fig. 13. Comparison of quantum efficiency (QE) spectrum of Hamamatsu R6233-100 PMT and X-ray induced emission spectra of the reference BGO crystal and G-1 glass sample.

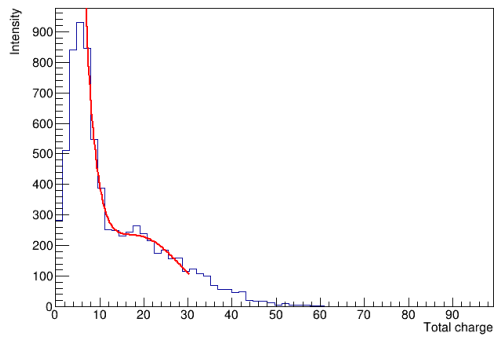

Fig. 14. Recorded (blue) and fitted (red) single-photon emission (SPE) pulse under single LED pulse with Hamamatsu R6233-100 PMT.

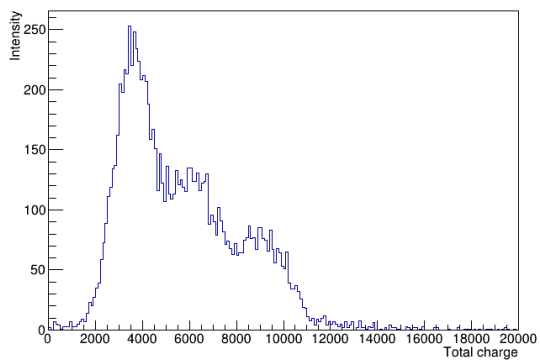

Fig. 15. Recorded pulse under γ-ray excitation from ^{137}Cs source with G-1 glass sample with the same PMT condition that was followed for SPE measurement.

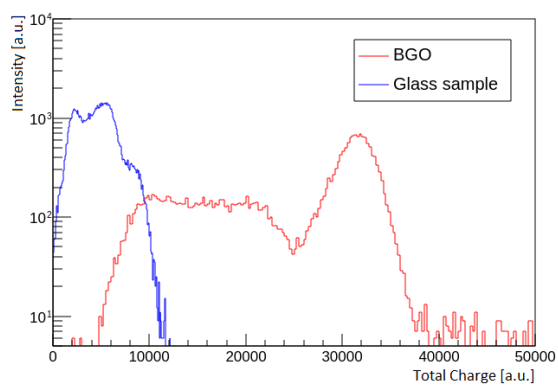

Fig. 16. The comparison in pulse height spectra to find the comparative light yield of the G-1 glass sample with reference to BGO crystal under γ-ray excitation from ^{137}Cs source.

The comparative measurement technique might be interesting to verify the value with respect to the reference BGO crystal. The comparative light yield was calculated using Eq. 4[11,101,102]:

$$Y_{ph(G-1)} = \frac{Y_{pe(G-1)} \times QE_{eff\,(BGO)}}{Y_{pe(BGO)} \times QE_{eff\,(G-1)}}\, Y_{ph(BGO)}, \quad (4)$$

where Y_{pe} represents the total charge corresponding to the complete peak absorption of each sample when excited by γ-rays. As indicated in Fig. 16, the comparative light yield ($Y_{ph(G-1)}$) of sample glass G-1 was 19% of the reference BGO crystal sample. Table 3 summarizes the computed results. The results produced from two distinct approaches are likewise in excellent agreement.

Table 3. The measured value of effective quantum efficiency (QE_{eff}), estimated value of effective reflectivity (R_{eff}), and calculated light yield (Y_{ph}) of the reference BGO crystal and G-1 glass sample.

Sample	Method	QE_{eff} (%)	R_{eff} (Estimated [117]) (%)	Light Yield (Photons/MeV)
G-1 sample	Absolute	33.6	20	1600 ± 200
	Comparative with BGO	33.6	-	1500 ± 200
BGO (ref. LY = 8000 Photons /MeV)	Absolute	20	34	7900 ± 200

The comparison of reported glass samples is displayed in Table 4. Except for our sample, all glass samples were produced in a silicate network. The discovery of a composition in a phosphate-based glass network with comparable light output and energy resolution but a shorter decay period is highly encouraging.

Table 4**.** The comparison in light yield, energy resolution, and decay time of different glass compositions.

Glass Composition (Mol%)	Light Yield (Ph/MeV)	Energy Resolution (γ-ray) (%)	Scintillation Decay Time (ns)	Reference
$50SiO_2$:$16Al_2O_3$:19NaF:$13GdBr_3$:$2CeBr_3$	1700	27	55	[118]
$33.4SiO_2$:33.3LiF:$32GdBr_3$:$1.3CeBr_3$	3460	14	522	[119]
$33.4SiO_2$:33.3LiF:$15Al_2O_3$:$2GdBr_3$:$1.3CeBr_3$	4317	15.6	~522	[119]
$63SiO_2$:21.75BaO:$13.09Gd_2O_3$:$1.4AlF_3$:$0.76Ce_2O_3$	2500	N/A	90, 400	[120]
$51.15SiO_2$:$33Li_2O$: $9.9Al_2O_3$:5.45MgO:$0.5Ce_2O_3$[a]	3500	14	50-100	[30]
$15SiO_2$:$30B_2O_3$:$25Al_2O_3$:$30Gd_2O_3$:($1Ce_2O_3$wt%)	907	18.7	N/A	[121]
$45P_2O_5$:$35Li_2O$:$9GdI_3$:$5Al_2O_3$:$5CaCO_3$:$1CeBr_3$	1600	31	40, 2290	This study

[a] wt. % converted to mol%

Bibliography

117) J.T.M. de Haas, P. Dorenbos, C.W.E. van Eijk, Measuring the absolute light yield of scintillators, Nucl. Instruments Methods Phys. Res. Sect. A Accel. Spectrometers, Detect. Assoc. Equip. 537 (2005) 97-100. https://doi.org/10.1016/j.nima.2004.07.243.

118) Z.T. Kang, R. Rosson, B. Barta, C. Han, J.H. Nadler, M. Dorn, B. Wagner, B. Kahn, GdBr3:Ce in glass matrix as nuclear spectroscopy detector, Radiat. Meas. 48 (2013) 7-11. https://doi.org/10.1016/j.radmeas.2012.11.010.

119) C. Struebing, M.B. Beckert, J.H. Nadler, B. Kahn, B. Wagner, Z. Kang, Optimization of a gadolinium-rich oxyhalide glass scintillator for gamma ray spectroscopy, J. Am. Ceram. Soc. 101 (2018) 1116-1121. https://doi.org/10.1111/jace.15273.

120) Dormenev, A. Amelina, E. Auffray, K.-T. Brinkmann, G. Dosovitskiy, F. Cova, A. Fedorov, S. Gundacker, D. Kazlou, M. Korjik, N. Kratochwil, V. Ladygin, V. Mechinsky, M. Moritz, S. Nargelas, R.W. Novotny, P. Orsich, M. Salomoni, Y. Talochka, G. Tamulaitis, A. Vaitkevicius, A. Vedda, H.-G. Zaunick, Multipurpose Ce-doped Ba-Gd silica glass scintillator for radiation measurements, Nucl. Instr. Meth. Phys. Res. Sect. A Accel. Spectrometers, Detect. Assoc. Equip. 1015 (2021) 165762. https://doi.org/10.1016/j.nima.2021.165762.

121) W. Chewpraditkul, X. He, D. Chen, Y. Shen, Q. Sheng, B. Yu, M. Nikl, R. Kucerkova, A. Beitlerova, C. Wanarak, A. Phunpueok, Luminescence and scintillation of Ce^{3+}-doped oxide glass with high Gd_2O_3 concentration, Phys. Status Solidi Appl. Mater. Sci. 208 (2011) 2830-2832. https://doi.org/10.1002/pssa.201127365.

The full article is available as,

Sudipta Saha, A. V. Ntarisa, Nguyen Duy Quang, N. T. Luan, P. Q. Vuong, H. J. Kim, N. Intachai, S. Kothan, J. Kaewkhao, *Scintillation Performance of the Ce^{3+} -Activated Lithium Phosphate Glass*, Radiation Physics and Chemistry. 199 (2022) 110285.
https://doi.org/10.1016/j.radphyschem.2022.110285